US011594753B2

(12) **United States Patent**
Kumta et al.

(10) **Patent No.: US 11,594,753 B2**
(45) **Date of Patent: Feb. 28, 2023**

(54) **CATHODES AND ELECTROLYTES FOR RECHARGEABLE MAGNESIUM BATTERIES AND METHODS OF MANUFACTURE**

(71) Applicant: **UNIVERSITY OF PITTSBURGH—OF THE COMMONWEALTH SYSTEM OF HIGHER EDUCATION**, Pittsburgh, PA (US)

(72) Inventors: **Prashant N. Kumta**, Pittsburgh, PA (US); **Partha Saha**, Pittsburgh, PA (US); **Moni Kanchan Datta**, Pittsburgh, PA (US); **Ayyakkannu Manivannan**, Morgantown, WV (US)

(73) Assignees: **UNIVERSITY OF PITTSBURGH—OF THE COMMONWEALTH SYSTEM OF HIGHER EDUCATION**, Pittsburgh, PA (US); **COMMONWEALTH SYSTEM OF HIGHER EDUCATION**, Pittsburgh, PA (US)

(*) Notice: Subject to any disclaimer, the term of this patent is extended or adjusted under 35 U.S.C. 154(b) by 209 days.

(21) Appl. No.: **17/085,099**

(22) Filed: **Oct. 30, 2020**

(65) **Prior Publication Data**

US 2021/0242488 A1 Aug. 5, 2021

Related U.S. Application Data

(60) Continuation-in-part of application No. 15/897,721, filed on Feb. 15, 2018, now Pat. No. 10,826,114,
(Continued)

(51) **Int. Cl.**
H01M 10/054 (2010.01)
H01M 4/58 (2010.01)
(Continued)

(52) **U.S. Cl.**
CPC ***H01M 10/054*** (2013.01); ***C01B 19/002*** (2013.01); ***C01B 19/007*** (2013.01);
(Continued)

(58) **Field of Classification Search**
None
See application file for complete search history.

(56) **References Cited**

U.S. PATENT DOCUMENTS

4,894,302 A 1/1990 Hoffman et al.
4,966,749 A 10/1990 Kondo et al.
(Continued)

OTHER PUBLICATIONS

Nanjundaswamy et al., Convenient synthesis of the chevrel phases MxMo6S8 (M=Cu,Pb,La,or Gd), 1987, InorgChem, 26 ,4286-4288 (Year: 1987).*
(Continued)

Primary Examiner — Daniel S Gatewood
(74) *Attorney, Agent, or Firm* — Carol A. Marmo; Eckert Seamans Cherin & Mellott, LLC

(57) **ABSTRACT**

The invention relates to Chevrel-phase materials and methods of preparing these materials utilizing a precursor approach. The Chevrel-phase materials are useful in assembling electrodes, e.g., cathodes, for use in electrochemical cells, such as rechargeable batteries. The Chevrel-phase materials have a general formula of Mo_6Z_8 (Z=sulfur) or $Mo_6Z^1{}_{8-y}Z^2{}_y$ (Z^1=sulfur; Z^2=selenium), and partially cuprated $Cu_1Mo_6S_8$ as well as partially de-cuprated $Cu_{1-x}Mg_xMo_6S_8$ and the precursors have a general formula of $M_xMo_6Z_8$ or $M_xMo_6Z^1{}_{8-y}Z^2{}_y$, M=Cu. The cathode containing the Chevrel-phase material in accordance with the invention can be combined with a magnesium-containing anode and an electrolyte.

9 Claims, 23 Drawing Sheets

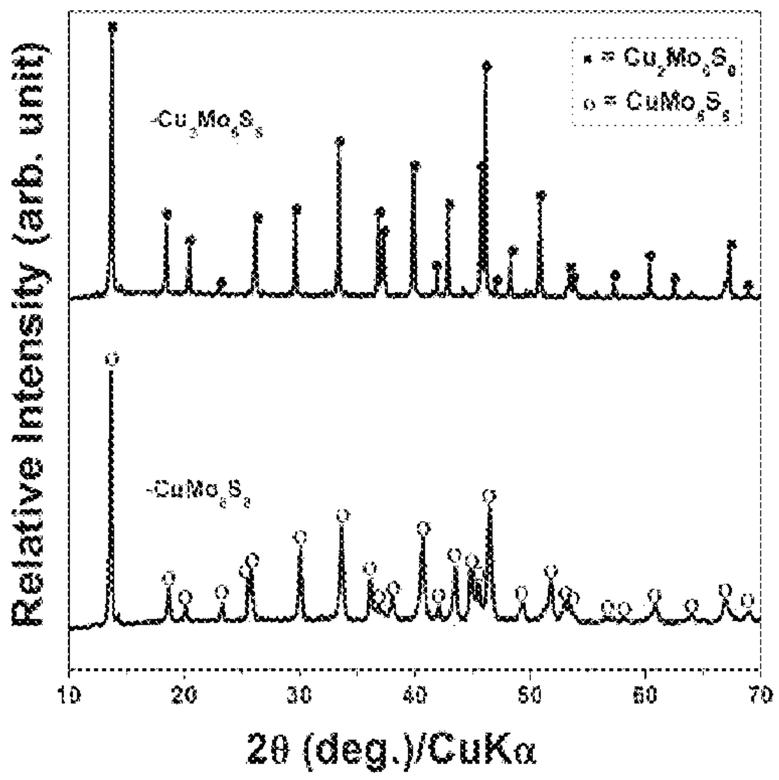

Related U.S. Application Data

which is a division of application No. 14/325,891, filed on Jul. 8, 2014, now Pat. No. 9,947,962.

(60) Provisional application No. 61/843,647, filed on Jul. 8, 2013.

(51) **Int. Cl.**

C01G 39/06	(2006.01)
C01G 39/00	(2006.01)
H01M 10/052	(2010.01)
C01B 19/00	(2006.01)
H01M 4/02	(2006.01)

(52) **U.S. Cl.**

CPC ***C01G 39/006*** (2013.01); ***C01G 39/06*** (2013.01); ***H01M 4/581*** (2013.01); ***H01M 4/5815*** (2013.01); ***H01M 10/052*** (2013.01); *C01P 2002/30* (2013.01); *C01P 2002/72* (2013.01); *C01P 2002/76* (2013.01); *C01P 2002/77* (2013.01); *C01P 2004/38* (2013.01); *C01P 2004/61* (2013.01); *C01P 2004/62* (2013.01); *C01P 2006/12* (2013.01); *C01P 2006/40* (2013.01); *H01M 2004/028* (2013.01)

(56) **References Cited**

U.S. PATENT DOCUMENTS

6,316,141	B1	11/2001	Aurbach et al.	
8,318,354	B2	11/2012	Muldoon et al.	
2001/0049060	A1	12/2001	Aurbach et al.	
2005/0220699	A1*	10/2005	Gofer	C01G 39/00 423/561.1
2008/0182176	A1*	7/2008	Aurbach	C01B 19/002 423/508
2011/0159381	A1*	6/2011	Doe	H01M 4/13 429/219
2011/0244338	A1	10/2011	Muldoon et al.	

OTHER PUBLICATIONS

Nanjundaswamy et al., Convenient Synthesis of the Chevrel Phases MxMo6S8 (M=Cu, Pb, La or Gd), Inorganic Chemistry (1987), 26:4286-4288.

* cited by examiner

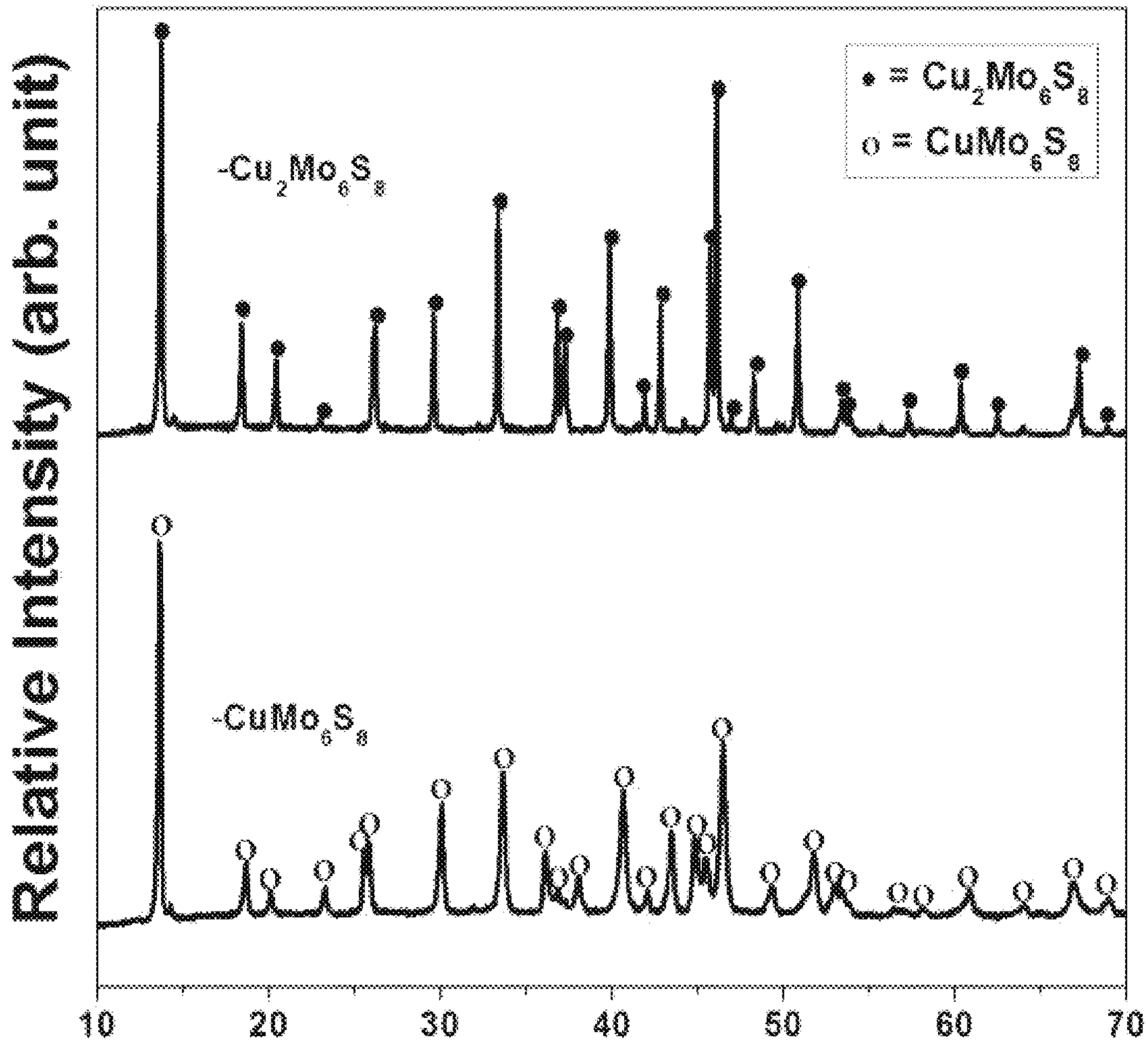
• = Cu2Mo6S8
o = CuMo6S8
-Cu2Mo6S8
-CuMo6S8
Relative Intensity (arb. unit)
10
20
30
40
50
60
70
2θ (deg.)/CuKα

FIG 1

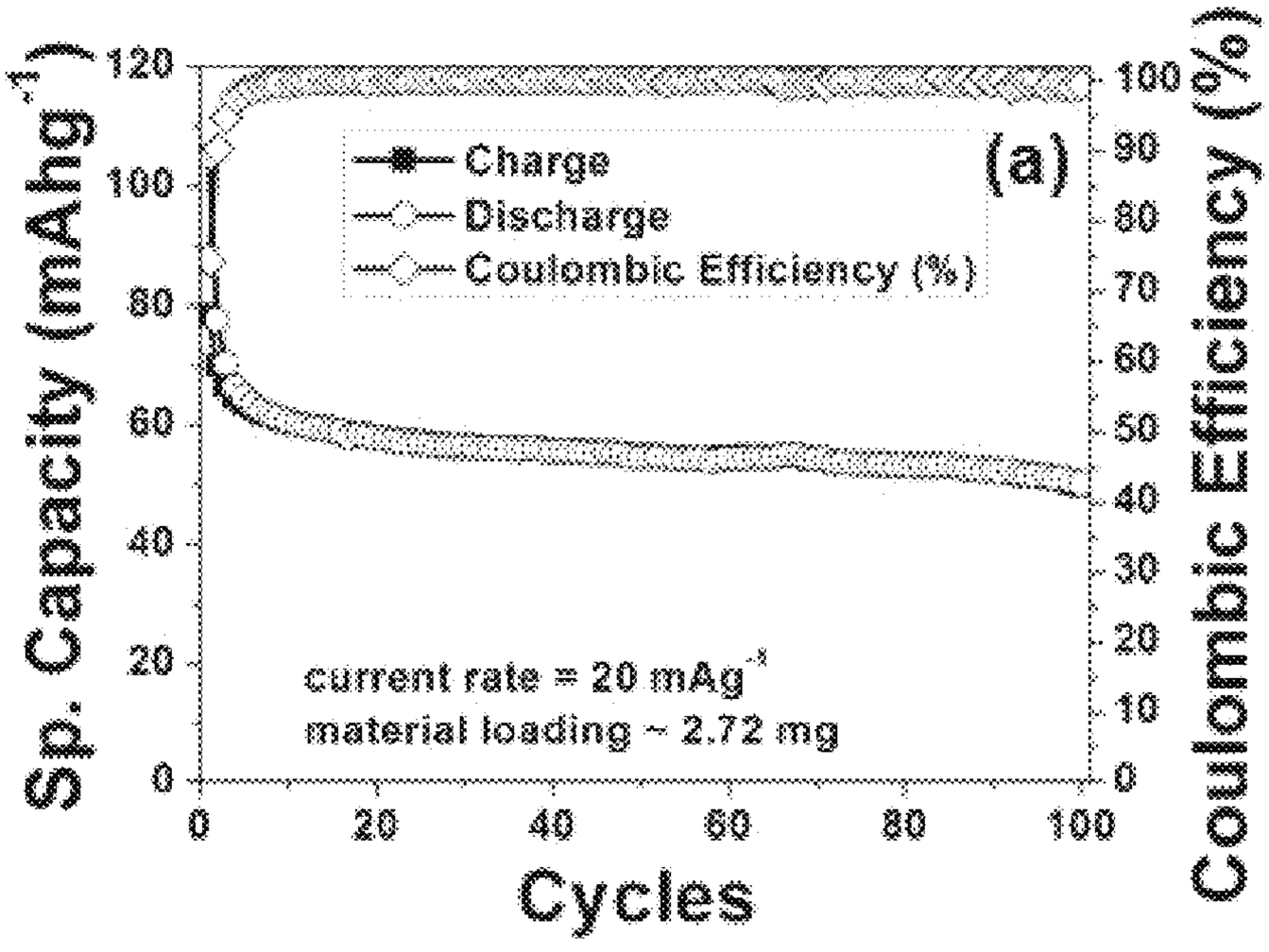
Sp. Capacity (mAhg-1)
Coulombic Efficiency (%)
Cycles
Charge
Discharge
Coulombic Efficiency (%)
(a)
current rate = 20 mAg-1
material loading ~ 2.72 mg
0
20
40
60
80
100
120
0
10
20
30
40
50
60
70
80
90
100

FIG 2a

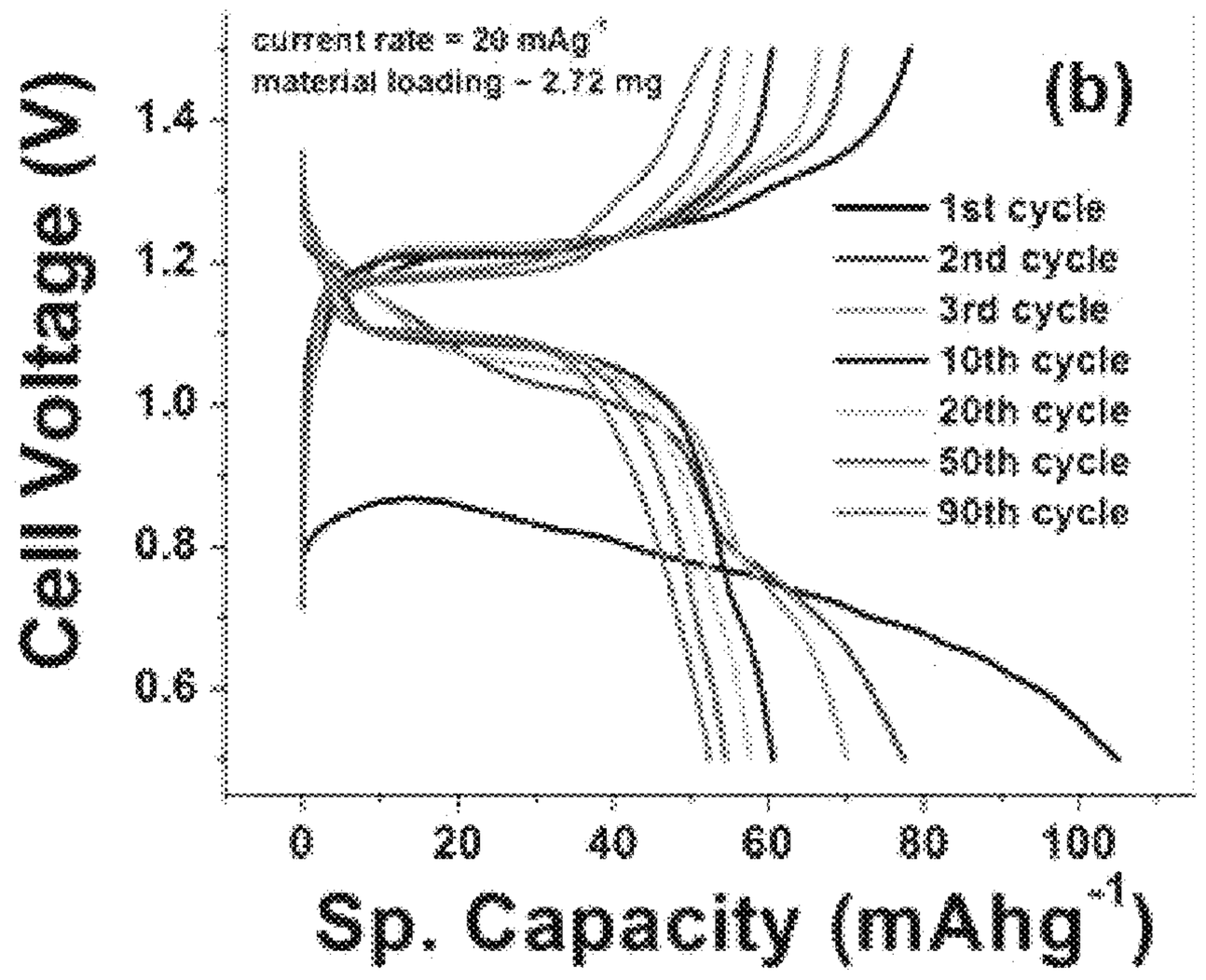
current rate = 20 mAg-1
material loading ~ 2.72 mg
(b)
1st cycle
2nd cycle
3rd cycle
10th cycle
20th cycle
50th cycle
90th cycle
Cell Voltage (V)
1.4
1.2
1.0
0.8
0.6
0
20
40
60
80
100
Sp. Capacity (mAhg-1)

FIG 2b

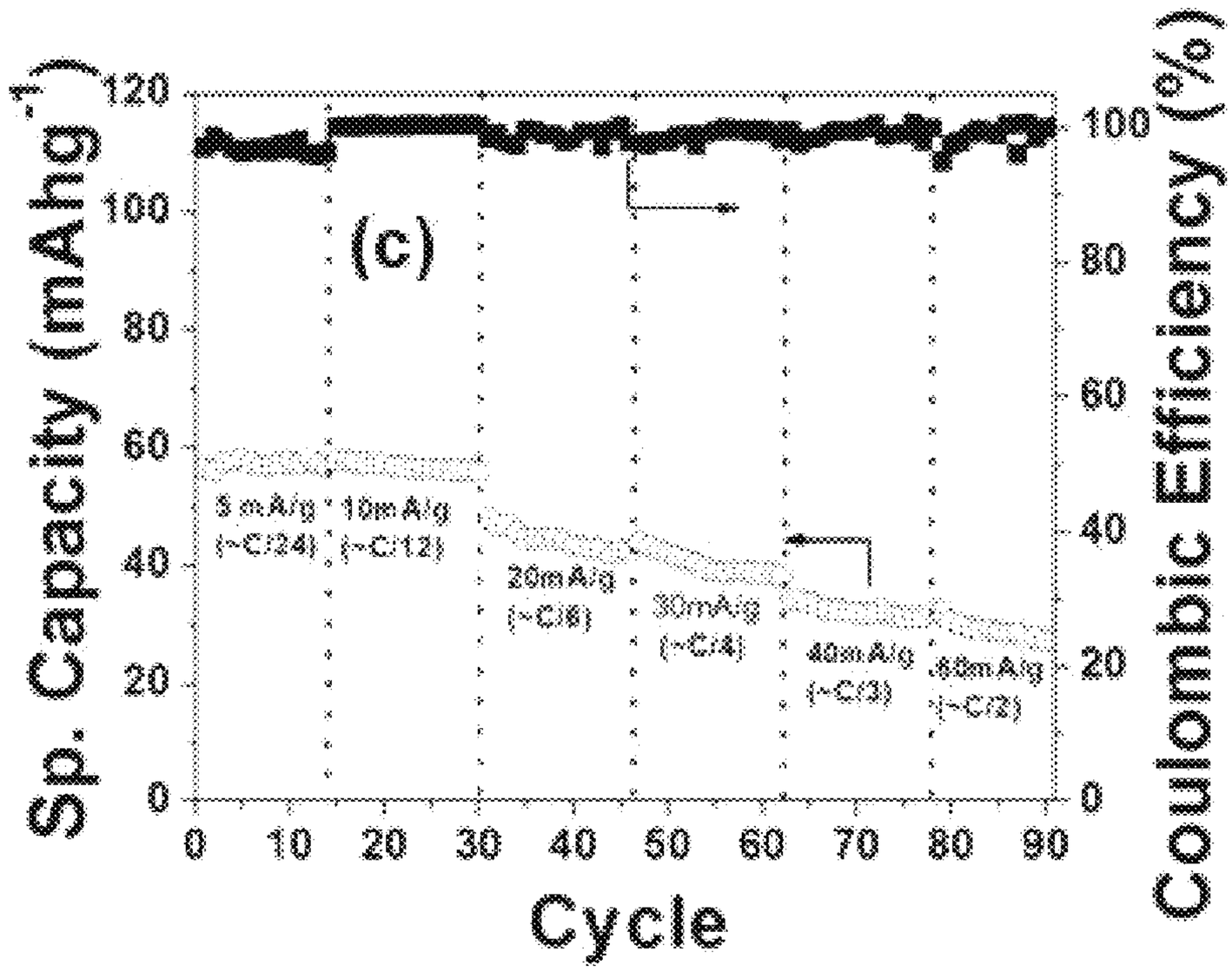
(c)
Sp. Capacity (mAhg-1)
Coulombic Efficiency (%)
Cycle
5 mA/g (~C/24)
10mA/g (~C/12)
20mA/g (~C/8)
30mA/g (~C/4)
40mA/g (~C/3)
60mA/g (~C/2)
0
20
40
60
80
100
120
0
10
20
30
40
50
60
70
80
90

FIG 2c

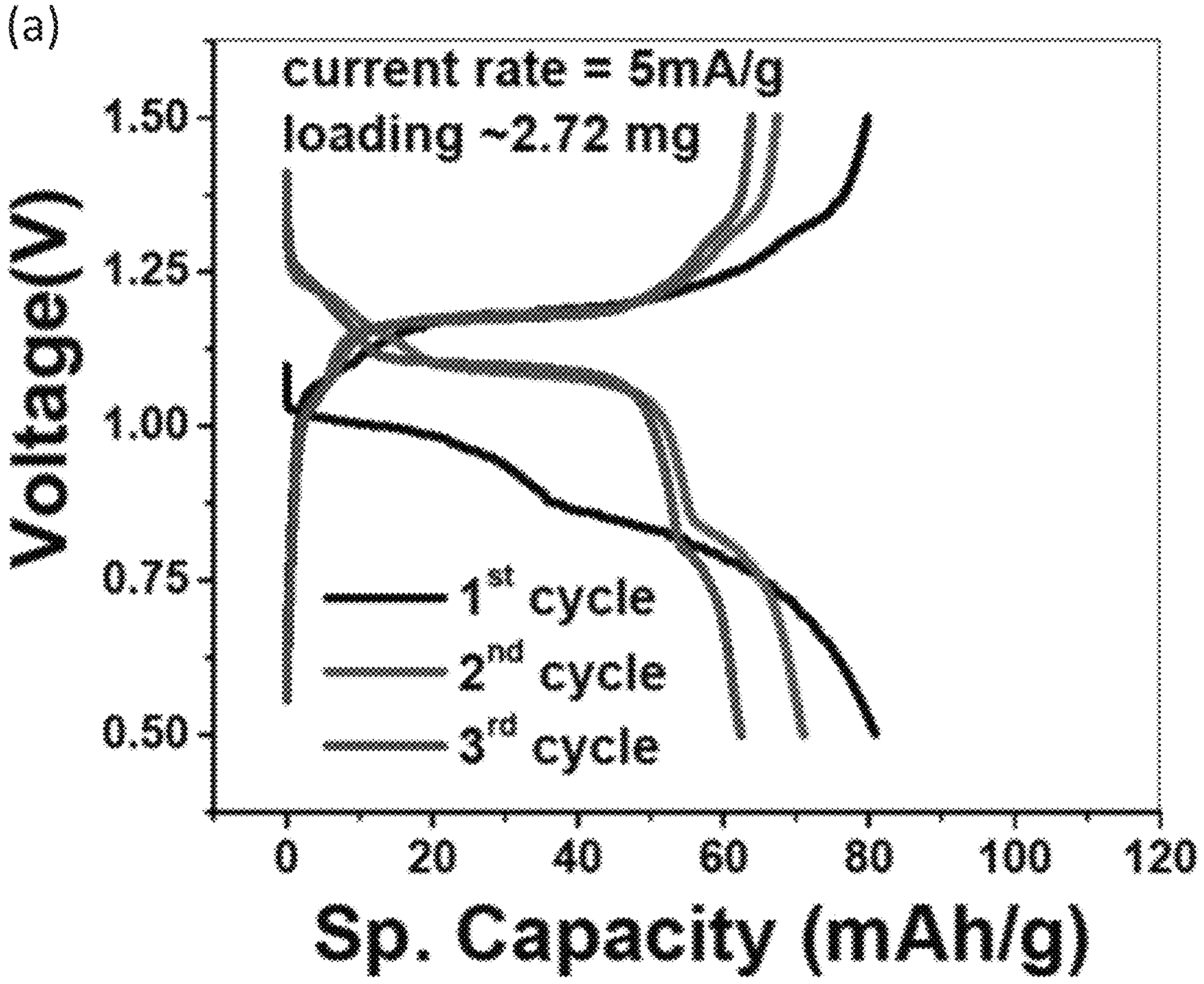
(a)
current rate = 5mA/g
loading ~2.72 mg
Voltage(V)
1.50
1.25
1.00
0.75
0.50
1st cycle
2nd cycle
3rd cycle
0
20
40
60
80
100
120
Sp. Capacity (mAh/g)

FIG 3a

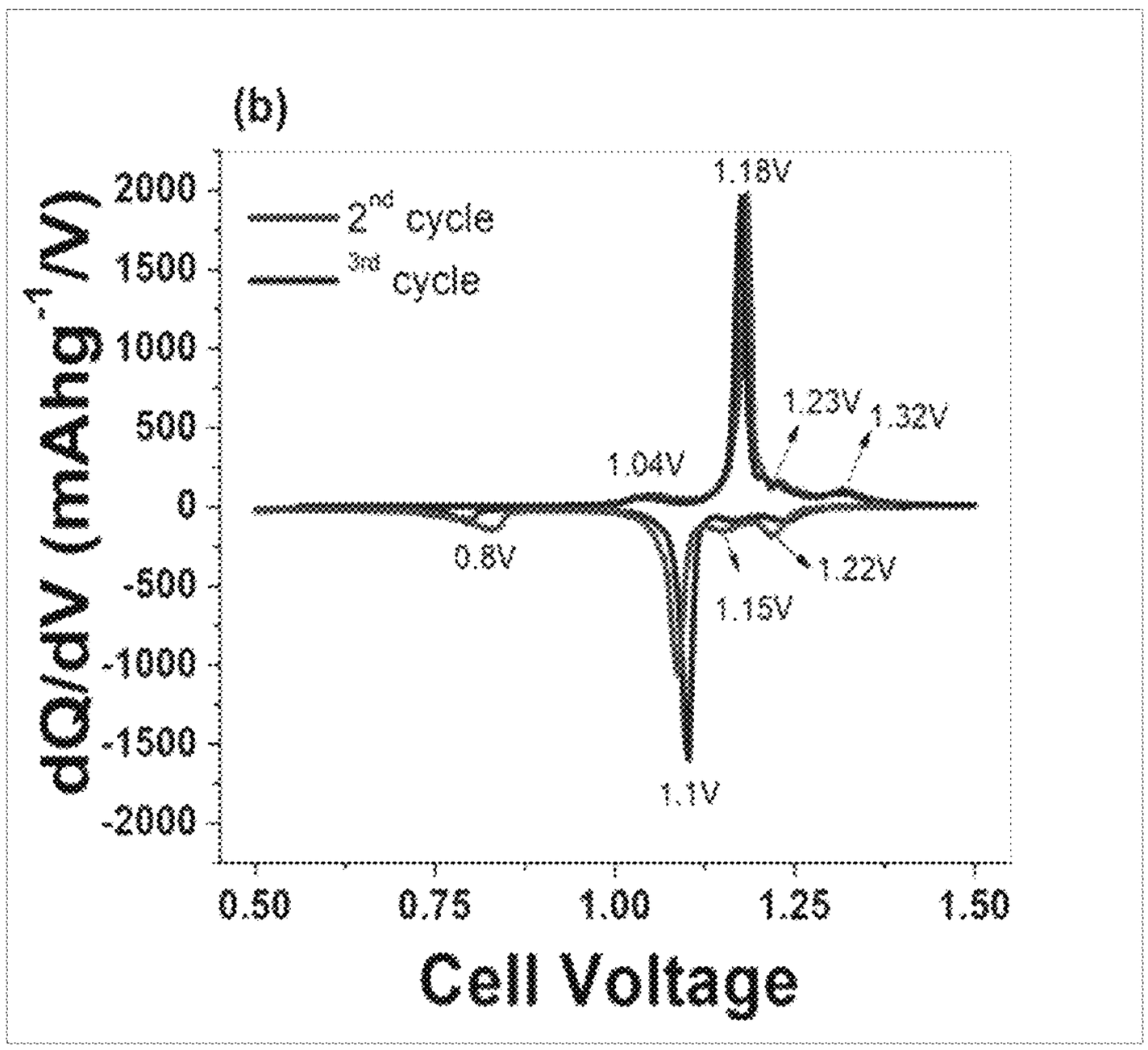
(b)
dQ/dV (mAhg-1/V)
2000
1500
1000
500
0
-500
-1000
-1500
-2000
2nd cycle
3rd cycle
1.18V
1.23V
1.32V
1.04V
0.8V
1.22V
1.15V
1.1V
0.50
0.75
1.00
1.25
1.50
Cell Voltage

FIG 3b

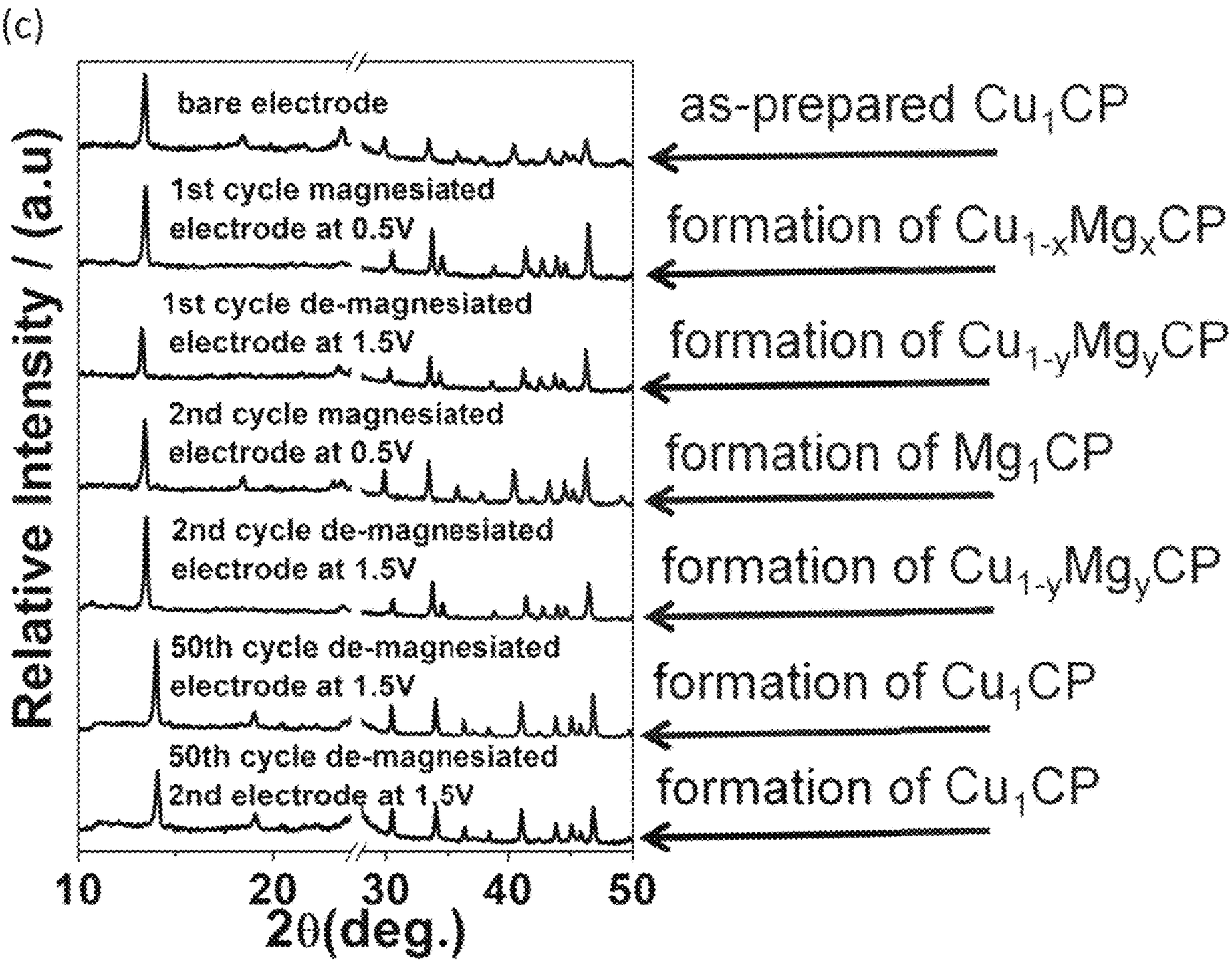
(c)
bare electrode
as-prepared Cu1CP
1st cycle magnesiated electrode at 0.5V
formation of Cu1-xMgxCP
1st cycle de-magnesiated electrode at 1.5V
formation of Cu1-yMgyCP
2nd cycle magnesiated electrode at 0.5V
formation of Mg1CP
2nd cycle de-magnesiated electrode at 1.5V
formation of Cu1-yMgyCP
50th cycle de-magnesiated electrode at 1.5V
formation of Cu1CP
50th cycle de-magnesiated 2nd electrode at 1.5V
formation of Cu1CP
Relative intensity / (a.u.)
10
20
30
40
50
2θ(deg.)

FIG 3c

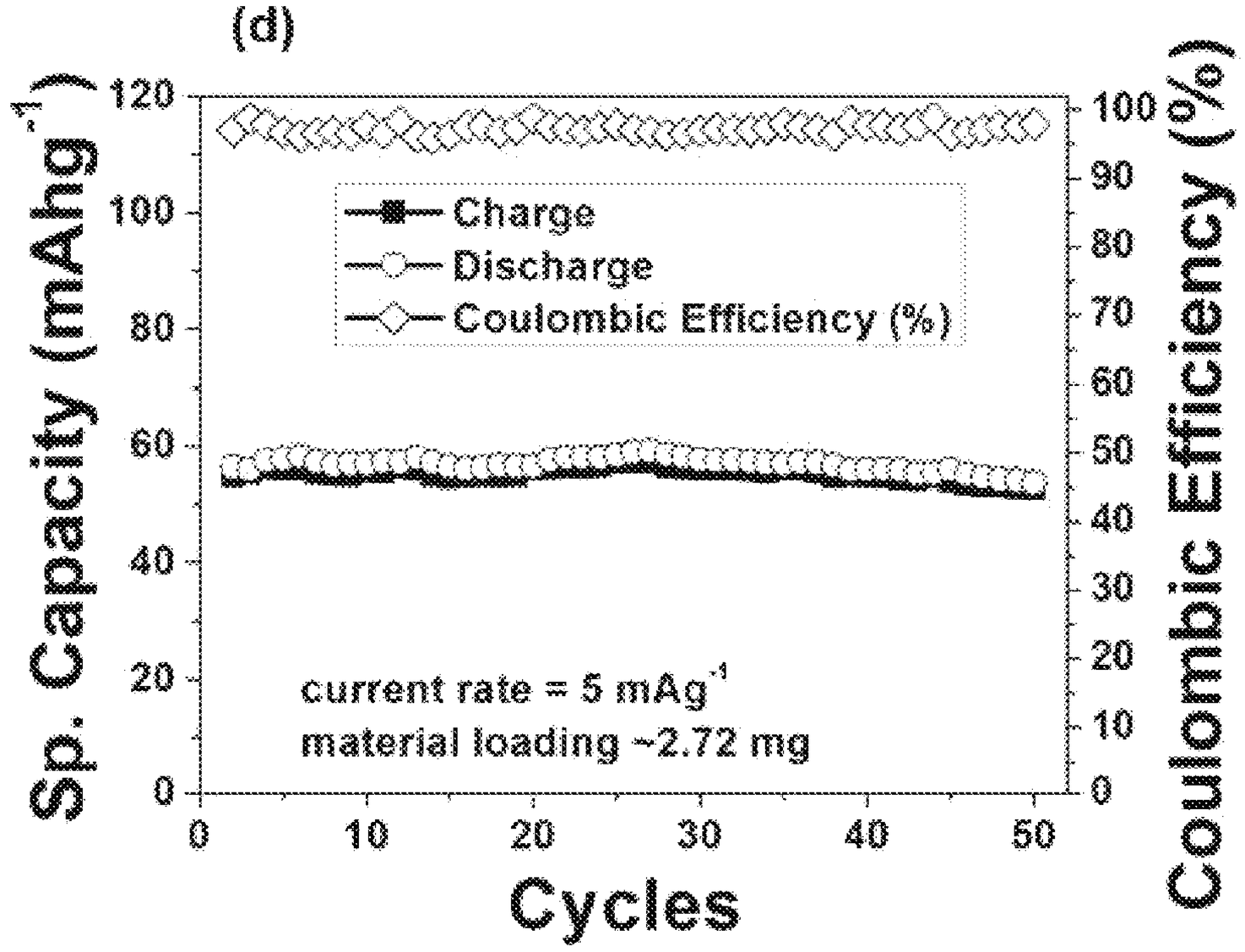
(d)
Sp. Capacity (mAhg-1)
Coulombic Efficiency (%)
Cycles
Charge
Discharge
Coulombic Efficiency (%)
current rate = 5 mAg-1
material loading ~2.72 mg
0
20
40
60
80
100
120
0
10
20
30
40
50
60
70
80
90
100

FIG 3d

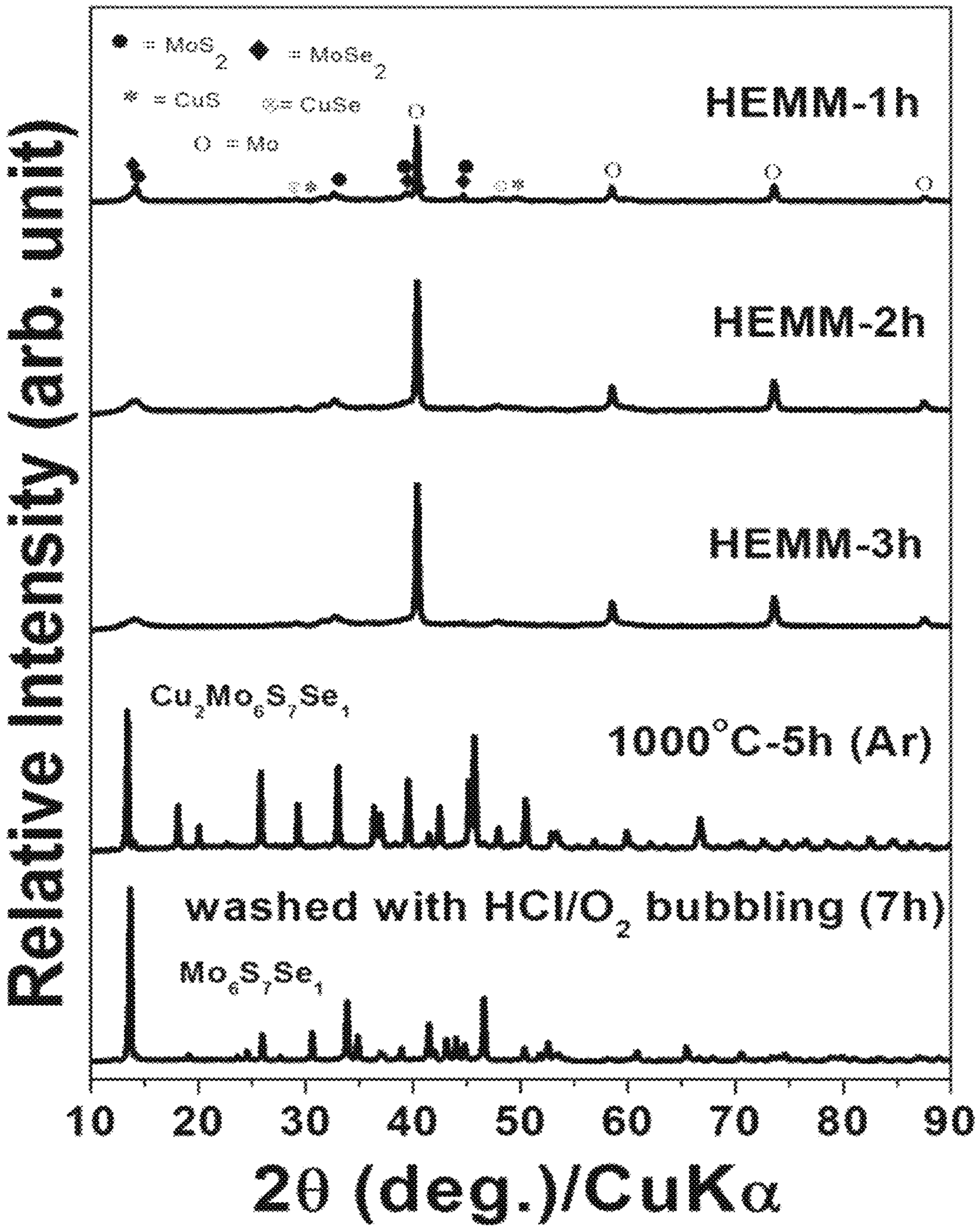
● = MoS_2
◆ = $MoSe_2$
※ = CuS
※ = CuSe
○ = Mo
HEMM-1h
HEMM-2h
HEMM-3h
$Cu_2Mo_6S_7Se_1$
1000°C-5h (Ar)
washed with HCl/O_2 bubbling (7h)
$Mo_6S_7Se_1$
Relative Intensity (arb. unit)
10
20
30
40
50
60
70
80
90
2θ (deg.)/CuKα

FIG 4

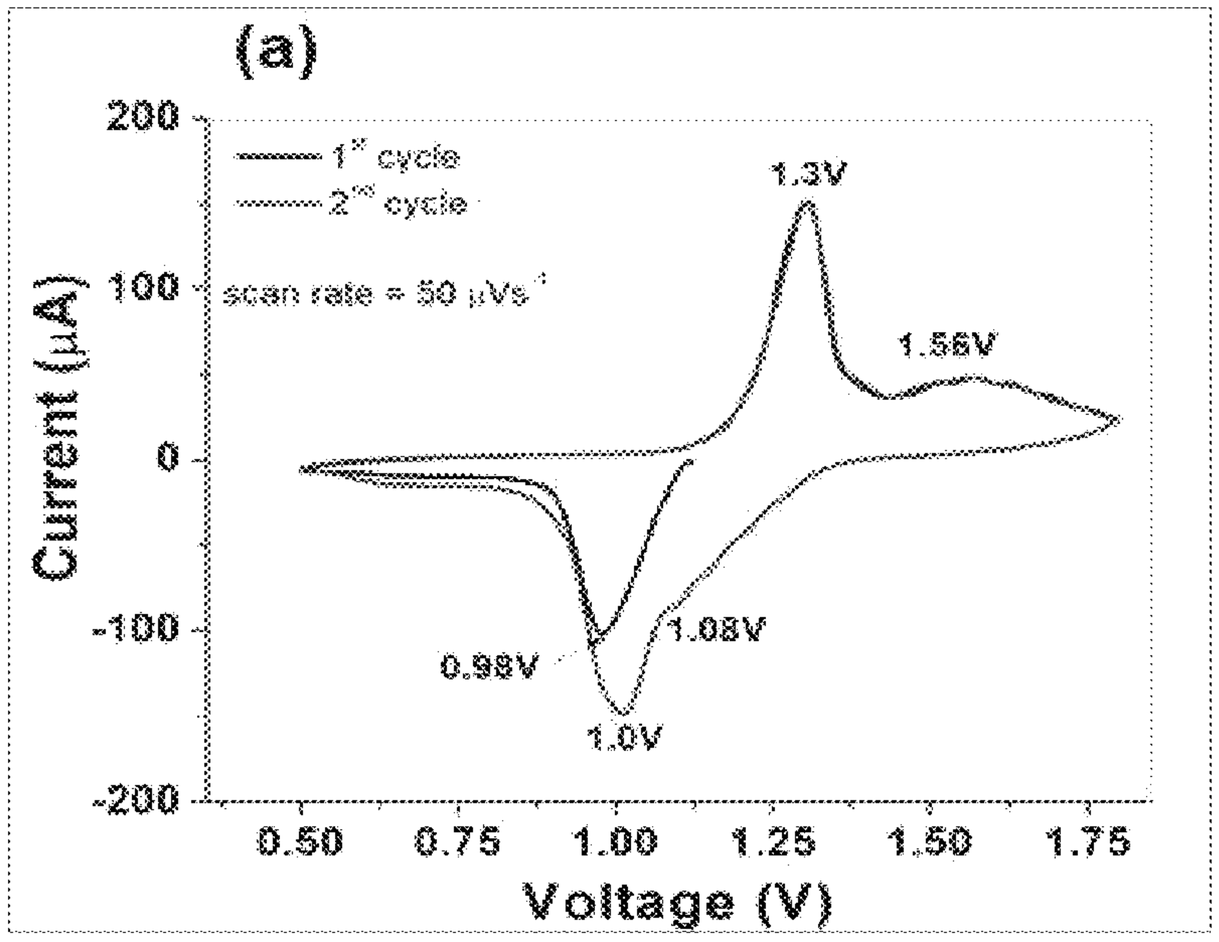
(a)
200
100
0
-100
-200
Current (μA)
1st cycle
2nd cycle
scan rate = 50 μVs-1
1.3V
1.56V
1.08V
0.98V
1.0V
0.50
0.75
1.00
1.25
1.50
1.75
Voltage (V)

FIG 5a

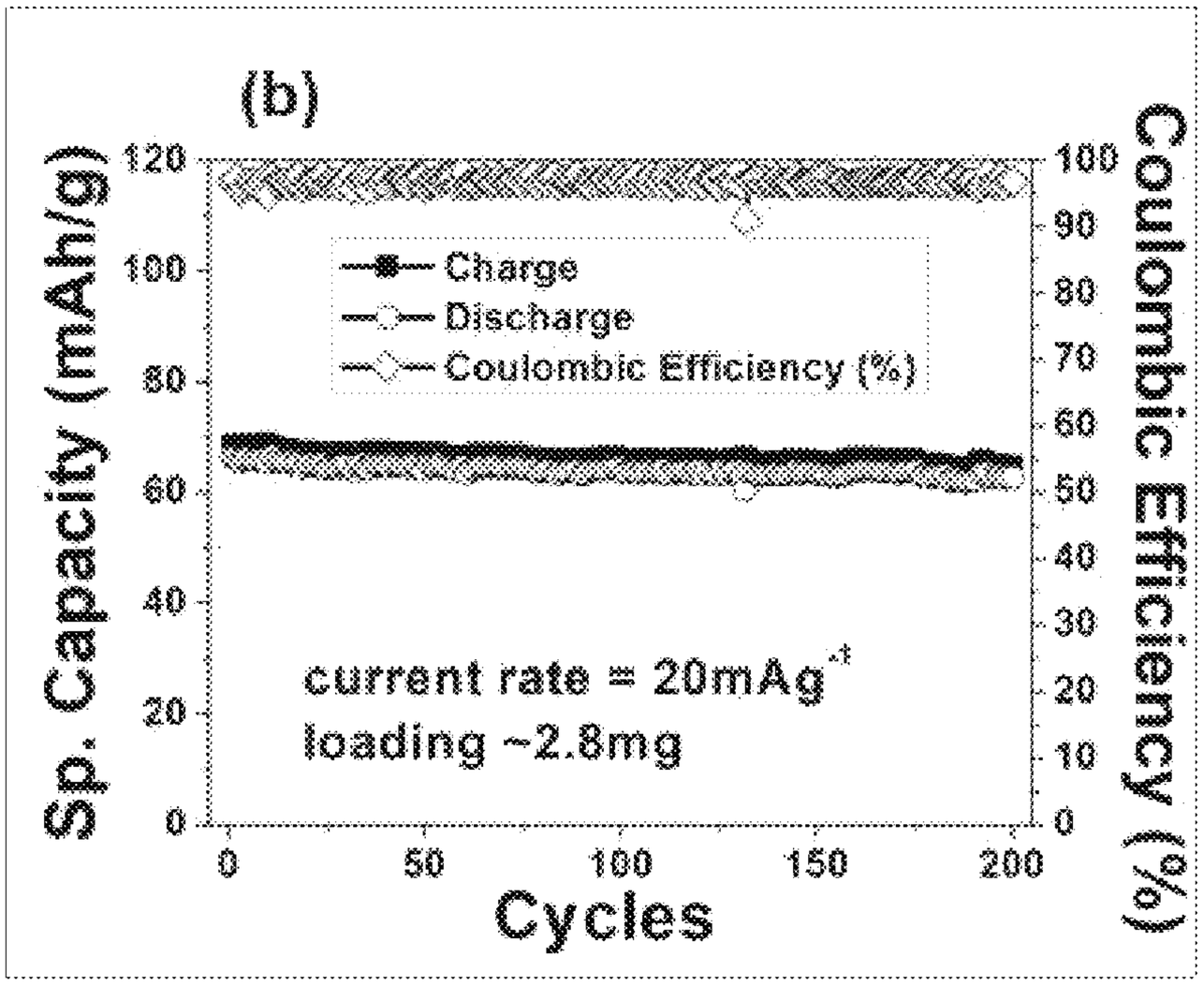
(b)
Sp. Capacity (mAh/g)
Coulombic Efficiency (%)
Charge
Discharge
Coulombic Efficiency (%)
current rate = 20mAg-1
loading ~2.8mg
Cycles
0
20
40
60
80
100
120
0
10
20
30
40
50
60
70
80
90
100
0
50
100
150
200

FIG 5b

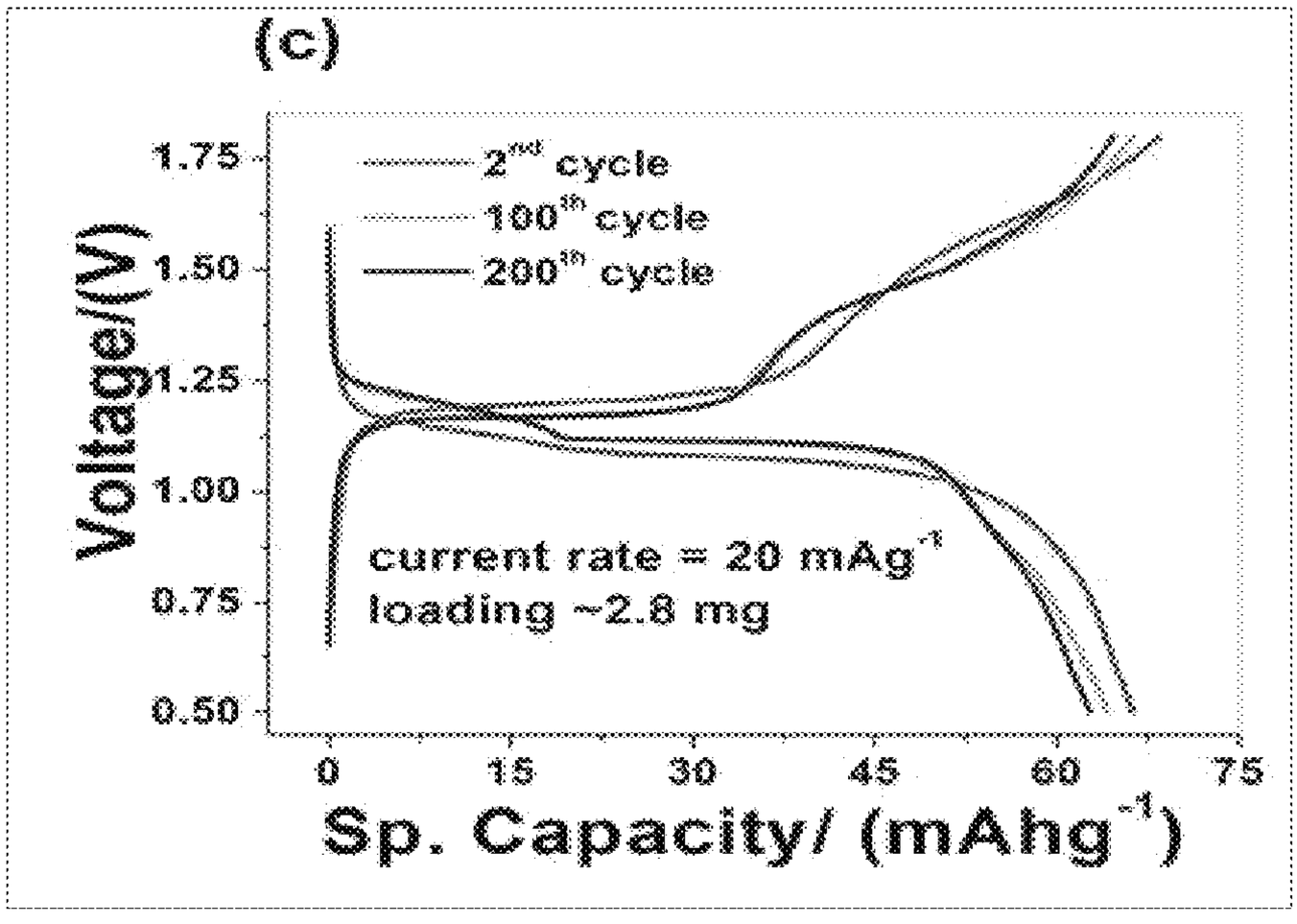
(c)
1.75
1.50
1.25
1.00
0.75
0.50
Voltage/(V)
2nd cycle
100th cycle
200th cycle
current rate = 20 mAg-1
loading ~2.8 mg
0
15
30
45
60
75
Sp. Capacity/ (mAhg-1)

FIG 5c

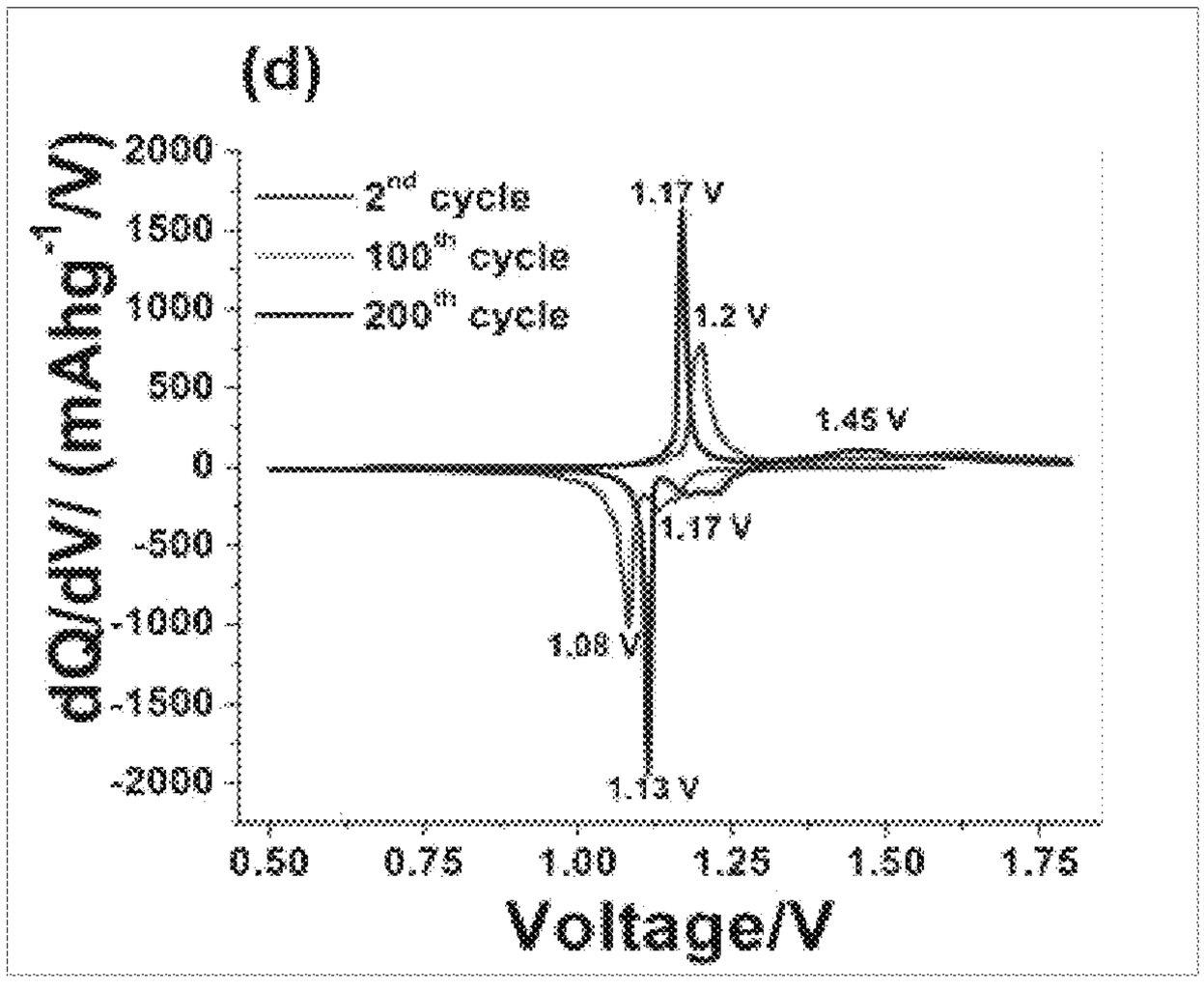
(d)
dQ/dV/ (mAhg-1/V)
2000
1500
1000
500
0
-500
-1000
-1500
-2000
2nd cycle
100th cycle
200th cycle
1.17 V
1.2 V
1.45 V
1.17 V
1.08 V
1.13 V
0.50
0.75
1.00
1.25
1.50
1.75
Voltage/V

FIG 5d

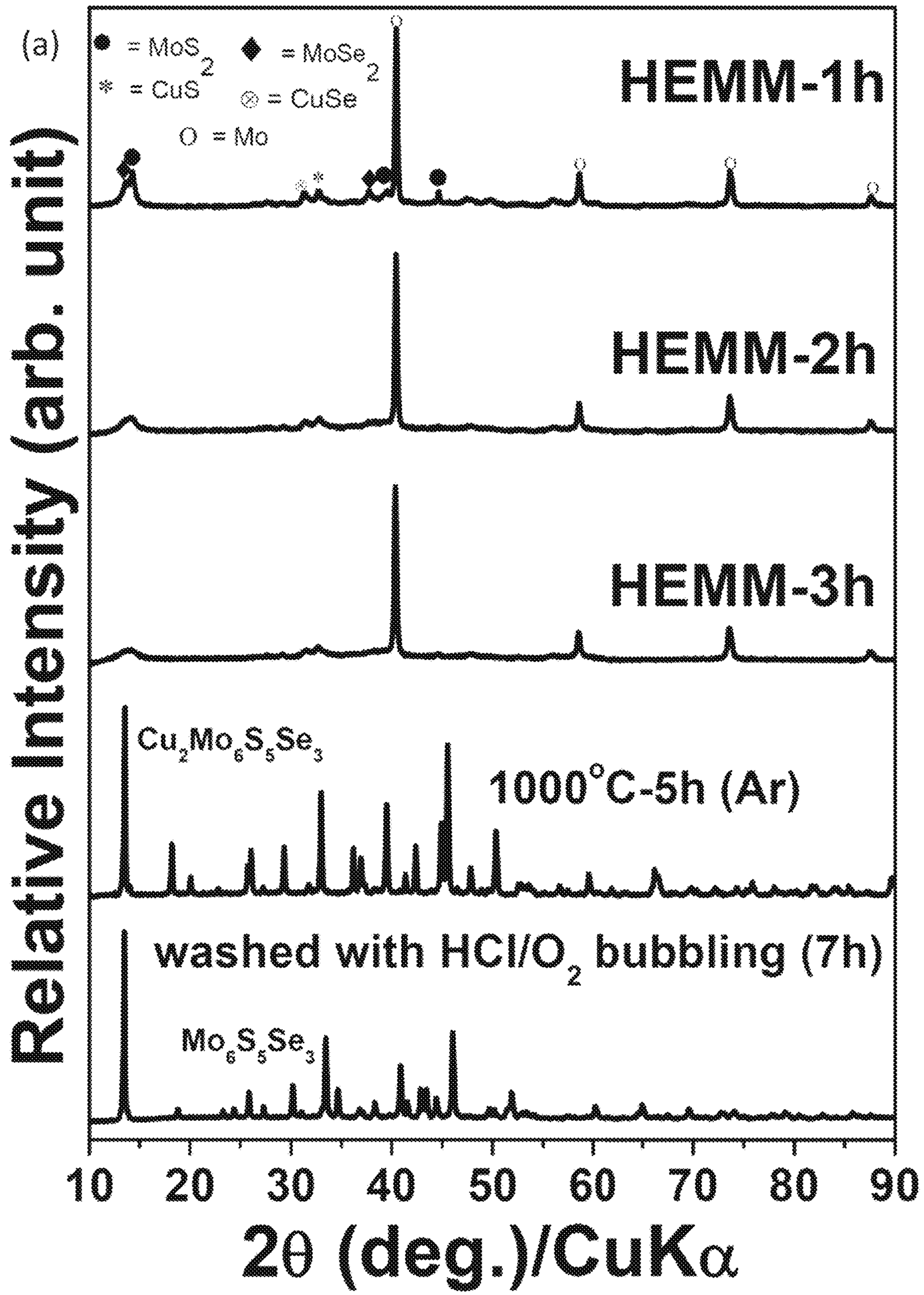
(a)
● = MoS2
◆ = MoSe2
* = CuS2
⊗ = CuSe
○ = Mo
HEMM-1h
HEMM-2h
HEMM-3h
Cu2Mo6S5Se3
1000°C-5h (Ar)
washed with HCl/O2 bubbling (7h)
Mo6S5Se3
Relative Intensity (arb. unit)
10
20
30
40
50
60
70
80
90
2θ (deg.)/CuKα

FIG 6a

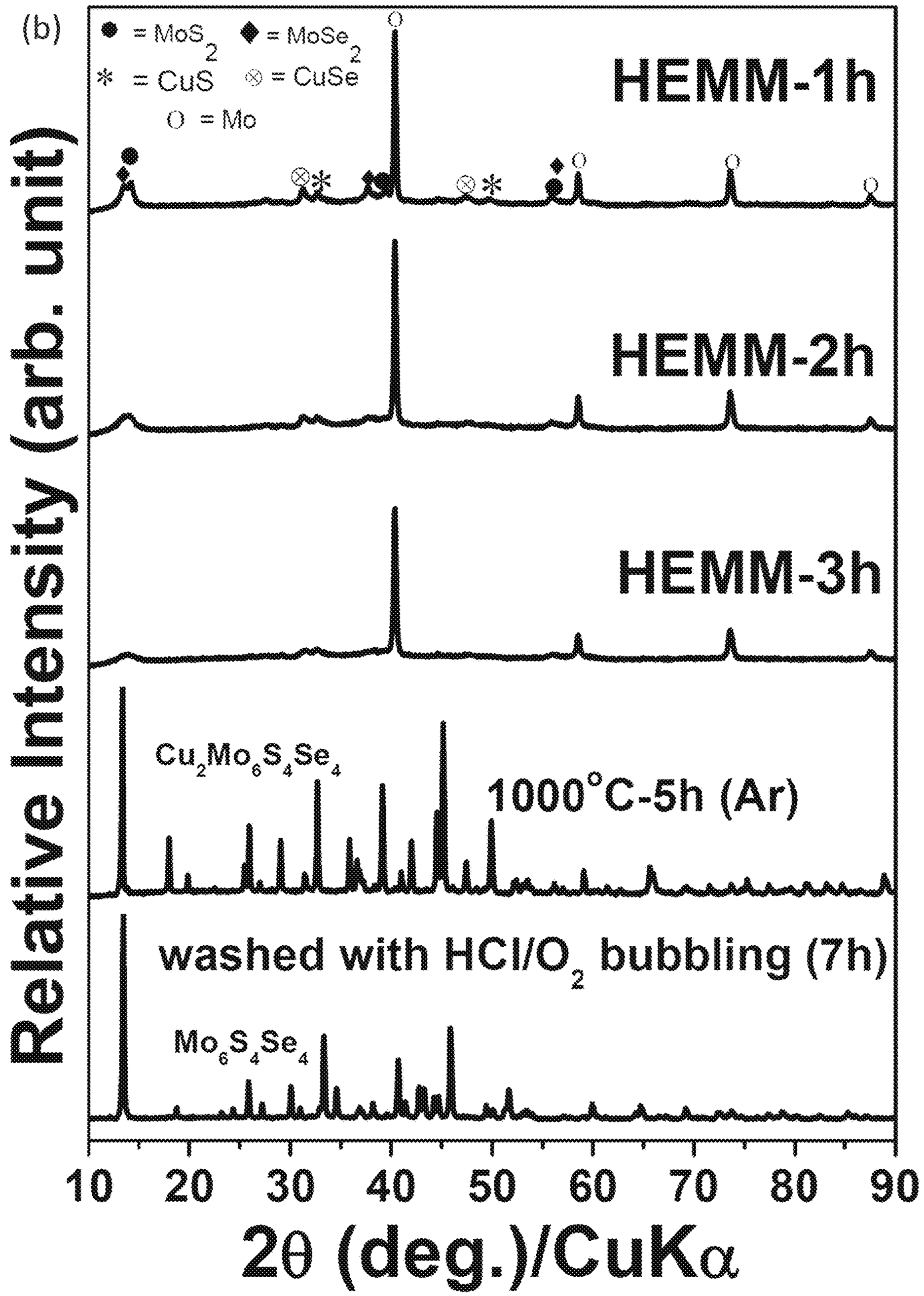
(b)
● = MoS_2 ◆ = $MoSe_2$
* = CuS ⊗ = $CuSe_2$
○ = Mo
HEMM-1h
HEMM-2h
HEMM-3h
$Cu_2Mo_6S_4Se_4$
1000°C-5h (Ar)
washed with HCl/O_2 bubbling (7h)
$Mo_6S_4Se_4$
Relative Intensity (arb. unit)
10 20 30 40 50 60 70 80 90
2θ (deg.)/CuKα

FIG 6b

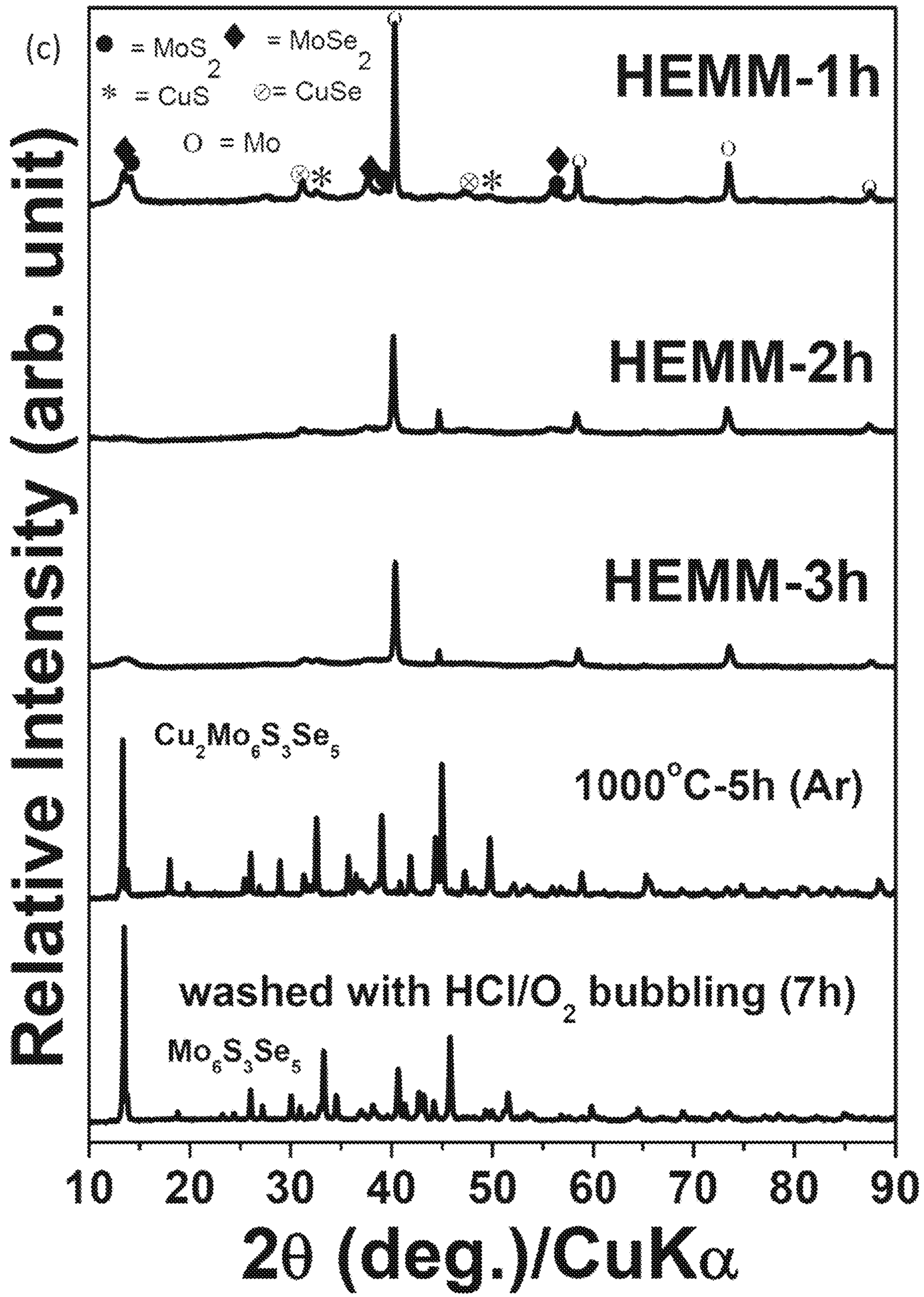
(c)
● = MoS_2 ◆ = $MoSe_2$
* = CuS ⊘ = CuSe
O = Mo
HEMM-1h
HEMM-2h
HEMM-3h
$Cu_2Mo_6S_3Se_5$
1000°C-5h (Ar)
washed with HCl/O_2 bubbling (7h)
$Mo_6S_3Se_5$
Relative Intensity (arb. unit)
10 20 30 40 50 60 70 80 90
2θ (deg.)/CuKα

FIG 6c

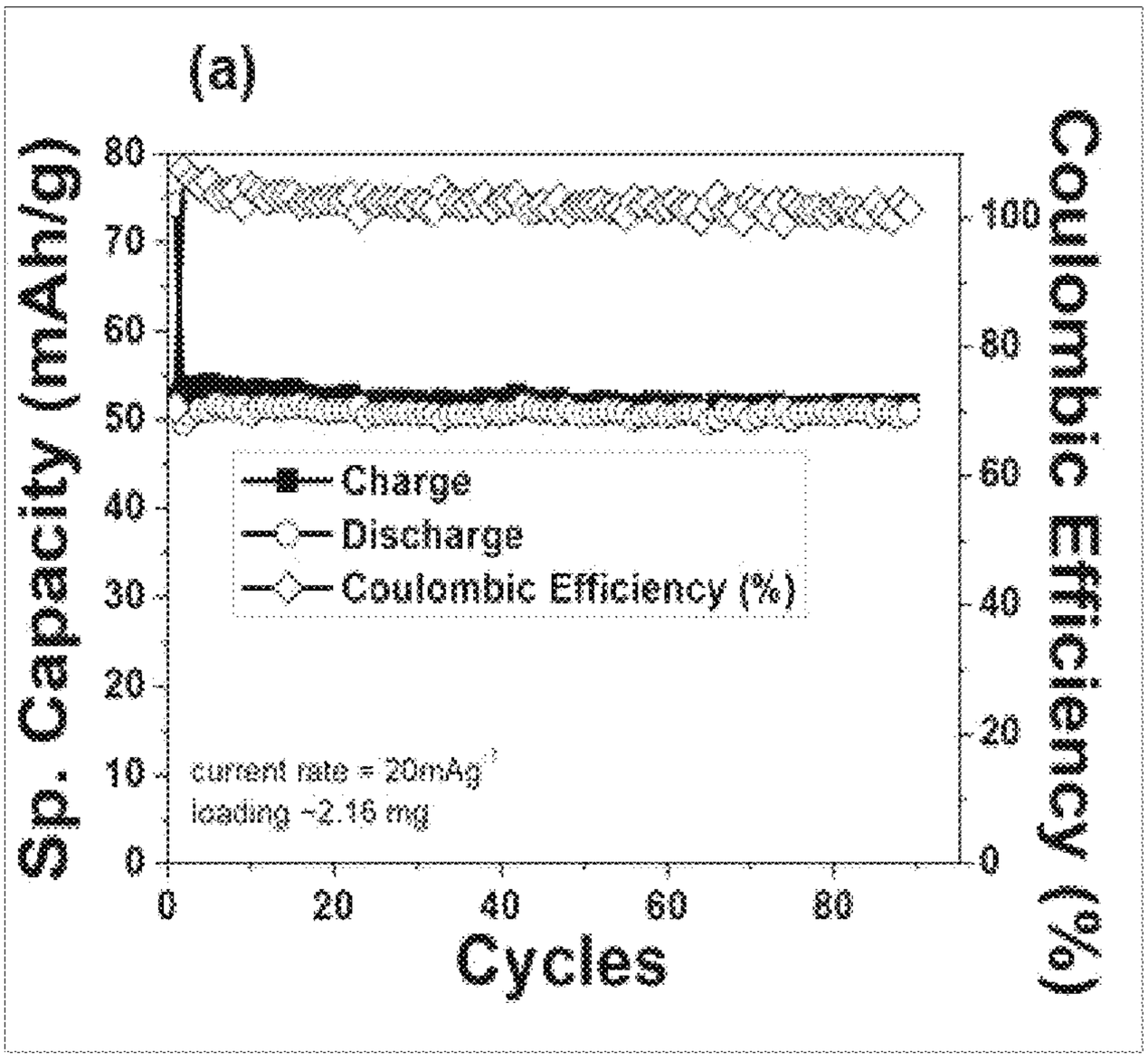
(a)
Sp. Capacity (mAh/g)
Coulombic Efficiency (%)
Cycles
Charge
Discharge
Coulombic Efficiency (%)
current rate = 20mAg-1
loading ~2.16 mg
0
10
20
30
40
50
60
70
80
0
20
40
60
80
100

FIG 7a

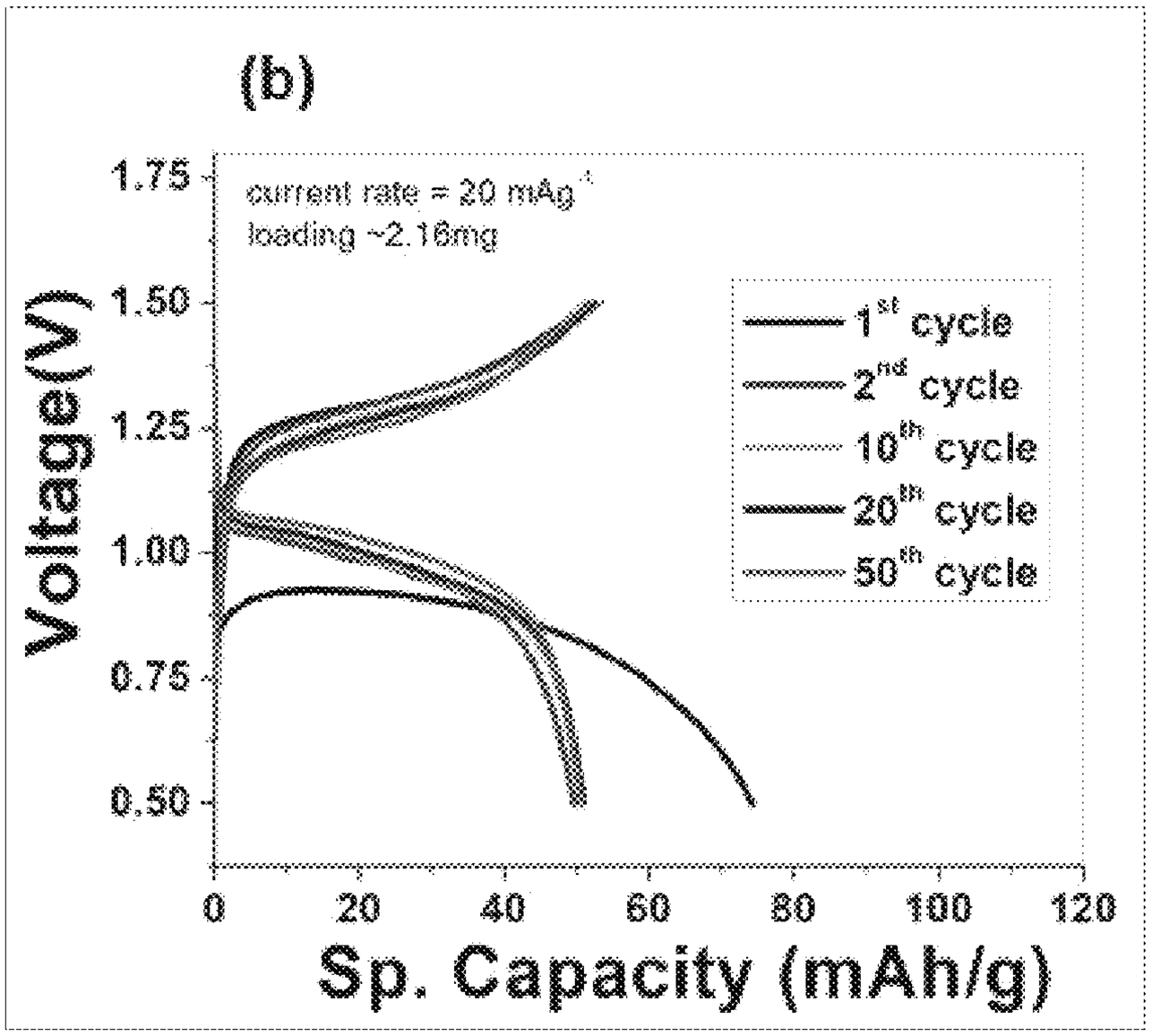
(b)
current rate = 20 mAg-1
loading ~2.16mg
1st cycle
2nd cycle
10th cycle
20th cycle
50th cycle
Voltage(V)
1.75
1.50
1.25
1.00
0.75
0.50
0
20
40
60
80
100
120
Sp. Capacity (mAh/g)

FIG 7b

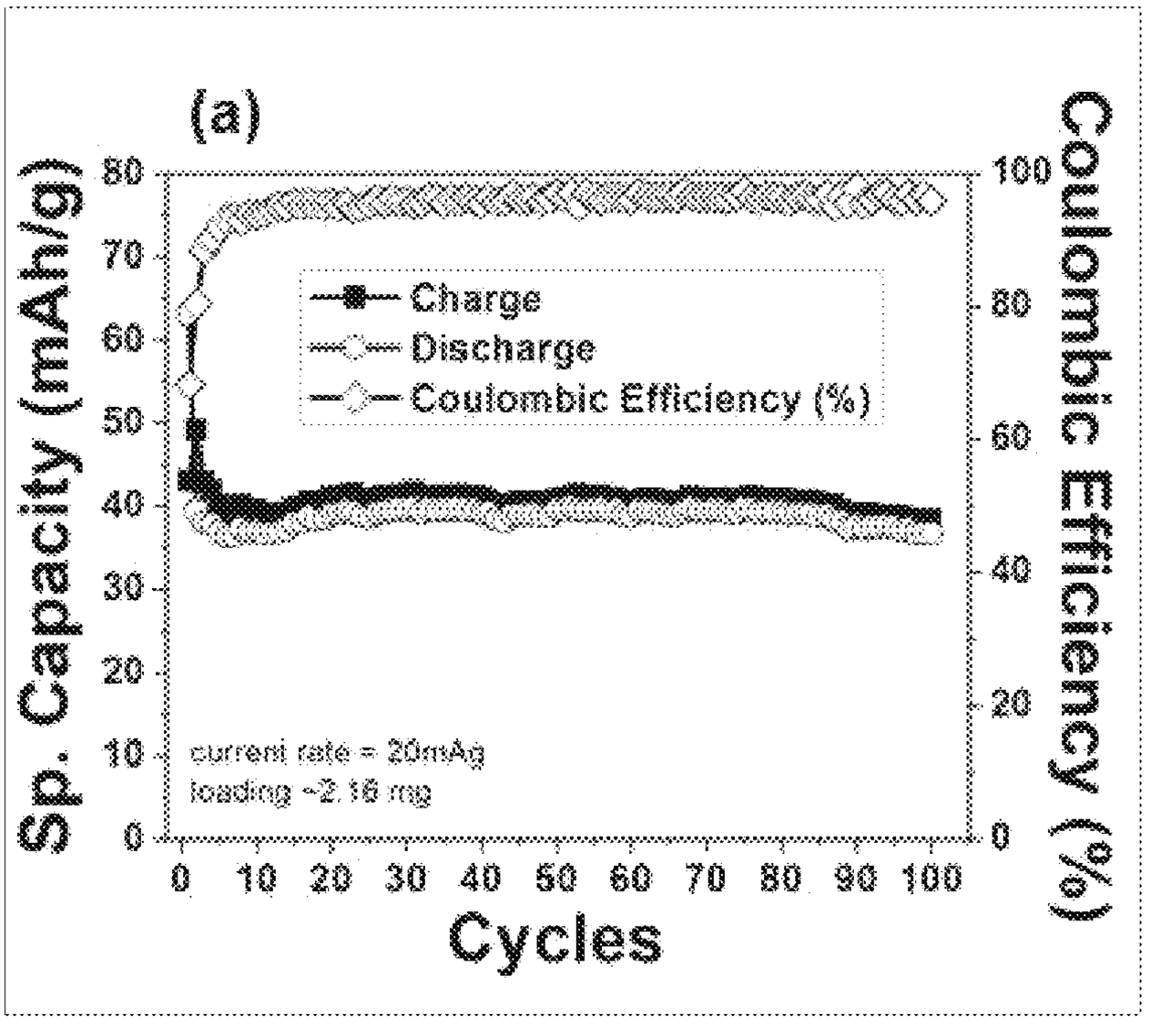
(a)
Sp. Capacity (mAh/g)
Coulombic Efficiency (%)
Charge
Discharge
Coulombic Efficiency (%)
current rate = 20mAg
loading ~2.16 mg
Cycles
0
10
20
30
40
50
60
70
80
90
100

FIG 8a

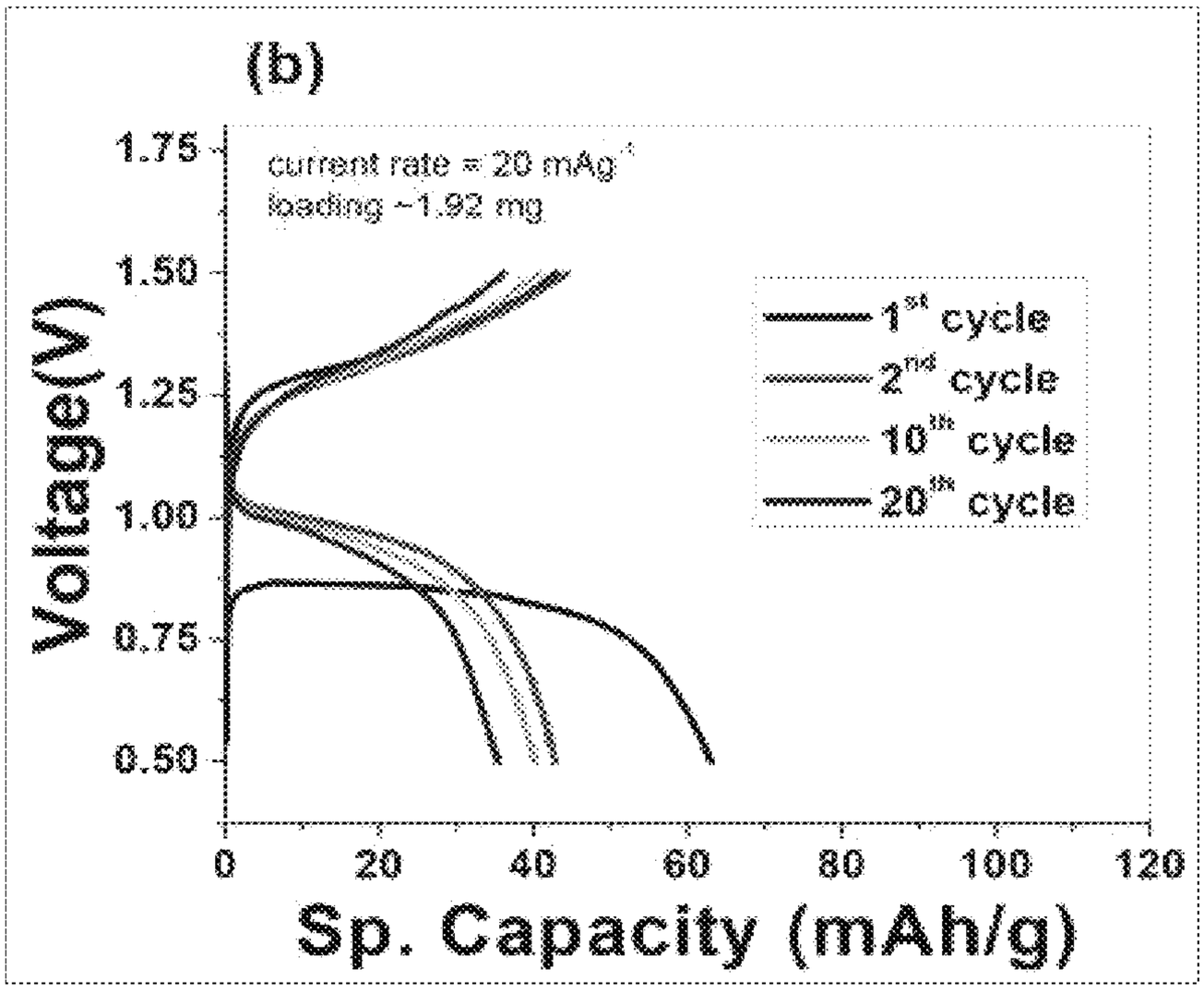
(b)
current rate = 20 mAg-1
loading ~1.92 mg
1st cycle
2nd cycle
10th cycle
20th cycle
Voltage(V)
1.75
1.50
1.25
1.00
0.75
0.50
0
20
40
60
80
100
120
Sp. Capacity (mAh/g)

FIG 8b

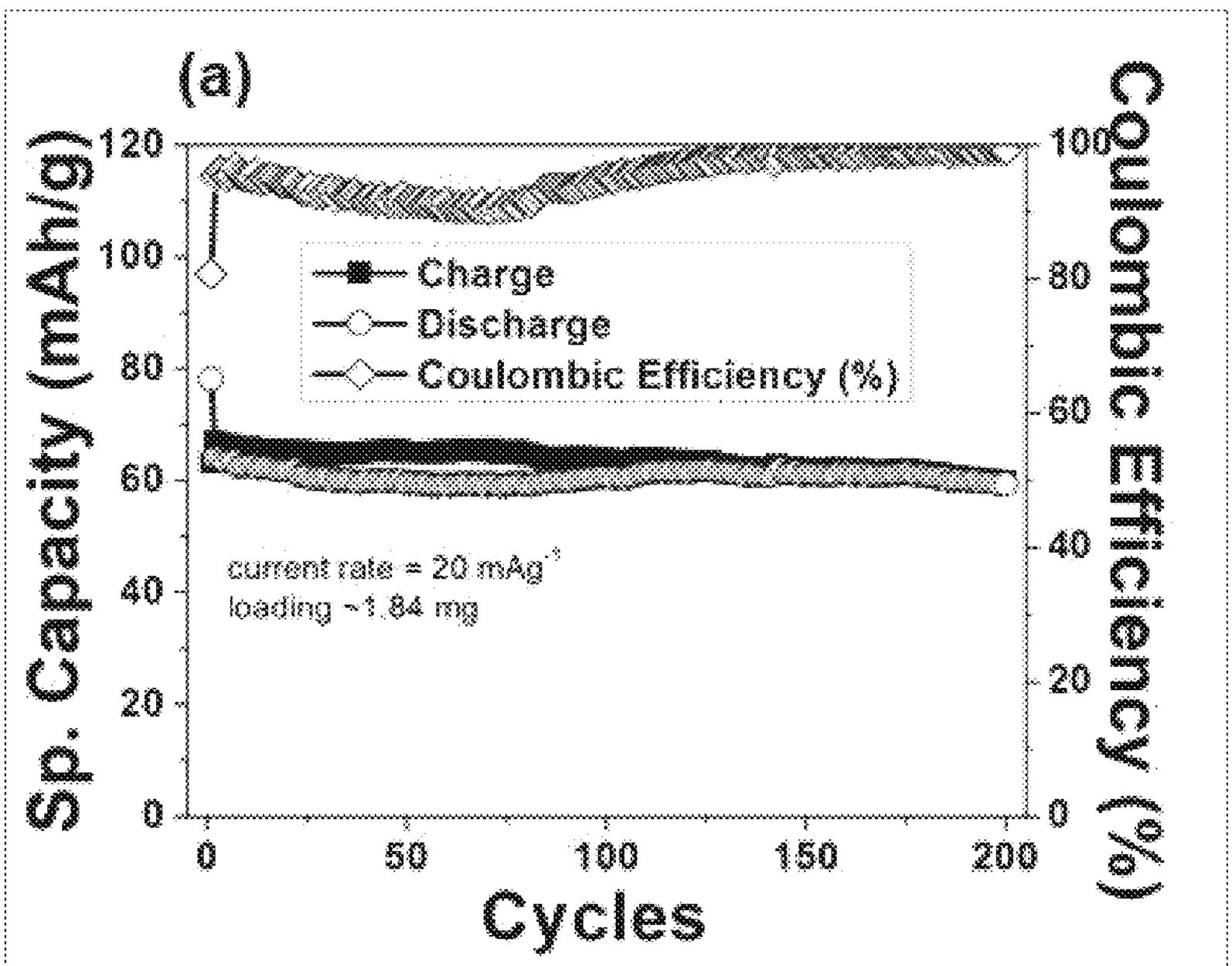
(a)
Sp. Capacity (mAh/g)
Coulombic Efficiency (%)
Cycles
Charge
Discharge
Coulombic Efficiency (%)
current rate = 20 mAg-1
loading ~1.84 mg
0
20
40
60
80
100
120
0
20
40
60
80
100
0
50
100
150
200

FIG 9a

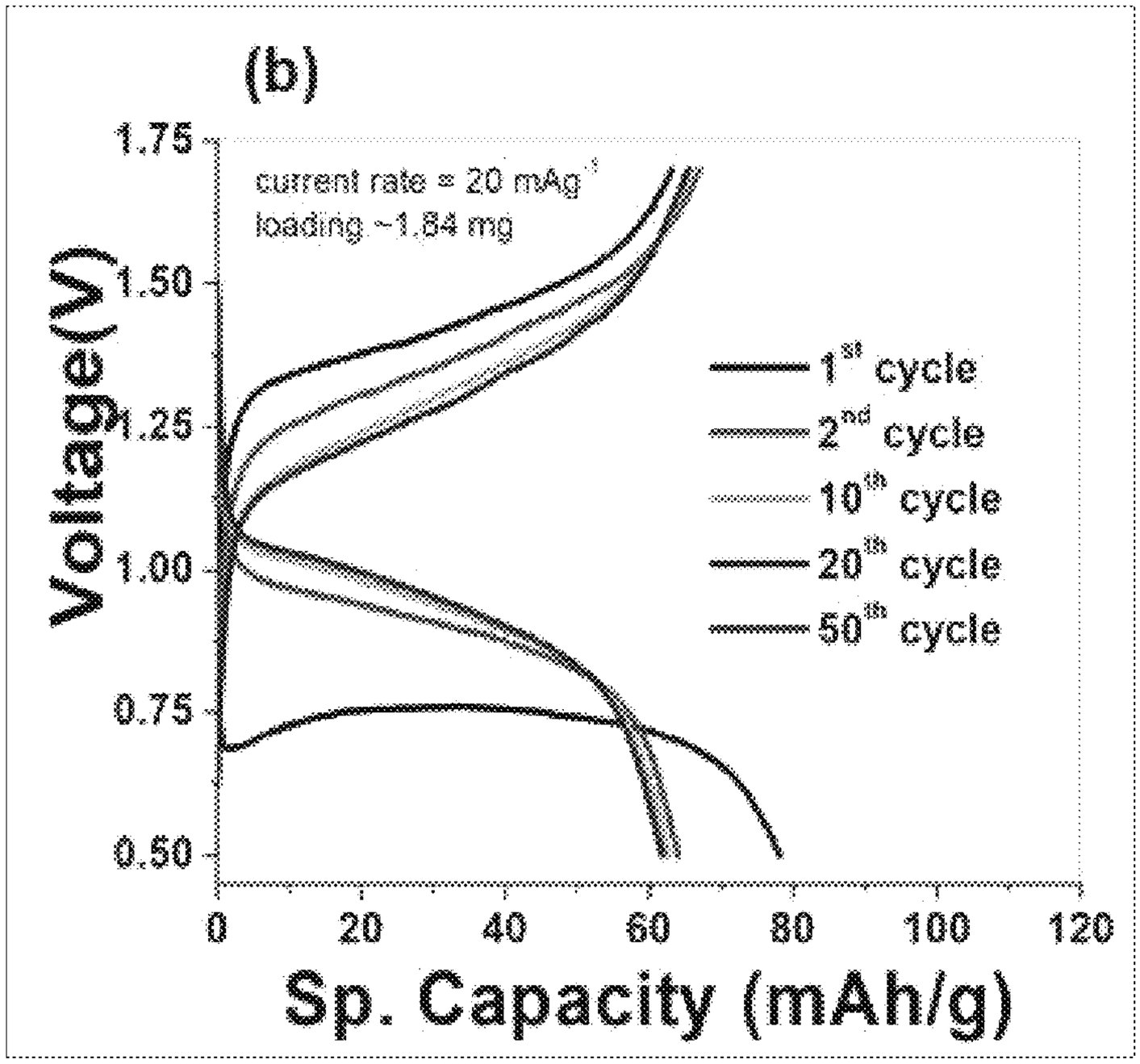
(b)
current rate = 20 mAg-1
loading ~1.84 mg
Voltage(V)
1.75
1.50
1.25
1.00
0.75
0.50
0
20
40
60
80
100
120
Sp. Capacity (mAh/g)
1st cycle
2nd cycle
10th cycle
20th cycle
50th cycle

FIG 9b

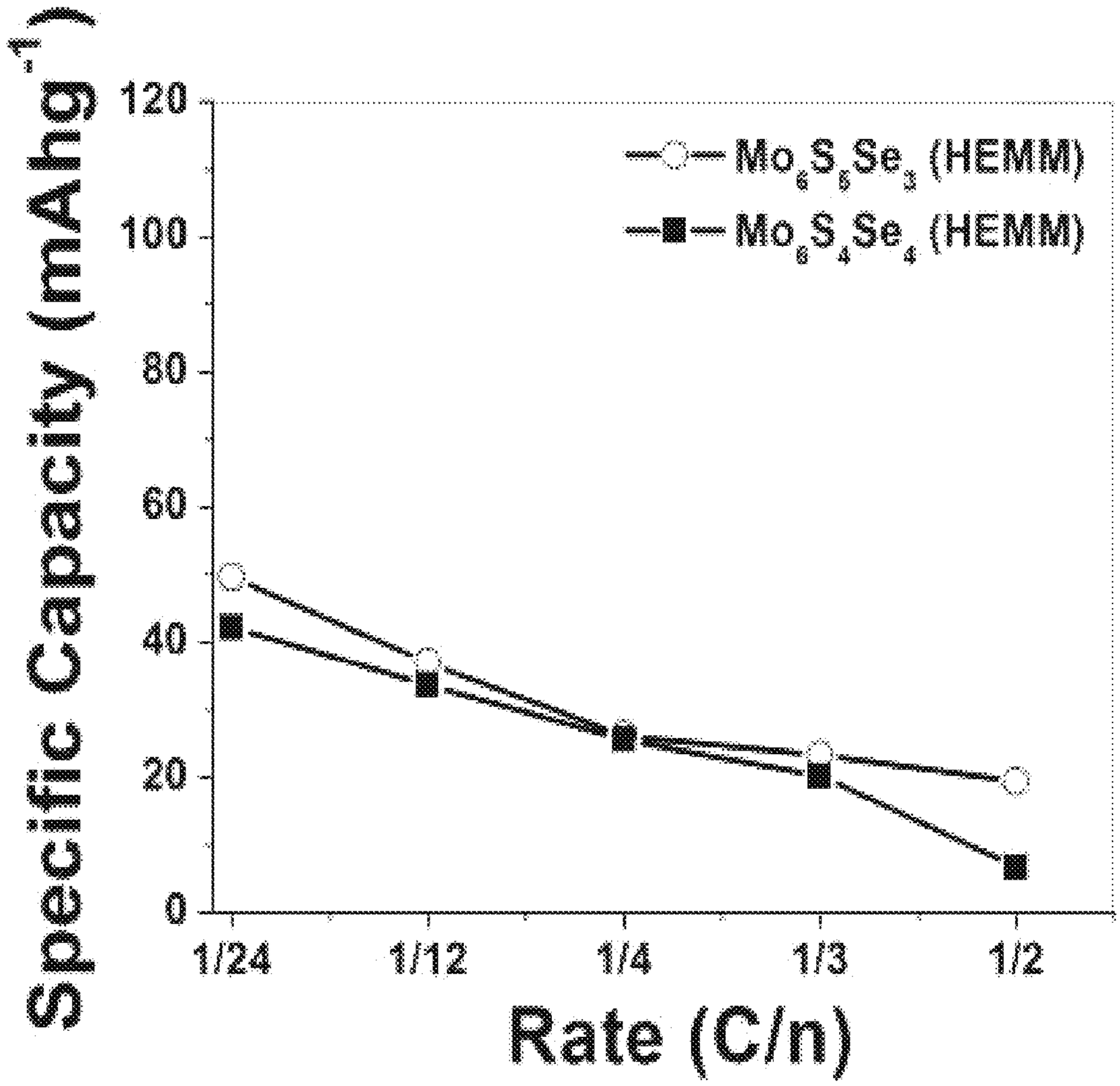
Specific Capacity (mAhg-1)
120
100
80
60
40
20
0
1/24
1/12
1/4
1/3
1/2
Rate (C/n)
Mo6S6Se2 (HEMM)
Mo6S4Se4 (HEMM)

FIG 10

CATHODES AND ELECTROLYTES FOR RECHARGEABLE MAGNESIUM BATTERIES AND METHODS OF MANUFACTURE

CROSS-REFERENCE TO RELATED APPLICATIONS

This continuation-in-part patent application claims priority from divisional U.S. patent application Ser. No. 15/897,721, filed Feb. 15, 2018, which claims priority from U.S. patent application Ser. No. 14/325,891, filed Jul. 8, 2014, which claims priority under 35 U.S.C. § 119(e) to U.S. Provisional Patent Application Ser. No. 61/843,647, filed Jul. 8, 2013, entitled "Cathodes and Electrolytes for Rechargeable Magnesium Batteries and Methods of Manufacture", which are herein incorporated by reference.

GOVERNMENT FUNDING

This invention was made with government support under grant #DE-FE0004000 awarded by the Department of Energy-NETL. The government has certain rights in the invention.

1. FIELD OF THE INVENTION

The invention relates to Chevrel-phase materials and methods for their preparation, and to secondary electrochemical cells utilizing a magnesium-containing anode and a Chevrel-phase-containing cathode.

2. BACKGROUND

High energy density, rechargeable electrochemical cells are known in the art. A rechargeable cell is theoretically capable of charging and discharging indefinitely. In producing a rechargeable battery system, a material for the cathode is selected. In certain instances, the cathode material is in the form of a liquid which allows reactions to readily take place. However, when in the form of a liquid, provisions are made to keep the cathode active material away from the anode, otherwise self-discharge can occur. As an alternative, the cathode material can be in the form of a solid which is essentially insoluble in the electrolyte. The solid cathode material is selected such that it absorbs and desorbs the anode ion because solubility of the anode ion occurs reversibly during operation of the cell. Such a solid cathode can be capable of intercalation of ions which are solubilized by the electrolyte. The electrolyte is selected to permit electroplating of solubilized ions at the anode. The plating of ions at the anode occurs during recharge of the cell and the intercalation of the cathode occurs during discharge of the cell.

Chevrel-phase compounds (CPs), also referred to as Chevrel materials, include an invariant portion which may consist essentially of molybdenum and a chalcogen. The chalcogen can be selected from elements in Group 16 of the Periodic Table, including sulfur, selenium, tellurium or mixtures of these, with or without minor amounts of oxygen. Ordinarily, this fixed portion has a stoichiometric formula of Mo_6Z_y where Z represents the chalcogen and y is usually between about 7.5 and 8.5, most typically about 8. The unique crystal structure of the materials permits intercalation of metals, so that the overall stoichiometry of the Chevrel-phase material is represented as $M_xMo_6Z_y$ where M represents the intercalated metal and 'x' may vary from 0 (no intercalated metal) to an upper limit which may be about 4 or less depending upon the particular metal.

Ternary CPs are a unique class of cluster compounds which exhibit remarkable magnetic, thermoelectric, catalytic, and superconductive properties. The crystal structure of CPs consists of Mo_6-octahedron clusters surrounded by eight chalcogen (e.g., S and/or Se) atoms at the corners of a distorted cube. For example, Mo_6S_8 units are linked with each other and form a three-dimensional framework with open cavities/channels that can be filled with wide-variety of guest atoms and form ternary CPs $M_xMo_6S_8$ ($0<x<4$). However, Mo_6S_8 binary CPs cannot be synthesized directly and indirectly stabilized via leaching metal from their ternary counterparts. For example, Mo_6Se_8 binary CPs include an iso-structure wherein Mo_6Se_8 clusters are rotated approximately 26° about the body diagonal ($\bar{3}$ axis) of the rhombohedral symmetry ($R\bar{3}$) which allows for bonding of Se atoms of one cluster to a Mo atom of a neighboring unit. The resultant three-dimensional Mo_6Se_8 framework has open cavities/sites that can be filled completely in the $M_xMo_6Se_8$ CPs into triclinic ($P\bar{1}$) forms due to intrinsic lattice instabilities. Among the three different families of CPs (Mo_6Z_8, Z=S, Se, Te), sulfide CPs have high ionic mobility at room temperature which allows them to transport monovalent (Li^+, Na^+) and bivalent (Mg^{2+}) cations, and to act as a cathode for rechargeable batteries.

Energy is released upon intercalation of the metal into the CPs and as the intercalation process is partially or wholly reversible with certain metals, the CPs can therefore be used as cathodes in electrochemical cells.

A cell with a lithium anode and a Chevrel-phase cathode of the formula $Li_xMo_6S_8$, for example, can be subjected to a charge cycle in which lithium is removed from the Chevrel-phase by the applied electrical energy. In a discharge cycle, the lithium is re-intercalated into the Chevrel-phase releasing energy as electrical energy. The reaction mixture containing lithium, molybdenum and sulfur for direct formation of the lithium-intercalated CPs can be prepared by heating a precursor mixture. The precursor mixture including a heat-liable lithium compound together with molybdenum and sulfur, typically as a mixture of MoS_2 and free Mo. Upon heating, the heat-labile compound yields volatile decomposition products which may be swept from the mixture, e.g., by a stream of inert gas, leaving behind the lithium, molybdenum and sulfur to form the Chevrel-phase material.

Intercalation reactions in typical battery development have focused on the use of alkali metals, specifically lithium as anodes. In comparison, there has been less research with respect to the use of alkaline earth metals, such as magnesium, for use as anodes and the use of cathodes capable of intercalation of alkaline earth metal ions.

It is known in the art to use lithium ion batteries for a wide variety of energy storage applications due to their very high energy density and flexible design. In considering alternative materials to lithium in producing electrochemical batteries, it is acknowledged that magnesium-based energy storage systems may be considered suitable alternatives because magnesium is environmentally safe, cost effective and abundant in the earth's crest. Further, magnesium is bivalent and theoretically capable of rendering higher volumetric capacity than lithium.

It has been found that conventional salts such as $Mg(ClO_4)_2$, $Mg(CF_3SO_3)_2$, $Mg[(CF_3SO_2)_2N]_2$ and the like, dissolved in various non-aqueous solvents develop surface passivation on a magnesium anode and effectively block Mg^{2+} transport. Relatively fast and easy intercalation of Mg^{2+} ions at room temperature makes CPs a preferred material of the cathode for magnesium batteries. However,

synthesis of the thermodynamically unstable Mo_6S_8 phase is challenging. Typically, a CuCP ($Cu_xMo_6S_8$) is synthesized by solid state reactions of elemental blends of copper, molybdenum, and MoS_2 powders in an evacuated quartz ampoules at a temperature of approximately 1150° C. for one week or by a molten salt approach including heat treatment at approximately 850° C. for about 60 hours under an argon atmosphere. Both of these approaches require chemical leaching in solution for several days at room temperature for complete removal of the copper.

The conventional methods utilized are not convenient approaches that can be readily and effectively translated into large scale manufacturing processes for generating the Chevrel phase. For example, an elemental blend sealed in evacuated quartz ampoule and heated at high temperature (~1273 K) for a long duration (~7 days) to obtain $Cu_xMo_6S_8$ results in high manufacturing costs not withstanding generating reproducible large scale quantities. Further, a significant disadvantage is the high vapor pressure of sulfur inside the ampoule during heating which causes a safety hazard. Furthermore, the final product obtained from the quartz ampoule has non-stoichiometry due to sulfur volatilization and condensation on the ampoule walls further from the product and excess sulfur that may be hence required to compensate for sulfur vapor loss during heating. Attempts to use metal sulfide (CuS, MoS_2) instead of elemental sulfur to avoid the high vapor pressure, has resulted in long and arduous synthesis time which is unreasonably long and thus not amenable large-scale production. Moreover, it was found that there can be difficulty in forming a reaction product at high temperature, e.g., the Chevrel phase may not be obtained and instead a sulfur deficient phase can form which adversely affects the desired and expected electrochemical performance.

In an attempt to reduce total synthesis time duration involved during the solid-state reaction method, cold-pressing and hot pressing have been employed as alternative means for the synthesis of a $Cu_xMo_6S_8$ phase. Neither the milling time nor the sintering temperature has been optimized for the synthesis of $Cu_xMo_6S_8$. However, it was found that pressure-assisted sintering at elevated temperature ~1123-1473 K was capable of reducing the synthesis duration to ~5-8 hours as compared to 7 days required for solid-state synthesis in an evacuated quartz ampoule.

The desired CPs also have been synthesized from soluble sulfide precursor, e.g., polythiomolybdate and metal salt, which form a chelated complex in ether or methanol solvent and directly forms the desired $Cu_2Mo_6S_8$ phase when heated at ~1073-1273 K under hydrogen atmosphere. An alternative soluble precursor method was proposed for the synthesis of nickel and lithium ternary CPs.

Obtaining Mo_6S_8 CPs from known soluble sulfide precursor methods requires the use of hydrogen gas during sulfurization. Final reduction of sulfur compounds to desired Chevrel phase at elevated temperature needs strict regulation and skills, and poses a safety concern for the synthesis of CPs.

Thus, there is a need for improvements in electrochemical cells incorporating Chevrel-phase cathodes and in the synthesis methods for the CPs, and furthermore, in the use of alkaline earth metals, such as magnesium, as anodes. Moreover, there is a need in the art to develop time-saving economical approaches and methods for the direct synthesis of CPs. In this respect, high energy mechanical milling (HEMM) is employed as a scalable, economical time-saving approach for the direct synthesis of ternary metal CPs ($M_xMo_6Z_8$ and $M_xMo_6Z^1{}_{8-y}Z^2{}_y$, wherein, for example, Z is S or Se, Z^1 is S and Z^2 is Se) using MZ, Mo and MoZ_2 or MZ^1, MZ^2, Mo, $MoZ_2{}^1$ and $MoZ_2{}^2$ as the precursor. The invention provides easy, rapid and facile precursor approaches for the synthesis of CPs for use as a cathode and magnesium-containing material for use as an anode in an electrochemical cell.

SUMMARY OF THE INVENTION

In one aspect, the invention provides an electrochemical cell including an alkali metal-containing anode, a cathode and an electrolyte. The cathode includes a Chevrel-phase material of a formula $Mo_6Z^1{}_{8-y}Z^2{}_y$ derived from a precursor material of a formula $M_xMo_6Z^1{}_{8-y}Z^2{}_y$ wherein M is a metallic element, x is a number from greater than 0 to 4, y is a number from greater than 0 to less than 8, and each of Z^1 and Z^2 is a chalcogen with or without the presence of oxygen, wherein Z^1 is a different chalcogen than Z^2.

In certain embodiments, the alkali-metal-containing anode comprises magnesium.

In certain embodiments, the metallic element M can be selected from Li, Na, Mg, Ca, Sc, Cr, Mn, Fe Co, Ni, Cu, Zn, Sr, Y, Pd, Ag, Cd, In, Sn, Ba, La, Pb, Ce, Pr, Nd, Sm, Eu, Gd, Tb, Dy, Ho, Er, Tm, Yb, Lu and mixtures thereof.

Each of the chalcogens Z^1 and Z^2 can be selected from chemical elements in Group 16 of the Periodic Table, including sulfur, selenium, tellurium and mixtures thereof. Further, each of Z^1 and Z^2 can be sulfur, selenium, tellurium or a mixtures thereof, with or without the presence of oxygen. Wherein, Z^1 is a different chalcogen than Z^2.

In certain embodiments, M is copper, x is 2, Z^1 is sulfur, and Z^2 is selenium.

The precursor material can be formed from a mixture of MZ^1, MZ^2, $MoZ_2{}^1$, $MoZ_2{}^2$ and molybdenum.

The Chevrel-phase material can be of the formula $Mo_6S_{8-y}Se_y$ which is derived from a precursor material of $Cu_2Mo_6S_{8-y}Se_y$ and the said precursor material $Cu_2Mo_6S_{8-y}Se_y$ which can be derived from a mixture of ammonium tetrathiomolybdate and anhydrous $CuCl_2$ in the presence of anhydrous N,N-dimethylformamide.

The electrolyte can be in the form of an electrolyte solution including electrolyte metal salt and the desired solvent. In certain embodiments, the electrolyte solution includes amidomagnesium-based magnesium salt transmetallated with an aluminum salt electrolyte dissolved in the solvent. In other embodiments, the electrolyte solution includes phenyl magnesium chloride-aluminum chloride, amidomagnesium-based magnesium salt transmetallated with an aluminum salt electrolyte, and solvent. The solvent can be tetrahydrofuran.

In yet other embodiments, the electrolyte solution includes 3-bis(trimethylsilyl)aminophenylmagnesium chloride with aluminum chloride in tetrahydrofuran.

The electrochemical cell can be a rechargeable battery.

In another aspect, the invention provides a method of synthesizing a Chevrel-phase cathode material. The method includes preparing a precursor material of a formula $M_xMo_6Z^1{}_{8-y}Z^2{}_y$, wherein M is a metallic element, x is a number from greater than 0 to 4, y is a number from greater than 0 to less than 8, each of Z^1 and Z^2 is a chacogen with or without the presence of oxygen, wherein Z^1 is a different chalcogen than Z^2, and removing the metallic element from the precursor material to form a Chevrel-phase cathode material of a formula $Mo_6Z^1{}_{8-y}Z^2{}_y$.

Each of Z^1 and Z^2 can be selected from the group consisting of sulfur, selenium, tellurium, wherein Z^1 is a different chalcogen than Z^2.

In certain embodiments, preparing the precursor material includes combining stoichiometric amounts of MZ^1, MZ^2, MoZ_2^1, MoZ_2^2 and molybdenum. Furthermore, preparing the precursor material can include combining stoichiometric amounts of ammonium tetrathiomolybdate, anhydrous copper chloride and N,N dimethylformamide to form the desired mixture. Furthermore, preparing the precursor material can include heating the mixture to at least substantially complete reaction, filtering, precipitating, drying the precipitate to yield a precursor material of a formula $M_2Mo_6Z^1_{8-y}Z^2_y$, completely or partially removing M ions, and drying to obtain the Chevrel-phase cathode material of $Mo_6Z^1_{8-y}Z^2_y$.

In other embodiments, preparing the precursor material includes combining stroichiometric amounts of copper (II) sulfide, copper (II) selenide, molybdenum, molybdenum disulfide and molybdenum selenide. Further, preparing the precursor material can include high energy mechanical milling the mixture to form a powder, heating the mechanically milled powder to at least substantially complete the reaction, yielding a precursor material of a formula $M_2Mo_6Z^1_{8-y}Z^2_y$, completely or partially removing the M ions, and drying to obtain the Chevrel-phase cathode material of a formula $Mo_6Z^1_{8-y}Z^2_y$. In another aspect, the invention provides a method of preparing an electrode.

In another aspect, the invention provides an electrode. The electrode includes a slurry and a current collector, wherein the slurry is at least partially deposited onto the current collector to form a coating thereon. The slurry includes a Chevrel-phase cathode material of a formula $Mo_6Z^1_{8-y}Z^2_y$.

The current collector can be a material substrate selected from the group consisting of copper, graphite, nickel, platinum, quartz, gold, stainless steel, tantalum, titanium, silver and mixtures thereof. In certain embodiments, the current collector is graphite foil.

BRIEF DESCRIPTION OF THE DRAWINGS

FIG. **1** is a plot that shows powder XRD pattern of $Cu_2Mo_6S_8$ (Cu_2CP) (top) obtained by high energy mechanical milling of CuS, MoS_2, and Mo corresponding to the stoichiometric compositions followed by heat treatment at 1000° C./5 h under UHP Ar, and acid leached $Cu_1Mo_6S_8$ (Cu_1CP) (bottom) obtained after 2 days to partially leach copper using 6 M HCl solution, in accordance with certain embodiments of the invention;

FIG. **2***a* is a plot that shows cycling data, FIG. **2***b* is a plot that shows galvanostatic discharge-charge profile, and FIG. **2***c* is a plot that shows rate capability of the synthesized $Cu_1Mo_6S_8$ electrode following leaching of Cu_2CP when cycled against magnesium in Mg-ion battery, in accordance with certain embodiments of the invention;

FIG. **3***a* is a plot that shows a galvanostatic discharge-charge profile of Cu_1CP electrode at 1^{st}, 2^{nd}, and, 3^{rd} cycle carried out at ~5 mAg^{-1} current rate within the potential window of 0.5-15 V, FIG. **3***b* is a plot that shows differential capacity, dQ/dV versus voltage (V) curves of 2^{nd} and 3^{rd} cycle, FIG. **3***c* is a plot that shows ex-situ XRD analysis at 0.5V and 1.5V cut-off voltage during charge/discharge cycles, and FIG. **3***d* is a plot that shows cycling data of Cu_1CP performed at a slow current rate of ~5 mAg^{-1} within 0.5-1.5V potential window in a Mg-ion cell, in accordance with certain embodiments of the invention.

FIG. **4** is a plot that shows XRD patterns collected on the powders obtained following mechanically milling for 1 h, 2 h, and 3 h using stoichiometric amounts of the individual elements, sulfide and selenide precursors corresponding to $Cu_2Mo_6S_7Se_1$ stoichiometry and also on powders obtained after heat-treating at 1000° C. for 5 h showing the formation of $Cu_2Mo_6S_7Se_1$ and acid leached $Mo_6S_7Se_1$, respectively, in accordance with certain embodiments of the invention;

FIG. **5***a* is a plot that shows a cyclic voltammogram (CV) curve obtained with a sweep rate of ~50 μVs^{-1} showing Mg-ion insertion/extraction into/from the synthesized $Mo_6S_7Se_1$ electrode, FIG. **5***b* is a plot that shows galvanostatic cycling data at a current rate of ~20 mAg^{-1}, FIG. **5***c* is a plot that shows capacity versus voltage profiles, and FIG. **5***d* is a plot that shows differential capacity versus voltage (dQ/dV versus V) curves for the 2^{nd}, 50^{th}, and 200^{th} cycles, in accordance with certain embodiments of the invention;

FIGS. **6***a*, **6***b* and **6***c* are plots that show XRD patterns collected on the powders after mechanically milling for 1 h, 2 h, and 3 h corresponding to the stoichiometric ratio of $Cu_2Mo_6S_{8-x}Se_x$ (x=3, 4, 5) and after heat treating at 1000° C. for 5 h showing the formation of (a) $Cu_2Mo_6S_5Se_3$ and acid leached $Mo_6S_5Se_3$, (b) $Cu_2Mo_6S_4Se_4$ and acid leached $Mo_6S_4Se_4$, and (c) $Cu_2Mo_6S_3Se_5$ and acid leached $Mo_6S_3Se_5$, respectively, in accordance with certain embodiments of the invention;

FIG. **7***a* is a plot that shows galvanostatic cycling data and FIG. **7***b* is a plot that shows capacity versus voltage profiles obtained at a current rate of ~20 mAg^{-1} cycled between 0.5-1.5V for $Mo_6S_5Se_3$ electrodes using the 0.4 molar 2(PhMgCl—$AlCl_3$)/tetrahydrofuran electrolyte, in accordance with certain embodiments of the invention;

FIG. **8***a* is a plot that shows galvanostatic cycling data and FIG. **8***b* is a plot that shows capacity versus voltage profiles performed at a current rate of ~20 mAg^{-1} between 0.5-1.5 V for $Mo_6S_4Se_4$ electrodes using the 0.4 molar 2(PhMgCl—$AlCl_3$)/tetrahydrofuran electrolyte, in accordance with certain embodiments of the invention;

FIG. **9***a* is a plot that shows galvanostatic cycling data and FIG. **9***b* is a plot that shows capacity versus voltage profiles performed at a current rate of ~20 mAg^{-1} between 0.5-1.75 V for $Mo_6S_3Se_8$ electrodes using the 0.4 molar 2(PhMgCl—$AlCl_3$)/tetrahydrofuran electrolyte, in accordance with certain embodiments of the invention; and

FIG. **10** is a plot that shows rate capabilities of $Mo_6S_5Se_3$ and $Mo_6S_4Se_4$ electrodes in a Mg-ion battery, in accordance with certain embodiments of the invention.

DETAILED DESCRIPTION OF THE PREFERRED EMBODIMENTS

The invention relates to Chevrel-phase materials, such as ternary molybdenum chalcogenide compounds. The Chevrel-phase materials, also referred to as Chevrel-phase compounds, in accordance with the invention have the formula Mo_6Z_8, wherein Mo represents molybdenum and Z represents a chalcogen, or $Mo_6Z^1_{8-y}Z^2_y$, wherein Mo represents molybdenum and each of Z^1 and Z^2 represents a first chalcogen and a different second chalcogen, respectively. The invention further relates to electrochemical cells incorporating a cathode which includes a Chevrel-phase material, an anode which includes an alkali metal, and an electrolyte.

The Chevrel-phase materials of the formula Mo_6Z_8 or $Mo_6Z^1_{8-y}Z^2_y$ are prepared using various techniques and methods. In accordance with certain embodiments of the invention, the Chevrel-phase materials are derived from said precursor materials. The precursor materials have the formula $M_xMo_6Z_8$, wherein M is a metallic element, 'x' is a number from greater than 0 to 4, and Z is a chalcogen, e.g.,

chalcogenide, or the formula $M_xMo_6Z^1_{8-y}Z^2_y$, wherein M is a metallic element, 'x' is a number from greater than 0 to 4, 'y' is a number from greater than 0 to less than 8, and each of Z^1, and Z^2 is a chacogen, e.g., chalcogenide, wherein Z^1 is a different chalcogen than Z^2.

The said precursor materials of the formulas $M_xMo_6Z_8$ or $M_xMo_6Z^1_{8-y}Z^2_y$ are formed using various methods. In accordance with certain embodiments of the invention, the precursor materials are formed by combining metal sulfides (MZ and MoZ_2, or MZ^1, MZ^2, $MoZ_2{}^1$ and $MoZ_2{}^2$) with molybdenum (Mo). Further, in certain embodiments, the metal sulfides (MZ and MoZ_2, or MZ^1, MZ^2, $MoZ_2{}^1$ and $MoZ_2{}^2$) and molybdenum (Mo) metal are subjected to high energy mechanical milling (HEMM) and during the ensuing milling process, the individual materials mentioned react resulting in forming the precursor materials.

In certain embodiments, the alkali metal is magnesium. Thus, the electrochemical cells in accordance with certain embodiments of the invention include a magnesium or magnesium-containing anode.

It is contemplated and understood that M includes a wide variety of metallic elements that are known to one having ordinary skill in the art. In certain embodiments, the metallic element is selected from Li, Na, Mg, Ca, Sc, Cr, Mn, Fe Co, Ni, Cu, Zn, Sr, Y, Pd, Ag, Cd, In, Sn, Ba, La, Pb, Ce, Pr, Nd, Sm, Eu, Gd, Tb, Dy, Ho, Er, Tm, Yb, Lu and mixtures thereof.

The chalcogens Z, Z^1 and Z^2 are selected from those known to one having ordinary skill in the art. In certain embodiments, the chalcogens Z, Z^1 and Z^2 are selected from the chemical elements in Group 16 of the Periodic Table, including sulfur, selenium, tellurium and mixtures thereof. Further, in certain embodiments, each of Z, Z^1 and Z^2 is sulfur, selenium, tellurium or a mixture thereof, with or without the presence of oxygen. Typically, the oxygen when present is in a small or trace amount. As aforementioned, Z^1 is a first chalcogen and Z^2 is a different second chalcogen.

In accordance with certain embodiments of the precursor approach for use in preparing Chevrel-phase materials, stoichiometric amounts of MZ, MoZ_2 and Mo, or stoichiometric amounts of MZ^1, MZ^2, $MoZ_2{}^1$, $MoZ_2{}^2$ and Mo are combined to form a mixture. The mixture is heated to complete the desired reaction or at least to substantially complete the desired reaction. The heating can be accomplished by various conventional mechanisms known in the art. For example, heating can be conducted over a hot plate at a temperature of about 90° C. under nitrogen bubbling. Following heating, the mixture is filtered using conventional techniques known in the art. Tetrahydrofuran (or any other known suitable solvent material) is added to the filtrate to initiate incipient precipitation. The resulting precipitate is washed in accordance with known techniques, e.g., with tetrahydrofuran and alcohol, e.g., methanol, and then dried using known techniques, e.g., at a temperature of about 60° C.

In certain embodiments, the dried product is ground and heated in an argon (or the like) atmosphere at about 1000° C. to yield metallic Chevrel-phase precursor material, e.g., $M_2Mo_6Z_8$ or $M_2Mo_6Z^1_{8-y}Z^2_y$.

The metals, e.g., metallic ions, are leached out using conventional mechanisms. For example, the metallic ions can be removed under an ambient atmosphere using a solution of HCl/O_2 bubbling. The solution is then centrifuged, washed and dried using known methods and techniques to yield the final Chevrel-phase product, e.g., Mo_6Z_8 or $Mo_6Z^1_{8-y}Z^2_y$.

In certain embodiments, the starting materials for use in forming the precursor material can be subjected to high energy mechanical milling (HEMM). Accordingly, appropriate amounts of MZ, MoZ_2 and Mo, or appropriate amounts of MZ^1, MZ^2, $MoZ_2{}^1$, $MoZ_2{}^2$ and Mo are charged into a HEMM apparatus. The HEMM process is carried out for a defined period of time which can vary. The time period can be as short in duration as thirty minutes or as long as one or two or three hours or even more as needed not extending beyond few hours to initiate and complete the reaction. The HEMM process is subsequently followed by annealing at an elevated temperature under ultra high purity (UHP) argon atmosphere. The temperature can vary and may be maintained from about 1123 to about 1273K.

An advantage of employing the HEMM process is that no vacuum or silica ampoule is required for the synthesis due to complete absence of elemental sulfur/selenium in the starting composition. Further, there is no loss or gain in mass between the Chevrel-phase product and the precursor reactants. The ternary Chevrel phase can be formed directly from the ball-milled or mechanically milled powder upon annealing, a major advantage of the invention. In certain embodiments, the annealing is carried out a temperature that is about 1073 K or greater in a corundum crucible in a tubular furnace.

In certain embodiments, M is copper, 'x' is 2 and Z is sulfur. The precursor material is $Cu_2Mo_6S_8$ which is formed by the combination and reaction of CuS, MoS_2 and Mo. The Chevrel-phase material has the formula of Mo_6S_8 and is derived from the precursor material $Cu_2Mo_6S_8$ followed by removing the copper or copper ions therefrom by subsequent acid leaching. Suitable materials for use in forming the precursor material can include a mixture of stoichiometric amounts of ammonium tetrathiomolybdate and anhydrous copper chloride ($CuCl_2$) in the presence of anhydrous N,N-dimethylformamide. For example, formation of the Chevrel-phase material can be conducted according to the formula: $2CuS+3Mo+3MoS_2=Cu_2Mo_6S_8$. For ease of description, much of the disclosure is directed to the chalcogen being sulfur (i.e., Z represents S) and the metallic element is copper (i.e., M represents Cu). However, it is understood that in accordance with the invention, the chalcogen is not limited to sulfur and the metallic element is also not limited to copper.

In certain other embodiments, M is copper, 'x' is 2, Z^1 is sulfur, Z^2 is selenium and 'y' is a number from greater than 0 to less than 8. The precursor material is $Cu_2Mo_6S_{8-y}Se_y$ which is formed by the reaction of a combination of CuS, CuSe, MoS_2, $MoSe_2$ and Mo. The Chevrel-phase material has the formula of $Mo_6S_{8-y}Se_y$ and is derived from the precursor material $Cu_2Mo_6S_{8-y}Se_y$ followed by removing the copper or copper ions therefrom by subsequent acid leaching. Suitable materials for use in forming the precursor material can include a mixture of stoichiometric amounts of ammonium tetrathiomolybdate and anhydrous copper chloride ($CuCl_2$) in the presence of anhydrous N,N-dimethylformamide. For example, formation of the Chevrel-phase material can be conducted according to the formulas: $Cu_2Mo_6S_8$ (Cu_2CP); $Cu_1Mo_6S_8$ (Cu_1CP); $Cu_2Mo_6S_7Se_1$ (Cu_2CPSe_1); $Mo_6S_7Se_1$; $Cu_2Mo_6S_{8-x}Se_x$ (x=3, 4, 5), $Cu_2Mo_6S_5Se_3$ (Cu_2CPSe_3); $Mo_6S_5Se_3$, $Cu_2Mo_6S_4Se_4$ (Cu_2CPSe_4); $Mo_6S_4Se_4$, $Cu_2Mo_6S_3Se_5$ (Cu_2CPSe_5); $Mo_6S_3Se_5$. For ease of description, much of the disclosure is directed to the chalcogens being sulfur and selenium (i.e., Z^1 represents S, and Z^2 represents Se) and the metallic element is copper (i.e., M represents Cu). However, it is understood that in accordance with the invention, the chalcogens are not

limited to only sulfur and selenium, and the metallic element is not limited to only copper. The $Mo_6S_{8-y}Se_y$ units are linked with each other and form a three-dimensional framework with open cavities/channels that can be filled with wide-variety of guest atoms and form ternary CPs $M_xMo_6S_{8-y}Se_y$ ($0<x<4$ and $0<y<8$).

In general, the precursor approach includes preparing a precursor material which includes a metallic element and the metallic element (or ions thereof) is subsequently completely or partially removed (e.g., leached out) to produce the said Chevrel-phase product for use as cathode material.

The Chevrel-phase material synthesized in accordance with the above-described precursor approach can be employed to prepare and fabricate an electrode, i.e., cathode, using conventional techniques and apparatus. For example, an electrode slurry containing the Chevrel-phase material of the invention can be prepared and deposited on a current collector, and then subsequently dried. The current collector can include a wide variety of suitable materials known by one having ordinary skill in the art. Non-limiting examples include but are not limited to copper, graphite, nickel, platinum, quartz, gold, stainless steel, tantalum, titanium, silver, and mixtures thereof. In certain embodiments, the current collector is also graphite foil (grafoil). Deposition of the slurry can include forming a coating, e.g., thin film, on the current collector. Drying can be accomplished using conventional mechanisms such as drying in a vacuum oven.

The Chevrel-phase cathode material can be combined with an alkali-metal anode, e.g., a magnesium or magnesium alloy-containing anode, and an electrolyte to form an electrochemical cell, such as a magnesium ion rechargeable battery.

The electrolyte can be in the form of a solution. The electrolyte solution can include electrolyte salt containing magnesium and solvent.

In general, suitable electrolytes with high anodic/oxidative stability above 3V wherein magnesium can be deposited reversibly are not widely known and available in the art. It has been found that magnesium may not be reversibly deposited from solutions of simple magnesium salts, e.g., $Mg(ClO_4)_2$, in conventional organic solvents, e.g., acetonitrile, propylene carbonate or N, N-dimethylformamide. This is primarily due to the formation of a dense passivating surface/blocking layer on the reactive magnesium electrode surface by the reduction products. It is believed and well-known that bare magnesium metal reacts with anions such as ClO_4^-, BF_4^- to form insoluble magnesium salts/halides that block the magnesium electrodes. Moreover, the surface films effectively block the electrodes, as the mobility of the Mg^{2+} ions through the impervious passivating films is low. After a period of time, the capacity fades leading to failure of the electrochemical cell.

It is generally known that magnesium can be deposited using Grignard reagents in ethereal solvents. Magnesium can be electro-deposited reversibly primarily based on the solutions of tetrahydrofuran (THF) using Grignard reagents (R—MgX, R=alkyl; X=Br, CO, and amidomagnesium halides. However, due to the strongly reducing character of Grignard reagents, and limited oxidative stability (EtMgBr and BuMgCl have an oxidative stability 1.5V vs. Mg), it appears to be incompatible or realistically not possible for cathodes to be developed for use in batteries. Also, it is known to that tetrahydrofuran (THF) or primary amines (N-methylaniline) can be as electrolytes solvents in which both magnesium dissolution and deposition will occur. However, the Coulombic efficiency is typically low. In accordance with the invention, amidomagnesium halide-based Grignard reagent of the formula [3-[bis(trimethylsilyl) amino]phenylmagnesium chloride $[(CH_3)_3Si]_2NC_6H_4MgCl]$ solution in 1.0 M THF is a suitable salt for synthesis of magnesium battery electrolyte. Due to the presence of an aromatic ring coupled with an amino methylsilyl group with $MgCl^+$ ion, and electron lone pair donated to the aryl phenyl group, the R—Mg bond is thus strong and likely precludes or prevents the oxidation of the anionic species.

In certain embodiments of the invention, the electrolyte solution includes amidomagnesium-based magnesium salt transmetallated with an aluminum salt electrolyte dissolved in the solvent. In other embodiments, the electrolyte solution includes phenyl magnesium chloride-aluminum chloride, amidomagnesium-based magnesium salt transmetallated with an aluminum salt electrolyte, and solvent. The solvent can be tetrahydrofuran. In yet other embodiments, the electrolyte solution includes 3-bis(trimethylsilyl)aminophenyl-magnesium chloride with aluminum chloride in tetrahydrofuran.

The cathodes, electrodes and electrochemical cells prepared in accordance with the present invention demonstrate the desired benefits and advantages over those that are known in the art. For example, the electrochemical performance, e.g., rate capability and stable specific capacity with galvanostatic cycling, of the products prepared according to the invention are found to be superior to the known products. The Chevrel-phase material prepared in accordance with the present invention also exhibits very high rate capability and cycling performance when assembled in a rechargeable magnesium electrochemical battery cell.

EXAMPLES

Example I

Materials Preparation

$Cu_2Mo_6S_8$ (CuCP) was synthesized as follows. In a 3-neck round bottom flask, stoichiometric amounts of ammonium tetrathiomolybdate (4 g, 15.37 mmol; Alfa-Aesar 99.95%) and anhydrous copper(II) chloride (0.6890 g, 5.12 mmol, Alfa-Aesar 99.985%) were added to N,N dimethylformamide, DMF (130 ml) solution. The resultant mixture was heated over a hot plate (~90° C.) for 6 hours under constant N_2 bubbling. After complete reaction, the mixture turned deep red in color and was filtered. Tetrahydrofuran (1:5 by volume) was added immediately to the filtrate to incipient precipitation. A fine black precipitate was formed. This precipitate was kept overnight. Then, the precipitate was washed with tetrahydrofuran and methanol followed by drying at ~60° C. for 24 hours. The final dried solid product was ground and heated in a UHP Ar+6.5% H_2 atmosphere at ~1000° C. for 5 hours which directly yielded copper Chevrel phase $Cu_2Mo_6S_8$. The copper ions were leached out under an ambient atmosphere using a solution of 6 M HCl/O_2 bubbling for 8 hours according to the method outlined by Lancry, et al. ("Leaching Chemistry and the Performance of the Mo_6S_8 Cathodes in Rechargeable Mg Batteries, Chemistry of Materials", 16 (2004) 2832-2838). Following complete copper leaching, the solution was centrifuged, washed with the same solvent and dried in an oven at ~60° C. In order to perform qualitative phase analysis, Z-ray diffraction (XRD) was carried out using the Philips PW1830 system employing the CuK_α (λ=0.15406 nm) radiation. Microstructural analysis of the initial $Cu_2Mo_6S_8$

and Mo_6S_8 obtained after copper removal was then performed using a scanning electron microscopy (JSM-6610, JEOL) operating at 10 kV.

Electrochemical Characterization

An electrode slurry was prepared by mixing 80 wt. % of the Mo_6S_8 powder (−325 mesh), 10 wt. % Super P, 10 wt. % polyvinylidene fluoride (PVDF) dissolved into a solution of N-methylpyrrolidinone (NMP) to make a homogeneous solution. The slurry was coated onto a graphite foil and dried at ~110° C. in a vacuum oven. Electrochemical characterization was conducted at room temperature using fabricated electrodes assembled in 2016 coin cells that were in turn assembled inside an argon-filled MBraun Inc. glove box (<0.1 ppm each of O_2 and H_2O) employing magnesium foil as a counter electrode and cellgard separator soaked in an electrolyte solution of 0.4 molar 2(PhMgCl)—$AlCl_3$ in tetrahydrofuran. Cyclic voltammogram (CV) was performed using an electrochemical workstation (VersaSTAT 3, Princeton Applied Research) between 0.5-1.75 V at a constant sweep rate of ~0.01 mVs^{-1}. Galvanostatic charge-discharge cycles were carried out employing various current rates of 20-120 mA/g within 0.5-1.5 V, with a short rest period between the charge/discharge cycles using a multichannel battery testing system (Arbin BT2000 instrument).

Results

The XRD patterns of the heat-treated powder obtained by the precursor route shows characteristic XRD peaks. The major diffraction peaks were indexed to the rhombohedral phase of $Cu_2Mo_6S_8$ (space group: R-3; number: 148; JCPDS-ICDD: 00-047-1519). Similarly, the XRD pattern of the powder obtained after acid removal of copper ions matches with the rhombohedral Mo_6S_8 (space group: R-3; number: 148; JCPDS number: 00-027-0319). The exact match of the XRD patterns of pristine $Cu_2Mo_6S_8$ and acid leached Mo_6S_8 phase compared with the standard XRD pattern suggests that the precursor route is a simple and convenient approach to the direct synthesis of Chevrel phase compounds. An impurity phase of MoS_2 (space group: P63/mmc, number: 194, JCPDS number: 01-073 1508) was observed in both $Cu_2Mo_6S_8$ and Mo_6S_8 identified by the presence of peaks at $2\theta=14.4°$, 32.8°, and 39.6°. The SEM micrographs of the $Cu_2Mo_6S_8$ and Mo_6S_8 powder materials showed that distinct micrometer-size cuboidal shape crystallites (~0.5-2 μm) were formed. The crystallites were relatively smaller for the Mo_6S_8 as compared to the $Cu_2Mo_6S_8$ phase.

Cyclic voltammogram at a scan rate ~0.01 mVs^{-1} has been recorded between 0.5-1.75 V of the electrode (comprising 80% Mo_6S_8, 10% PVDF, 10% Super-P) in a 0.4 M THF/2(PhMgCl)—$AlCl_3$ electrolyte solution. The CV curve indicates a highly reversible behavior for magnesium-ion insertion/extraction in the Mo_6S_8 phase similar to the expected electrochemical phenomena based on observations in the art. The anodic and cathodic peaks observed at ~1.05 V and 1.17 V respectively, suggest Mg^{2+} insertion/extraction into the $Mg_xMo_6S_8$ ($0<x<2$) phase. It is established that Mg^{2+} insertion into the Mo_6S_8, Chevrel phase occurs in two stages, but due to partial charge entrapment after the initial magnesiation only 60-80% magnesium-ion can be extracted during the first charge, resulting in 20-25% capacity loss compared to the theoretical value (128 $mAhg^{-1}$). The loss in capacity may be salvaged if the electrochemical cell can be operated at an elevated temperature (~60-80° C.). The galvanostatic charge-discharge profiles (1^{st}, 2^{nd}, 25^{th} and 50^{th} cycle) of the Mo_6S_8 electrode performed at a constant current rate of ~20 mAg^{-1} (~C/6). During first discharge, electrochemical Mg^{2+} insertion occurred into Mo_6S_8 host, and offered a specific discharge capacity of ~116 $mAhg^{-1}$ (91% of theoretical value). During the 1^{st} discharge curve, Mg^{2+} insertion plateaus occurred at ~0.9 V, whereas Mg^{2+} extraction occurred at ~1.2 V. The 2^{nd}, 25^{th}, and 50^{th} cycles indicated only single reaction plateau at ~1.1 V (Mg^{2+} insertion) and at ~1.2 V (Mg^{2+} extraction), respectively. The cycling data suggested that the initial Mg^{2+} insertion into Mo_6S_8 was difficult and intrinsically very slow requiring a slight overvoltage of 200 mV compared to the subsequent cycles. The 1^{st} cycle discharge (~116 $mAhg^{-1}$) and charge capacity (~104 $mAhg^{-1}$) suggested ~91% magnesiation and ~81% demagnesiation occurred from the Mo_6S_8 host (resulting in a 1^{st} cycle irreversible loss 10.3%). Complete removal of Mg^{2+} ion was not possible at room temperature due to the partial charge trapping in the Mo_6S_8 host. The variation of specific capacity vs. cycle number along with coulombic efficiency of the Mo_6S_8 electrode, cycled at a constant current of ~20 mAg^{-1} (~C/6 rate) in the potential window of 0.5-1.5 V shows that the 1^{st} cycle discharge and charge capacity of the Mo_6S_8 electrode is ~116 $mAhg^{-1}$ and 104 $mAhg^{-1}$, respectively, with a 1^{st} cycle irreversible loss (FIR) of ~10.3%. However, from the 2^{nd} to the 50^{th} cycle, it is shown that there was a steady charge and discharge capacity of ~80 $mAhg^{-1}$ and ~76 $mAhg^{-1}$ respectively, which resulted in an improved coulombic efficiency of ~95%. This excellent capacity retention may be ascribed to the formation of high surface area cuboidal shaped ~0.5-2 μm, Mo_6S_8 particles, which allowed suitable wetting of the active material with the electrolyte promoting good charge transfer. The differential capacity plot (dQ/dV vs. V) of the 1^{st}, 2^{nd}, 25^{th}, 50^{th} cycle shows that during the 1^{st} discharge and charge cycles, magnesiation/demagnesiation occurred at ~0.92 V and at ~1.17 V, respectively. A sharp peak is shown at ~1.10 V (magnesiation) and at ~1.17 V (demagnesiation) for the 2^{nd}, 25^{th}, and 50^{th} cycles which was due to the known phenomena of partial entrapment of Mg^{2+} ion after the 1^{st} magnesiation ($Mg_2Mo_6S_8$) reaction which resulted in only one Mg^{2+} ion cycling into/from the $Mg_xMo_6S_8$ ($0<x\leq1$) host from the 2^{nd} cycle and thereon. The differential capacity plot matched well with the charge-discharge profile of the electrode cycled at 20 mAg^{-1} which suggested excellent cyclability and reversibility of Mg^{2+} insertion/extraction phenomena of the as-synthesized Mo_6S_8 electrode in an Mg cell.

The excellent electrochemical rate performance was validated. The Mg/Mo_6S_8 cell was cycled at various current rates. The results showed the rate capability of the Mo_6S_8 electrode performed at current rates of 20 mAg^{-1} (~C/6), 64 mAg^{-1} (~C/2), 128 mAg^{-1} (~C), and 192 mAg^{-1} (~1.5 C). The capacity retention of the synthesized cuboidal Mo_6S_8 via the novel precursor approach was excellent compared to literature reports of similar Chevrel phase compounds synthesized by published approaches. The discharge capacities at the above current rate was ~76 $mAhg^{-1}$, ~72 $mAhg^{-1}$, ~68 $mAhg^{-1}$, and ~66 $mAhg^{-1}$ respectively. The coulombic efficiency at ~/6, ~/2, ~1 C, and ~1.5 C rate was 95%, 97.8%, 98.9%, and 99.3%, respectively. Although it is expected that coulombic efficiency decreases with increasing C-rate, the unique features of cuboidal Mo_6S_8 (excellent electronic conductivity) rendered it suitable for fast insertion/extraction of Mg^{2+} ions at ambient temperature with an improved coulombic efficiency in a Mg prototype cell.

Conclusions

In summary, unique cuboidal shape ~0.5-2 μm size $Cu_2Mo_6S_8/Mo_6S_8$ Chevrel phase was synthesized by a rapid and facile precursor route. XRD confirmed the phase formation and the electrochemical measurements indicated superior performance, such as rate capability and stable

specific capacity. The Mo_6S_8 Chevrel phase exhibited extremely high rate capability and cycle performance when assembled in an Mg cell. The cell delivered a capacity of ~66 $mAhg^{-1}$ at ~1.5 C rate making it suitable as a cathode for a magnesium-ion battery.

Example II

Stoichiometric amounts of MoS_2, Mo, and CuS were batched in a SS vial (powder:ball ratio=1:10). The powders were mechanically milled for intervals of 1 hour, 2 hours and 3 hours, and subjected to XRD patterns. After 3 hours of milling, the powder was heat-treated at 1000° C./5 hours under UHP argon atmosphere. The X-ray diffraction patterns showed the synthesis of $Cu_2Mo_6S_8$ Chevrel-phase by the high energy mechanical milling route. The XRD patterns of the heat-treated powder also showed the formation of pure crystalline $Cu_2Mo_6S_8$. The $Cu_2Mo_6S_8$ was washed with HCL/O_2 bubbling for 7 hours to yield completely crystalline Mo_6S_8.

Example III

Stoichiometric amounts of $MoSe_2$, Mo, and CuSe were batched in a SS vial (powder:ball ratio=1:10). The powders were mechanically milled for intervals of 1 hour, 2 hours and 3 hours, and subjected to XRD patterns. After 3 hours of milling, the powder was heat-treated at 1000° C./5 hours under UHP argon atmosphere. The XRD analysis and patterns collected showed the synthesis of $Cu_2Mo_6Se_8$ Chevrel-phase by the high energy mechanical milling route. Further, the XRD patterns of the heat-treated powder showed the formation of pure crystalline $Cu_2Mo_6Se_8$. The $Cu_2Mo_6Se_8$ was washed with HCL/O_2 bubbling for 7 hours to yield completely crystalline Mo_6Se_8.

Example IV

Novel amidomagnesium-based electrolytes at varying molar ratios were compared with Aurbach's 1^{st} and 2^{nd} generation electrolytes by conducting cyclic voltammetry. The electrochemical parameters obtained from the cyclic voltammograms conducted at a 25 mvs^{-1} scan rate using amidomagnesium-based novel electrolytes at different molar ratios are compared with Aurbach's 1^{st} generation electrolyte (i.e., 0.25 molar $Mg(AlCl_2EtBu)_2$/THF) and 2^{nd} generation electrolyte (i.e., 0.4 molarPhMgCl)—$AlCl_3$/THF) are shown in Table 1.

TABLE 1

Electrochemical parameters obtained from the cyclic voltammograms conducted at 25 mVs^{-1} scan rate using novel amidomagnesium based electrolytes at different molar ratio and compared with Aurbach's 1^{st} and 2^{nd} generation electrolyte.

base/acid ratio	Onset deposition potential (V)	Anodic stripping peak potential (V)	Mg cycling efficiency (%)
1:1	−0.283	0.983	93.2
2:1	−0.242	0.842	63.7
3:1	−0.351	0.401	56.5
1:2 (1^{st} generation)	−0.193	1.032	95
2:1 (2^{nd} generation)	−0.37	0.643	85.5

The 1:1 (Lewis base: Lewis acid ratio) electrolyte conducted at a scan rate of 25 mVs^{-1} demonstrated enhanced performance for all of the novel electrolytes in accordance with the invention. Further, Table 1 suggests that the coulombic efficiency for reversible magnesium deposition/dissolution was near or about 93% for the 1:1 electrolyte. The coulombic efficiency for the 2:1 and 3:1 electrolytes was about 64% and about 56%, respectively.

The linear sweep voltammograms obtained at a scan rate of 1 mVs^{-1} from open circuit potential to approximately 4 V showing the anodic stability onto Pt working electrode of the novel amidomagnesium-based electrolytes at varying molar ratios as compared with Aurbach's 1^{st} and 2^{nd} generation electrolyte. The linear sweep voltammograms of the above-mentioned electrolytes from open circuit potential to about 4 V at 1 mVs^{-1} showed that the electrochemical stability of the amidomagnesium-based novel electrolytes of 1:1, 2:1 and 3:1 was about 2.27, about 2.33 and about 2.19 V, respectively, onto noble metal (e.g., platinum electrode). The electrochemical stability of the novel electrolyte was similar to Aurbach's 1^{st} generation electrolyte but significantly lower than Aurbach's 2^{nd} generation electrolyte.

Example V

A Mo_6S_8 cathode was tested in a 2016 coin cell using 0.4 M 3((3-bis(trimethylsilyl)amino)phenylmagnesium chloride)-$AlCl_3$THF (3:1 novel electrolyte). The electrochemical performance in particular when conducted at a current rate of 20 mAg^{-1} and cyclic voltammetry employing a scan rate of 100 microvolts per second (100 μVs^{-1}) showed a 1^{st} cycle irreversible loss of about 40% and stable discharge capacity about 37 $mAhg^{-1}$ at C/6 rate with coulombic efficiency about 90%.

Example VI

A Mo_6S_8 cathode was tested in a 2016 coin cell using 0.4 M 2((3-bis(trimethylsilyl)amino)phenylmagnesium chloride)-$AlCl_3$THF (2:1 novel electrolyte). The electrochemical performance in particular when conducted at a constant current of 20 mAg^{-1} and a scan rate of 100 microvolts per second (100 μVs^{-1}) showed a 1^{st} cycle irreversible loss of about 48% and stable discharge capacity about 54 $mAhg^{-1}$ at C/6 rate with coulombic efficiency about 88%.

Example VII

A Mo_6S_8 cathode was tested in a 2016 coin cell using 0.4 M ((3-bis(trimethylsilyl)amino)phenylmagnesium chloride)-$AlCl_3$THF (1:1 novel electrolyte). The electrochemical performance in particular when cycled at a constant current of 20 mAg^{-1} and a scan rate of 100 microvolts per second (100 μVs^{-1}) showed a 1^{st} cycle irreversible loss of about 26% and stable discharge capacity about 60 $mAhg^{-1}$ at C/6 rate with coulombic efficiency about 99%.

Example VIII

$Cu_2Mo_6S_8$ (Cu_2CP) Chevrel phase was developed by High Energy Mechanical Milling (HEMM) route. Stoichiometric amounts of MoS_2, Mo, and CuS were batched in a SS vial (powder:ball ratio=1:10). The powders were mechanically milled for 1 hour, 2 hour, and 3 hour intervals and subjected to XRD analysis to collect the XRD patterns. After 3 hours of high-energy mechanical milling (HEMM), the powder was heat-treated at 1000° C./5 h under UHP Ar atmosphere. XRD pattern of the heat-treated powder collected showed the formation of pure crystalline $Cu_2Mo_6S_8$.

Further, $Cu_2Mo_6S_8$ was washed with HCl/O_2 bubbling for 7 hours yields to obtain completely crystalline Mo_6S_8 (CP).

It was established that Mg^{2+} insertion into Mo_6S_8 Chevrel phase occurred in two stages, and theoretically could offer a capacity ~128 $mAhg^{-1}$. However, due to partial charge entrapment after initial magnesiation, only 50-60% magnesium-ion could be extracted during first charge, resulting in 40-50% irreversible loss in the 1^{st} cycle from the theoretical value (~128 $mAhg^{-1}$). In order to minimize the 1^{st} cycle irreversible loss, Cu was partially leached from the original Cu_2CP structure. 1.8 g of Cu_2CP was added in 20 ml 6M HCl solution in a small glass vial with a magnetic stir bar. Cu_2CP/HCl solution was continuously stirred for 2 days at room temperature. After 2 days of continuous stirring, the solution was ultrasonically cleaned using distilled water (3 times) and dried at a temperature of 60° C. for 24 hours. XRD pattern of the partial leached Cu_2CP collected showed the formation of completely crystalline partially de-cuprated, $CuMo_6S_8$ (Cu_1CP).

Results

The XRD patterns were collected on $Cu_2Mo_6S_8$ (Cu_2CP) powder obtained by high energy mechanical milling of CuS, MoS_2 and Mo stoichiometric compositions followed by heat treatment at 1000° C./5 h under UHP Ar, and acid leached $CuMo_6S_8$ (CuCP) obtained after 2 days partial leaching of copper using 6M HCl solution. The Bragg diffraction lines were indexed to a hexagonal-rhombohedral symmetry unit cell of $Cu_2Mo_6S_8$ (space group: R-3; number: 148; JCPDS-ICDD: 00-047-1519). Lattice parameter(s) calculated using least-square method of the experimental data (a=0.96478 nm, c=1.02026 nm, and unit cell volume=822.42×10^{-3} nm^3) was in good agreement with the standard $Cu_2Mo_6S_8$ unit cell parameters (a=0.9584 nm, c=1.025 nm, unit cell volume=815.36×10^{-3} nm^3). Similarly, the XRD pattern obtained after removal of one copper from the heat-treated powder using hydrochloric acid treatment matched with the JCPDS patterns. The Braggs lines were indexed with the hexagonal-rhombohedral symmetry unit cell of $CuMo_6S_8$ phase (space group: R-3; number: 148; JCPDS-ICDD: 00-034-1379), and the calculated lattice parameter(s) (a=0.94412 nm, c=1.04761 nm, and unit cell volume=808.70×10^{-3} nm^3) matched quite well with standard unit cell parameters of $CuMo_6S_8$ obtained from above ICDD database (a=0.94120 nm, c=1.04070 nm, unit cell volume=798.40×10^{-3} nm^3). The calculated lattice parameters values were consistent with the standard lattice parameter(s) values of pristine $Cu_2Mo_6S_8$ and acid leached $CuMo_6S_8$ powder obtained from JCPDS-ICDD database suggested that 6M HCl treatment for 2 days leached 50% copper from the original Cu_2CP structure and yielded $CuMo_6S_8$ (CuCP).

The variation of specific capacity versus cycle number along with coulombic efficiency of the $CuMo_6S_8$ electrode, cycled at a constant current of ~20 mAg^{-1} (~C/6 rate) in the potential window of 0.5-1.5 V using 0.4 molar 2(PhMgCl—$AlCl_3$)/tetrahydrofuran electrolyte showed that the 1^{st} cycle discharge and charge capacity of the $CuMo_6S_8$ electrode was ~105 $mAhg^{-1}$ and ~78 $mAhg^{-1}$, respectively, with a 1^{st} cycle irreversible loss (FIR) of ~25.7% (or coulombic efficiency of ~74.3%). It is to be noted that, the 1^{st} cycle irreversible loss (FIR) of Mo_6S_8 is ~50% obtained by completely leaching out copper from the HEMM derived Cu_2CP structures. Further, from 10^{th} cycles onward there was a steady charge-discharge capacity of ~55 $mAhg^{-1}$, with a coulombic efficiency of ~99.9%. The preliminary results of CuCP suggested that partial Mg^{2+} charge entrapment which is common during 1^{st} cycle magnesiation (discharge) in Mo_6S_8 cathode may be overcome with $CuMo_6S_8$ structure where one Mg^{2+} can cycle without any hindrance.

The HEMM derived Mo_6Se_8 cathode assembled in a 2016 coin cell using Mg metal anode, 0.4 molar 2(PhMgCl)—$AlCl_3$/tetrahydrofuran electrolyte exhibited a ~17% capacity fade after 100 cycles. The exact reason of fading is still under investigation. However, in order to improve the electrical conductivity of the Mo_6Se_8 cathode, it was mixed with conductive graphite and coated with Mg^{2+} conducting $MgSO_4$ and used as composite cathode.

Example IX

The $Cu_2Mo_6Se_8$ (~Cu_2CP) Chevrel phase developed by 3 hours of High Energy Mechanical Milling (HEMM) of stoichiometric amounts of $MoSe_2$, Mo, and CuSe was followed by heat-treatment at 1000° C./5 h under UHP Ar atm, were further mixed with commercial available synthetic graphite (SigmaAldrich, 1-2 m) in situ during milling process at 70:30 ratio (weight percent) and used as composite cathode for magnesium battery. Further, $Cu_2Mo_6Se_8$/graphite was washed with HCl/O_2 for 7 hours to develop Mo_6Se_8/graphite composite cathode.

Example X

Mo_6Se_8 Chevrel-phase obtained after the complete removal of copper from HEMM derived $Cu_2Mo_6Se_8$ was mixed thoroughly with previously prepared water solution of commercially available $MgSO_4$ (Aldrich, 99.9%) at 70:30 ratio (weight percent). Further the mixed slurry was dried at 60° C. for 24 hours and used as $MgSO_4$ coated Mo_6Se_8 cathode for magnesium battery.

Example XI

Electrochemical impedance spectroscopy (EIS) was carried out on a Mo_6S_8 electrode before and after cycling to evaluate Mg^{2+}-ion charge storage mechanisms. EIS was performed using a Versastat 3 (Princeton Applied Research Inc.) potentiostat over a frequency range of 0.01 Hz-100 KHz. An A.C. amplitude of 5 mV was used and the spectra were obtained before cycling and subsequent to 1^{st} and 2^{nd} discharge cycle. Electrode potential was stabilized after discharge cycle and EIS was performed (i.e., immediately such that no significant relaxation processes and equilibrium phase changes occurred) to observe any noticeable changes in the charge storage mechanism upon cycling. The effect of cycling on charge transfer parameters was also analyzed by performing EIS. Z-View (Scribner Associates, Inc.; version 3.3) software was used for Randall's equivalent circuit modeling of the experimentally collected impedance spectra.

Results

Electrochemical impedance study (EIS) was performed on a newly prepared Mo_6S_8 electrode (wet chemical route) as well as cycled Mo_6S_8 electrode at the magnesiated (discharged) and de-magnesiated (charged) states assembled in a 2016 coin cell using magnesium foil as the counter and reference electrodes, Mo_6S_8 composite electrode as the working electrode and 0.4 molar 2(PhMgCl)—$AlCl_3$ in tetrahydrofuran as the electrolyte. A Nyquist plot was generated for the electrode prepared using the Chevrel phase (Mo_6S_8) at different stages. A clear transition in behavior was observed upon cycling. The impedance behavior was modeled using a Randall's circuit which considered a number of electrochemical phenomena including:

a) High frequency series resistance (R_s);

b) High frequency semi-circle (HFS) due to sluggish charge and electron transfer kinetics (CPE_e and R_e);

c) Gerischer impedance as a result of the coupling of a chemical and an electrochemical process (GE);

a barrier to solid state diffusion of Mg^{2+}. Without intending to be bound by any particular theory, this mass transfer limitation and loss in magnesium trapped irreversibly as a result of the phase change occurring in the 1^{st} discharge cycle, was believed to be the reason for the low capacity occurring from the 2^{nd} cycle onward.

TABLE 2

Charge transfer parameter(s) of the Chevrel phase electrode at different stages obtained from Randall circuit model.

	R_s	CPE_e-T	CPE_e-P	R_e	CPE_i-T	CPE_i-P	R_i	GE-T	GE-P	W_o-R	W_o-T	W_o-P	R_{trap}	CPE_{trap}-T	CPE_{trap}-P
Before cycling	10.27	8.03E−06	0.974	286.4	8.49E−06	1.009	53.28	0.693	0.134	5.041	4.22E−06	0.393	2.32E−04	1.318E−04	0.125
After 1^{st} discharge	12.36	4.88E−06	0.941	182.6	7.23E−05	0.821	9748	5.195	0.089	0.205	1.61E−07	0.416	3.01E−05	1.287E−04	0.294
After 2^{nd} discharge	12.94	4.29E−05	0.76	921.2	1.14E−05	0.881	65.09	3.849	0.728	0.135	1.08E−07	0.375	8855	5.813E−04	0.479

d) Low frequency semi-circle (LFS) due to Mg-ion trapping in the Chevrel phase (Mo_6S_8) host (CPE_i and R_i); and

e) Diffusion characteristic and associated ion-trapping (W_o, R_{trap}, CPE_{trap}).

A model including all of these elements can be used for circuit modeling. The model employed considered both charge transfer and mass transfer phenomena contributing to the electrode impedance. The circuit also included constant phase elements (CPEs) due to the porous nature of the electrodes. In addition, it was found that the Gerischer impedance element (GE) was very small and insignificant for the electrode.

With respect to the effect of insertion/extraction on the impedance profile of the electrode materials, it was observed that the material exhibited a significant increase in overall impedance following the initial Mg^{2+}-ion insertion after the 1^{st} discharge cycle. Table 2 depicts the values of resistances obtained as a result of Randall's circuit modeling. The solution resistance (R_s) was almost invariable. The charge transfer resistance (R_e) which is a characteristic of electron and ion transfer differed, pre- and post-Mg^{2+}-ion insertion stage. There was a drop in R_e post Pt discharge and an increase from subsequent to 2^{nd} discharge. Interfacial resistance increased post Pt discharge and decreased subsequent to 2^{nd} discharge. Charge trapping (R_{trap}) which remained very small before cycling and post Pt discharge, increased by almost 8 orders, post 2^{nd} discharge. The transition in these three parameters provided information with respect to the Mg^{2+} charge storage mechanisms occurring in the Chevrel phase. The significant increase in overall impedance subsequent to first discharge indicated that the Mg^{2+}-ion insertion was accompanied by a rate limiting phenomenon. This, in turn, was seen by the two order rise in interfacial resistance (R_i) subsequent to 1^{st} discharge. The electrode resistance, however, maintained the same order indicating that post-insertion in the 1^{st} discharge cycle, the electrode became kinetically limiting for electrochemical charge transfer processes as a result of the formation of either a secondary interface or a phase change. After the 2^{nd} discharge, however, the R_i was small but R_{trap} and R_e increased indicating that part of the layer was either inactive or became

Example XII

The electrochemical behavior and stability of amidomagnesium-based three non-aqueous electrolyte 0.4 molar $[(CH_3)_3Si]_2NC_6H_4MgCl]$—$AlCl_3$/THF were investigated using both a three-electrode electrochemical cell and coin cells. The cyclic voltammetry, linear sweep voltammetry, and coin cell charge/discharge measurements indicated that the electrolyte is capable of reversibly cycling magnesium with a Coulombic efficiency ~90% and electrochemical stability ~2.3V. Reversible cycling of magnesium from the amidomagnesium-based electrolytes were proved by scanning electron microscopy (SEM), and energy-dispersive X-ray spectroscopy (EDX) analyses. SEM and EDX show that uniform spherical magnesium particles (1-5 μm) free from any dendrites formation deposited on platinum substrate. Moreover, Mo_6S_8 cathode derived by molten salt and high energy mechanical milling route able to deliver a first cycle discharge capacity ~120-128 $mAhg^{-1}$ demonstrate the feasibility of the system as potential 2V magnesium battery electrolyte.

1 molar $[(CH_3)_3Si]_2NC_6H_4MgCl]$ salt in THF solution was transmetallated with 1 molar $AlCl_3$/THF in-house solution at three different Lewis base-acid molar ratio of 1:1, 2:1 and 3:1 and studied the electrochemical behavior using cyclic voltammetry, chronopotentiometry, linear sweep voltammetry, and galvanostatic charge-discharge cycles. Electrochemical data shows that amiodomagnesium-based electrolyte is electrochemically stable up to 2.3V and capable of delivering 100% theoretical capacity (~128 $mAhg^{-1}$) from Mo_6S_8 Chevrel phase cathode at room temperature.

EXPERIMENTAL SECTION

Synthesis of 0.4 Molar L^{-1} $[(CH_3)_3Si]_2NC_6H_4MgCl]$—$AlCl_3$/THF Electrolyte

The starting chemical of [(CH3)3Si]2NC6H4MgCl] (1 molar in tetrahydrofuran) was purchased from Sigma Aldrich and used without further purification. Highly pure inhibitor-free anhydrous tetrahydrofuran (THF) was obtained from EMD Millipore and further dried (using Na chips and benzophenone) under ultra high purity Argon atmosphere using stringent drying steps outlined in the

literature. Anhydrous $AlCl_3$ (99.999%) powder in glass ampoules was obtained from Sigma Aldrich and used as-received. First, 1 molar $AlCl_3$/THF was prepared where ~2 g $AlCl_3$ was gradually added in an anhydrous THF (~15 ml) through a powder addition funnel inside a Schlenk flask under constant stirring. The above reaction is exothermic and a light yellowish solution was obtained after the reaction was over. The electrolyte of chemical formula 0.4 molar L^{-1} $[(CH_3)_3Si]_2NC_6H_4MgCl]$—$AlCl_3$/THF at different molar ratio was synthesized according to the following method. Stoichiometric amounts of $[(CH_3)_3Si]_2NC_6H_4MgCl]$ (1 molar in THF) and $AlCl_3$ (1 molar in THF) (1:1, 2:1, and 3:1 Lewis base/Lewis acid ratio in volume) were added in a 25 ml clear glass vial. The mixture was continuously stirred for ~2 h inside the glass vial closed with a screw threaded cap. After 2 h reaction, the screw cap was carefully opened and the electrolyte solution was diluted using anhydrous tetrahydrofuran (THF), resulting in the formation of 0.4 molar L^{-1} $[(CH_3)_3Si]_2NC_6H_4MgCl]$—$AlCl_3$/THF electrolyte. The electrolyte preparation was carried out inside an MBraun Inc. glove box where the oxygen and moisture levels are always maintained <0.1 ppm. 0.25 molar $L^{-1}Mg(AlCl_2EtBu)_2$/THF (butyl-ethyl complex or BEC) as well as 0.4 molar L^{-1}2 (PhMgCl)—$AlCl_3$/THF (all-phenyl complex or APC) were also synthesized as reference electrolytes according to the standard protocol outlined in literature.

Characterization

Electrochemical analyses, including linear sweep voltammetry (LSV) and cyclic voltammetry (CV) were carried out on a CHI660D electrochemical station. The electrochemical cell used in the LSV and CV study was a three electrode cell which consisted of a working electrode (Pt), counter electrode (Mg), and reference electrode (Mg). The scan speed of the test was set to 10, 25, and 50 mV/s within −1V to +2.2V potential ranges. Deposition/dissolution efficiency of Mg on to Pt electrode was carried out in 2016 coin cells at a constant current density of 0.25 $mAcm^{-2}$ for 1 hour deposition and −0.25 $mAcm^{-2}$ for 1 hour dissolution for chronopotentiometic measurements. The three electrode cells were assembled with the Pt working electrode, woven fiberglass (GFD separator), Mg counter and reference electrode, and 0.4 M L^{-1} $[(CH_3)_3Si]_2NC_6H_4MgCl]$—$AlCl_3$/THF electrolyte.

Scanning electron microscopy (SEM) and energy-dispersive X-ray spectroscopy (EDX) were performed using a Philips XL-30 operating at an accelerating voltage of 20 kV. It is noted that the electrodes were washed by copious amount of THY three times and dried in vacuum before SEM and EDX analysis. The conductivity of the synthesized electrolyte was measured by a portable conductivity meter (HI991301, HANNA).

Results and Discussions

Amidomagnesium halide-based Grignard reagent of the formula [3-[bis(trimethylsilyl)amino]phenylmagnesium chloride $[(CH_3)_3Si]_2NC_6H_4MgCl]$ solution in 1.0 THF was identified as a potential salt for the synthesis of ma magnesium battery electrolyte. The chronopotentiogram of the 1^{st} cycle plating and stripping on platinum substrate using 1 mol L^{-1} $[(CH_3)_3Si]_2NC_6H_4MgCl]$/THF solutions demonstrated the expected reversibility of Mg^{2+}. Metallic magnesium was reversibly plated onto platinum and stripped versus Mg^{2+}/Mg couple in a three electrode cell at a constant current rate of ~0.1 mA/cm^2 for 1 h. It was observed that the overpotential for magnesium plating (−0.123V versus Mg^{2+}/Mg) and stripping (0.103V versus Mg/Mg^{2+}) was low and Coulombic efficiency ~75% was observed suggest that the $[(CH_3)_3Si]_2NC_6H_4MgCl]$/THY Grignard reagent based solvent is capable of cycling Mg-ion in a reversible manner. Cyclic voltammetry study of this amiodomagnesium-based solvent using platinum as working electrode and magnesium being counter and reference electrode in a three electrode cell further prove our hypothesis. The cell was first run from open circuit potential to −1V (for Mg deposition) followed by −1V to 2.2V (for Mg stripping) using different voltage scan rate. The cyclic voltammogram at different scan rates (10, 25 and 50 mV/s) between −1 to 2.2 V showed the obvious reversible magnesium deposition/dissolution which occurred within the potential window of ~2.2V. The onset potential for 1^{st} cycle Mg deposition was −0.192V, −0.243V and −0.293V for 10 mVs^{-1}, 25 mVs^{-1} and 50 mVs^{-1} scan rate respectively (see Table 1). The increase in onset potential with increasing voltage scan rate is due to solution resistance and increasing kinetic barriers with high charge transfer rate that exist in any standard electrochemical cell. A typical charge balance during cathodic plating and anodic stripping of the 1 mol L^{-1} $[(CH_3)_3Si]_2NC_6H_4MgCl]$/THF solutions showed ~65% cyclic efficiency. Table 1 shows the onset deposition potential and the magnesium cyclic efficiency of the 1 mol L^{-1} $[(CH_3)_3Si]_2NC_6H_4MgCl]$/THF solutions at different scan rate. It appears that the 1 mol L^{-1} $[(CH_3)_3Si]_2NC_6H_4MgCl]$/THF Grignard reagent has some potential benefits like the electrochemical stability window ~1.5V but the Coulombic efficiency is very low (~65%). However, preliminary electrochemical data suggest that $[(CH_3)_3Si]_2NC_6H_4MgCl]$/THF is a Grignard reagent based Lewis base is a promising system which can be transmetallated with a strong Lewis acid ($AlCl_3$, BF_3 etc.) in order to improve its electrochemical performance as Aurbach et al. mentioned in literature. This prompted our interest to synthesize amidomagnesium-based electrolyte by transmetallation of the amidomagnesium chloride $[(CH_3)_3Si]_2NC_6H_4MgCl]$ with a strong Lewis acid ($AlCl_3$) at different base/acid ratio and further dissolving the reaction product in tetrahydrofuran at different molar level and study their electrochemical performance.

Three different electrolytes were synthesized at three different base/acid ratio (we will call it 1:1, 2:1, and 3:1 electrolyte) as listed in Table 3.

TABLE 3

Electrochemical parameters of amidomagnesium based electrolyte compared with BEC and APC electrolyte including the anodic stability of the electrolytes on Pt working electrode.

base/acid ratio	Onset deposition potential (V)	Anodic stripping peak potential (V)	Mg cycling efficiency (%)	Anodic stability limit in Pt (1 > 100 μAcm^{-2})
1:1	−0.283	0.983	93.2	2.27
2:1	−0.242	0.842	63.7	2.33
3:1	−0.351	0.401	56.5	2.19

TABLE 3-continued

Electrochemical parameters of amidomagnesium based electrolyte compared with BEC and APC electrolyte including the anodic stability of the electrolytes on Pt working electrode.

base/acid ratio	Onset deposition potential (V)	Anodic stripping peak potential (V)	Mg cycling efficiency (%)	Anodic stability limit in Pt ($1 > 100\ \mu Acm^{-2}$)
1:2 (BEC electrolyte)	−0.193	1.032	95	2.2(known)
2:1 (APC Electrolyte	−0.37	0.643	85.5	3.0(known)

In order to validate the quality of the amidomagnesium-based three different electrolytes, it was first evaluated by cyclic voltammetry (CV) study using a three-electrode cell. The first five cycles of CV within the potential window −1 V to 2.2V performed using platinum working electrode, magnesium counter and reference electrode in 0.4M L^{-1} $[(CH_3)_3Si]_2NC_6H_4MgCl]$—$AlCl_3$/THF electrolyte family demonstrated that deposition and dissolution of magnesium in the present system is highly reversible with a 1^{st} cycle deposition-dissolution efficiency of ~93% for 1:1 electrolyte (Table 1). On the contrary, 1^{st} cycle magnesium deposition-dissolution efficiency was ~63% and ~56% for 2:1 and 3:1 electrolytes, respectively. From the 2^{nd}-5^{th} cycles magnesium deposition/dissolution efficiency increased to ~77% and ~85% for 2:1 and 3:1 electrolytes, respectively. The cycling efficiency for magnesium deposition-dissolution was calculated from total charge balance during reduction/oxidation for each half-cycle as described in an earlier publication. The overpotential for the deposition was observed to be −0.23V and remain steady from the 1^{st} to 5^{th} cycles for 1:1 electrolyte. In the case of 2:1 and 3:1 electrolytes, overpotential for the deposition was −0.24V and −0.35V respectively. The decrease in overpotential and the increasing deposition-dissolution efficiency of magnesium from the 2^{nd} cycle onwards may be ascribed to the desorption of electrolyte on the working electrode. Importantly, a cyclic voltammetry study showed a minimum 5-fold increase in total current density for magnesium deposition and dissolution which suggest that transmetallation of amidomagnesium-based Grignard reagent with $AlCl_3$ increases number of active ionic-species in the electrolytes for Mg-ion transport.

The magnesium deposition and dissolution reactions on platinum substrate could be repeated hundreds of times for 1:1, 2:1, and 3:1 electrolytes as confirmed for 0.4 molar $[(CH_3)_3Si]_2NC_6H_4MgCl]$—$AlCl_3$/THF (1:1) electrolyte solution. The first three cycles for magnesium deposition-dissolution obtained from 1:1, 2:1 and 3:1 electrolytes at a given current rate of ~0.25 $mAcm^{-2}$ for 15 minutes (0.225 Ccm^{-2}), respectively, showed that the overpotential for 1^{st} cycle deposition drops drastically to a lower voltage from open circuit potential, however, the voltage steadied after 10-15 seconds. For 1:1, 2:1, and 3:1 electrolyte, the overpotential for the deposition were −0.15V, −0.06V and −0.07V for the first three cycles and dissolution were 0.1V, 0.05V, and 0.04V respectively. Low overpotential for magnesium deposition-dissolution observed from the chronopotentiogram suggested that the magnesium-ion transport was amenable in the above electrolytes. Galvanostatic cycling for the first 100 cycle magnesium deposition-dissolution on the platinum substrate gave a reoxidation cycling efficiency of ~89% and ~83%, respectively, for 1:1 and 2:1 electrolytes. The reoxidation cycling efficiency of 3:1 was found to fluctuate between ~60-80% for the first 50 cycles and then steadily increased to ~88%. In all the three cases, the reoxidation cycling efficiency was found to increase steadily from the 1^{st} to 20^{th} cycle may be due to desorption of electrolyte and electroactive species on the working electrode. In order to confirm the deposit structure, magnesium was electrodeposited on a platinum substrate from the three different amidomagnesium-based electrolytes at 0.5 $mAcm^{-2}$ for 1 hour (1.8 Ccm^{-2}). SEM image analysis of the platinum substrate after 1 hour deposition from 2:1 electrolyte reflected the presence of pronounced spherical particles of 1-5 μm on the surface. An EDX full frame analysis of the SEM image confirmed that the spherical particles were magnesium. The uniform spherical magnesium deposition morphology is extremely important for practical use of the electrolytes because it ensures the lack of dendrite formation in battery systems.

The electrochemical performance of the three amidomagnesium-based electrolytes at varying molar ratios was compared with BEC and APC electrolytes. The electrochemical parameters obtained from the cyclic voltammograms conducted at a 25 mVs^{-1} scan rate are shown in Tables 1 and 2 including the cyclic voltammograms of the amidomagnesium-based electrolytes with a direct comparison with BEC (i.e., 0.25 molar $Mg(AlCl_2EtBu)_2$/THF) and APC (i.e., 0.4 molar 2(PhMgCl)—$AlCl_3$/THF) electrolyte. The 1:1 (Lewis base:Lewis acid ratio) amidomagnesium-based electrolyte demonstrated enhanced performance among all the amidomagnesium-based electrolytes synthesized. It showed a 1^{st} cycle Coulombic efficiency ~93% and was in excellent agreement with chronopotentiometic measurements. Table 2 lists the electrochemical parameter(s) obtained from the linear sweep voltammograms (LSV) performed at a scan rate of 1 mVs^{-1} from open circuit potential to approximately 4V showing the anodic oxidative stability of the amidomagnesium-based electrolytes onto platinum working electrode compared with known anodic stability of ~2.2V and ~3V for BEC and APC electrolytes, respectively. It was found that the electrochemical stability of the amidomagnesium-based novel electrolytes was ~2.27V, ~2.33V and ~2.19V for 1:1, 2:1 and 3:1 electrolytes, respectively. The electrochemical anodic stability of the amidomagnesium-based electrolyte was similar to Aurbach's BEC electrolyte but significantly lower than APC electrolyte.

In order to validate the feasibility of the amidomagnesium-based electrolyte solutions for a magnesium battery system, Mo_6S_8 Chevrel phase a known magnesium-ion intercalation cathode was synthesized by molten salt (MS) route found in literature and high energy mechanical milling (HEMM) route first time reported. The 2016-type coin cell was constructed using the 0.4M L^{-1} $[(CH_3)_3Si]_2NC_6H_4MgCl]$—$AlCl_3$/THF solution as the electrolyte (3:1 molar ratio), a Mg disc as a negative electrode, and Mo_6S_8

as a positive electrode. The 2016 coin cells were cycled at a current rate of ~C/6 (~20 mAg^{-1}) with the discharge and charge voltage limits of 0.5V and 1.5V versus Mg reference electrode at room temperature. The results showed that the 1^{st} cycle discharge and charge capacity was ~128 $mAhg^{-1}$ (100% of theoretical capacity) and ~70 $mAhg^{-1}$ with 1^{st} cycle Coulombic efficiency ~54.8% for HEMM derived Mo_6S_8 cathode. The expected drop in 1^{st} cycle capacity was due to partial charge trapping which occurred in the Mo_6S_8 electrode during 1^{st} cycle. Nevertheless, Mo_6S_8 electrode derived by MS and HEMM method was able to cycle magnesium reversibly and yield a discharge capacity of ~66 $mAhg^{-1}$ and ~60 $mAhg^{-1}$ calculated based on the weight of the cathode's active mass with Coulombic efficiency ~97% and ~95% respectively, between 2^{nd} and 50^{th} cycle. Typical cyclic voltammogram conducted between 0.5-1.5V at a scan rate of 0.1 mVs^{-1} shows cathodic and anodic peak at ~1.0V and ~1.3V due to formation of $Mg_xMo_6S_8$ ($0<x\leq1$) phase.

Conclusions

In summary, we have synthesized a ~2.3V amidomagnesium based magnesium electrolyte system based on the Lewis base-acid complex via a reaction between organometallic Grignard reagent $[(CH_3)_3Si]_2NC_6H_4MgCl]$ and $AlCl_3$ in tetrahydrofuran solvent. The $[(CH_3)_3Si]_2NC_6H_4MgCl]$ $AlCl_3$/THE electrolyte solution shows excellent reversibility of Mg deposition-dissolution (~90% cycling efficiency for reversible magnesium deposition), and electrochemical anodic stability (2.3V vs. Mg reference electrode). In addition, the good compatibility of the amiodomagnesium-based electrolyte solution with the Mo_6S_8 intercalation cathode derived by the molten salt as well as the high energy mechanical milling routes confirms that the electrolyte could be practically used in 2V rechargeable Mg battery systems.

Example XIII

High energy mechanical milling (HEMM) of a stoichiometric mixture of molybdenum and copper chalcogenide (CuT and CuT_2), followed by a short thermal treatment at elevated temperature was applied to synthesize Chevrel phases ($Cu_2Mo_6Z_8$; Z=S, Se), a cathode precursor for magnesium battery. Differential scanning calorimetry, thermogravimetric analyses, combined with X-rays diffraction and scanning electron microscopy was used to evaluate the phase transformation(s) during milling and thermal treatment. It was shown that CuS and Mo reacted at elevated temperature and formed an intermediate ternary Chevrel phase which further reacted with residual Mo and MoS_2 to form the desired $Cu_2Mo_6S_8$. Quantitative XRD analyses showed the formation of ~96-98% Chevrel phase as low as 30 minutes time during post milling thermal treatment process. Electrochemical performance of de-cuprated Mo_6S_8 and Mo_6Se_8 phase were evaluated by cyclic voltammetry (CV), galvanostatic cycling, electrochemical impedance spectroscopy (EIS). CV and galvanostatic cycling data of Mo_6S_8 and Mo_6Se_8 electrodes showed expected anodic/cathodic behavior and a stable capacity after the 1^{st} cycle with the formation of $Mg_xMo_6Z_8$ (Z=S, Se; $x=1\leq x\leq2$). EIS at ~0.1 V intervals of Mo_6S_8 electrode during 1^{st} and 2^{nd} cycle showed that partial Mg-ion trapping caused increased charge transfer resistance, R_e. Carbon incorporation during milling resulted in improved capacity fade in the case of Mo_6Se_8 electrode and ~99.93% Coulombic efficiency was achieved. Importantly, ease of fabrication, stable capacity, high Coulombic efficiency and excellent rate retention rendered HEMM-derived Chevrel phases as suitable magnesium battery cathodes for stationary electrical energy storage (EES) applications.

Electrochemical performance of HEMM-derived Mo_6S_8 and Mo_6Se_8 phase devoid of copper was evaluated in 2016 coin cell by cyclic voltammetry, and galvanostatic cycling at various C— rates. The Chevrel phase(s) exhibited competitive electrochemical results and provided a time saving, rapid approach.

Materials Synthesis

$Cu_xMo_6S_8$ was synthesized as follows using an HEMM approach in accordance with certain embodiments of the invention. Stoichiometric amounts of MoS_2 (1 g, 99% Alfa Aesar), Mo (0.6 g, 99.9% Alfa Aesar), and CuS (0.4 g, 99.8% Alfa Aesar) were batched in a stainless steel vial (powder:ball ratio=1:10). The powders were mechanically milled in atmospheric condition for 30 minutes, 1 hour, 2 hours, and 3 hours in a SPEX-8000M shaker mill and subjected to XRD analysis. $Cu_xMo_6Se_8$ was also synthesized using a similar approach. Stoichiometric amounts of $MoSe_2$ (1.141 g, 99.9% Alfa Aesar), Mo (0.432 g, 99.9% Alfa Aesar), and CuSe (0.427 g, 99.5% Alfa Aesar) were batched in a stainless steel vial (powder:ball ratio=1:10). The powders were mechanically milled for 30 minutes, 1 hour, 2 hours, and 3 hours, and subjected to XRD analysis. The milled powder was thermal treated at elevated temperature under ultra-high purity Argon (UHP-Ar) atmosphere. Copper-ions were subsequently leached out from HEMM-derived ternary Chevrel phase(s) using 6 molar hydrochloric acid solution under constant oxygen flow for 8 hours in ambient atmosphere. After copper-ions were leached completely from the parent phase, the acid solution containing the residue was centrifuged, washed with de-ionized water three times and dried in an oven at ~323K.

Materials Characterization

The thermal behavior of the milled powder was evaluated by thermo-gravimetric (TG)/differential scanning calorimetry (DSC) using a Netzsch STA 409 PC Luxx thermal analyzer unit in an ultra UHP-Ar atmosphere at a heating rate of 10 K/min, up to 1273K. The milled powder samples were isothermally heat treated at 1273K for 30 minutes under UHP-Ar atmosphere followed by X-rays diffraction (XRD) analyses. In addition, the mechanically milled powder was thermal treated at elevated temperature for different durations (30 minutes, 5 hours) under UHP-Ar atmosphere. Powder X-ray diffraction (XRD) of the milled, commercial and thermally-treated powders was carried out using the Philips PW1830 system employing the CuK_α (λ=0.15406 nm) radiation. Quantitative phase analysis was carried out using PANalytical X'Pert HighScore Plus Rietveld program on the powder XRD patterns. No other attempt was made to determine the composition obtained from the HEMM approach at high temperature. Microstructural analyses of the milled, commercial and heat treated powders (Chevrel phases) were performed using a scanning electron microscopy (JSM-6610, JEOL) operating at 10 kV and high resolution transmission electron microscopy-HRTEM (JEOL JEM 2000FX) operating at 200 kV. Specific surface area of the milled powder was measured using the Brunauer-Emmett-Teller (BET) technique. Each sample was vacuum degassed and then tested using a Micromeritics ASAP 2020 BET equipment.

Electrochemical Characterization

Electrode slurry was formulated by mixing 80 wt. % of active material (−325 mesh), 10 wt. % Super-P carbon, 10 wt. % polyvinylidene fluoride (PVDF) binder with N-methylpyrrolidinone (NMP) solvent together in a glass vial with

constant magnetic stirring for 24 hours. The slurry obtained was coated (50 μm thick) onto graphite foil acting as a current collector and dried at ~383K overnight in a vacuum oven. Further, the dried electrodes were uniaxially pressed at ~5 MPa to improve the particle contacts and then circular disks (Θ=11.28 mm) were punched with an active material loading ~1-3 mg/cm^2. An electrochemical test was carried out at room temperature with 2016-type coin cells assembled inside an argon-filled MBraun Inc. glove box (<0.1 ppm each of O_2 and H_2O) employing magnesium foil as the counter and reference electrode, electrode disks as working electrode, and Celgard® separator soaked in an electrolyte solution of 0.4 molar 2(PhMgCl)—$AlCl_3$/tetrahydrofuran. Cyclic voltammogram (CV) was acquired using an electrochemical workstation (VersaSTAT 3, Princeton Applied Research) at a constant sweep rate of ~0.001 Vs^{-1}. Galvanostatic charge-discharge cycles were carried out at various rates ~20-160 mAg^{-1} within 0.5-1.5V or 0.5-1.7V, employing a short rest period between the charge/discharge cycles using a multichannel battery testing system (Arbin BT2000 instrument). Electrochemical impedance spectroscopy (EIS) was performed to understand the charge storage behavior in Chevrel phases. EIS was performed on the Versastat 3 over a frequency range of 0.01 Hz-100 KHz. An A.C. amplitude of 5 mV was used and the spectra were obtained after charge/discharge cycles. The charge transfer characteristics and accompanying parameters were analyzed by equivalent circuit modeling using Z-View (Scribner Associates, Inc.; version 3.3).

Results and Discussion

Synthesis of $Cu_xMo_6S_8$ Chevrel Phase by HEMM Approach

Each as-received commercial powder as well as mechanically milled powders was subjected to XRD analysis. The major XRD peaks from commercial powders can be indexed with standard Mo (ICDD number: 98-006-2711; cubic; space group Im-3m, number 229), CuS (ICDD number: 01-079-2321; hexagonal; space group P63/mmc, number 194), and MoS_2 (ICDD number: 03-065-7025; hexagonal; space group P63/mmc, number 194) phase. From the XRD pattern of mechanically milled powders, it appeared that gradual increase in milling duration from 30 minutes to 3 hours induced a homogeneous mixture between CuS, Mo, MoS_2 phase. The Bragg reflection of high intensity peaks from MoS_2, Mo and CuS were evident in the XRD patterns of milled powders. The absence of any peaks besides CuS, Mo and MoS_2 suggested that mechanical milling only induced an intimate mixture between the constituent phases rather than forming any new phase(s). However, gradual increase in milling duration would likely induce an X-rays amorphization of the MoS_2 and CuS phase either due to formation of ultrafine particles or diffusive mixing mechanisms initiated between the CuS and MoS_2 phases which would significantly decrease the peak intensity and allow peak broadening. The relative intensity of peaks from (002), (010), (013), (105) and (112) planes of MoS_2 and (102), (013), (006), (110) planes of CuS were significantly reduced and peaks were broadened as the milling duration increased from 30 minutes to 3 hours. The Bragg reflection from (011), (002), (112), and (022) planes reflected from elemental Mo were found to be relatively intense. The difference in peak intensities and broadening during milling operation was mainly due to a difference in the hardness of starting compositions, where ductile and hard Mo metal powder repeatedly got fractured and cold welded whereas brittle and soft MoS_2, and CuS ceramic phase got fragmented and embedded within the ductile Mo matrix during milling operation.

SEM images of the commercial powder used during milling showed unique morphology of the particles before milling. CuS particles were of irregular shape and agglomerated, whereas MoS_2 were large and flaky, and Mo particles were round and globular. Following 30 minutes of mechanical milling, the morphology of the particles changed completely and irregular shape particles were formed. SEM image of the 30 minute-milled powder showed formation of agglomerated irregular shaped particles mechanically bonded together. Quantitative elemental composition of the milled powder obtained by EDX analyses confirmed that measured atomic percent of each element (Cu, Mo, and S) was close to the stoichiometric batch composition. The elemental X-ray mapping of Cu, Mo, and S atoms in the milled powder showed homogeneous distribution of Cu, Mo, and S within the agglomerated particles without segregation on any specific site. Importantly, the absence of any oxides of copper and molybdenum up to 3 hours of milling was evident from the XRD patterns which suggested that milling between CuS, MoS_2, and Mo in atmospheric conditions does not oxidize or contaminate the milled composition. However, mechanical milling did not form the desired ternary CP (since Chevrel phase formation is a thermally activated metastable process and requires thermal treatment at elevated temperature under inert atmosphere to form the desired phase). The Brunauer-Emmett-Teller (BET) surface area measurement by nitrogen adsorption/desorption technique of the milled powder was ~12.33 m^2/g, 14.61 m^2/g, 7.72 m^2/g, and 9.65 m^2/g, for 30 minute-, 1 hour-, 2 hours-, and 3 hours-milled powder sample, respectively. From the surface area measurement it appeared that mechanical milling beyond 1 hour had no effect on reduction of surface area of milled particles. However, to complete the formation of homogeneous mixture between the constituents the mechanical milling was continued up to 3 hours.

To assess phase formation during thermal treatment of the mechanically milled powder, selected milled samples were subjected to thermo gravimetric-differential scanning calorimetry (TG-DSC) under UHP-Ar atmosphere up to 1273K at a constant heating rate of 10K/min. The TG-DSC trace showed a continuous exothermic behavior of the milled powder samples. The 30 minutes-milled sample showed a broad exothermic peak between 600-1260K associated with an enthalpy of formation ~775 J/g (~743 kJmol^{-1}) approximated to the calculated enthalpy of formation (~873 kJmol-1) for $Cu_2Mo_6S_8$ at 1000K. DSC traces of 1 hour- and 3 hour-milled powder samples showed a continuous exothermic behavior beyond 600K with no apparent exotherms up to 1273K. However, thermo gravimetric (TG) curves exhibited ~4% weight loss between ~525K to ~630K for each sample. The 4% weight loss associated with TG analysis was accompanied by heat evolution in the DSC curves which suggested that an exothermic process was initiated. To assess the exothermic reaction processes evolved with DSC scan of milled powder sample, each of the constituents (CuS, Mo and MoS_2 powder) used during milling was subjected to TG-DSC under identical conditions. The thermo gravimetric trace of Mo and MoS_2 commercial powder showed no appreciable weight change. However, CuS showed ~16% weight loss when heated to ~745K that was accompanied by an endothermic reaction (enthalpy of formation: ~206 J/g or 19.7 kJ/mol) between ~686K to ~773K with the peak endotherm at ~745K. Without intending to be bound by any particular theory, it is believed that

the endothermic peak was due to formation of Cu_2S and sulfur-rich liquid phase from CuS since the thermodynamic measurement of enthalpy of formation for peritectic decomposition of CuS to Cu_2S and S-rich liquid was ~17.87 kJ/mol. The formation of Cu_2S from CuS resulted in a 16% weight difference according to the following formula: —2CuS (2×95.61)=Cu_2S (159.16)+S (32.06). The ~4% weight loss (¼th of ~16%) observed was related to the phase transformation of CuS to Cu_2S and sulfur-rich liquid phase and was in agreement with the following formula: −2CuS+3Mo+3MoS_2=$Cu_2Mo_6S_8$. It is believed that the sulfur-rich liquid reacted immediately with elemental Mo and formed the MoS_2 phase which subsequently reacted with Cu_2S, unreacted Mo and MoS_2 and formed the desired ternary copper CP according to the following formula —Cu_2S+3MoS_2+xMoS_2+(3-x)Mo+(1-2x)S=$Cu_2Mo_6S_8$.

To assess the details of phase formation during thermal treatment, equimolar amounts of Mo (~1 g) and CuS(~1 g) were mechanically milled for 30 minutes and subjected to TG-DSC. The TG-DSC trace of CuS—Mo powder exhibited three regions, a small endothermic hump at ~714K (due to peritectic reaction and melting of CuS to Cu_2S and S) associated with ~8% weight loss, a plateau between the temperature interval of 714K-800K, and a continuous exothermic region beyond 800K up to 1273K. It appeared that the peritectic reaction at ~714K occurred slightly earlier than expected likely due to mechanical milling having decreased the particle size and collapsed the hexagonal crystal structure of CuS. The XRD pattern of the mechanically milled powder showed the presence of Mo and CuS phase. XRD analysis was performed on the remnant powder after the TG-DSC test was completed. The XRD showed the formation of $Cu_{1.83}Mo_3S_4$ phase (ICDD: 98-000-5103), along with elemental Mo and Cu. It is believed that CuS dissociated into Cu_2S and elemental sulfur and further reacted with Mo to form the $Cu_{1.83}Mo_3S_4$ Chevrel phase according to the following reactions:

$$CuS=Cu_2S+Mo(\sim 714 \text{ to } \sim 745K)$$

$$2Cu_2S+2S+4Mo=Cu_{1.83}Mo_3S_4+2.17\ Cu+Mo(\text{between } 800K\text{-}1273K).$$

Thermal treatment of CuS+Mo powder was carried out inside a tube furnace at two different temperatures of ~773K (above the peritectic temperature of CuS) and ~1273K at a heating rate of 10K/min and allowed the powder to furnace cool under UHP-Ar atmosphere. The XRD pattern of the sample thermally treated to ~773K showed the presence of Cu_2S and elemental Mo, whereas, the sample heated to ~1273K showed the formation of $Cu_{1.83}Mo_3S_4$, Cu and Mo peaks. Similar study between equimolar Mo (0.75 g) and MoS_2 (1.25 g) showed the small endotherm ~711K associated with ~8% weight loss due to the peritectic reaction melting of CuS in the TG-DSC trace. However, the CuS+MoS_2 milled powder when heated to ~773K and ~1273K respectively, showed no traces of Chevrel phase formation confirmed by XRD analyses, instead Cu_2S and MoS_2 phase were intact. The above evaluations suggested that the presence of CuS and Mo in the starting composition was essential for the formation of ternary copper CP. One possible reaction scheme for the formation of $Cu_2Mo_6S_8$ ternary CP at elevated temperature may be $Cu_{1.83}Mo_3S_4$+2.17Cu+Mo+2Mo+6MoS_2=2$Cu_2Mo_6S_8$.

To assess whether ternary CP can be formed during thermal treatment, a XRD analysis of the remnant powder was conducted following completion of the TG-DSC on 2CuS+3Mo+3MoS_2 samples milled for 30 minutes and 1 hour. The alumina crucible used during the TG-DSC test was carefully opened upon cooling to room temperature and the sample (~10 mg) was evenly spread onto a glass slide and a XRD analysis between 10-90° 20 value was performed. Unexpectedly, the XRD data of a 1 hour milled sample heated to 1273K at a constant heating rate of ~10K/min showed the formation of $Cu_2Mo_6S_8$ phase along with unreacted MoS_2, Mo, and MoO_2 phase as impurities. It is believed that $Cu_2Mo_6S_8$ was formed before the temperature was reached to 1273K. However, incomplete formation/transformation of $Cu_2Mo_6S_8$ phase was mainly due to insufficient time to allow completion of the solid state diffusive reaction to occur between the constituents. A similar TG-DSC evaluation was repeated up to 1273K with an additional 30 minute-holding time at 1273K with 1 hour- and 3 hour-milled powders. The XRD analysis performed on 1 hour- and 3 hour-mechanically milled powder following TG-DSC test showed the formation of $Cu_2Mo_6S_8$ phase with minor unreacted MoS_2 and Mo. According to the Cu—Mo—S ternary phase diagram at 1273K, $Cu_xMo_6S_8$ phase could co-exist with MoS_2 and metallic Mo and appear as minor impurities during high temperature synthesis of the ternary Chevrel phase, $M_xMo_6S_8$ (M=Cu, Sn). The above results were encouraging and indicated that ternary copper CP ($Cu_2Mo_6S_8$) could be formed using CuS, Mo, and MoS_2 powder at 30 minute-dwell time at 1273K peak temperature. The magnified portion between 20 values of 12-16° of the XRD data clearly showed that 30 minute-dwell time at 1273K had a pronounced effect on $Cu_2Mo_6S_8$ formation, as the high intensity peak from (002) plane of MoS_2 was significantly reduced at the expense of peak intensity from (101) plane of $Cu_2Mo_6S_8$ phase. An ~2 g powder sample of 30 minute- and 1 hour-milled powder was placed on a corundum crucible and thermally treated inside a tubular furnace with a heating rate of 10K/min at two different temperatures of 1123K and 1273K with a 30 minute-dwell time at peak temperature followed by cooling to room temperature at a constant cooling rate of 10K/min (the above experiments were done under UHP-Ar, gas flow rate ~100 standard cubic centimeter/min). The heat-treated powder analyzed by XRD showed the formation of ternary copper CP—$Cu_2Mo_6S_8$. The 30 minute-mechanically milled powder sample thermally treated to 1123K with 30 minute-dwell time showed the formation of $Cu_2Mo_6S_8$ with slight presence of unreacted MoS_2 and Mo powder. However, the 30 minute- and 1 hour-milled powder samples when heated to 1273K with 30 minute-dwell time at the peak temperature, the MoS_2 peak was completely vanished and fully crystalline $Cu_2Mo_6S_8$ phase was formed. The magnified portion between 12-16° of the XRD patterns depicted the high intensity peak from (101) plane of $Cu_2Mo_6S_8$ phase matched completely with the standard $Cu_2Mo_6S_8$ database (ICDD number: 00-047-1519). Secondary electron SEM image of the $Cu_2Mo_6S_8$ phase synthesized at 1123K and 1273K with 30 minute-dwell time at peak temperature showed the formation of sub-micron to micrometer size irregular shaped particles. The composition, obtained by EDX quantitative analyses, of the copper Chevrel phase formed at 1123K and 1273K, respectively, was in good agreement with TG-DSC/XRD data and suggested that rapid synthesis of $Cu_2Mo_6S_8$ by HEMM was possible and could be achieved in a time period as low as at 30 minutes. Lattice parameter(s) calculated using the least-square method of the experimental XRD data was in good agreement with the standard $Cu_2Mo_6S_8$ (ICDD number: 00-047-1519; a=0.9584 nm, c=1.025 nm, unit cell volume=815.36×10^3 nm^3) unit cell parameters and presented in Table 1.

Phase Formation and Electrochemical Activity of HEMM Derived De-Cuprated Mo_6S_8

To obtain the de-cuprated Mo_6S_8 phase, $Cu_2Mo_6S_8$ phase formed at 1123K and 1273K was treated with 6 molar hydrochloric acid solution with constant O_2 bubble for 7 hours in a round bottom flask. In order to confirm the formation of Mo_6S_8 after complete copper leaching, XRD analysis was performed. All the Braggs peaks in the XRD patterns matched with the standard Mo_6S_8 (ICDD: 98-005-708) pattern which suggested complete copper removal was achieved. EDX full frame analyses also confirmed that hydrochloric acid-treated samples were devoid of copper. High resolution SEM image of the respective Mo_6S_8 phase showed agglomerated particles of submicron to micrometer size. Electrochemical performance of the 80 wt. % Mo_6S_8: 10 wt. % Super-P: 10 wt. % PVDF composite electrode was evaluated in a 2016 coin cell. The galvanostatic cycling conducted at ambient condition between 0.5-1.7V with a current of 20 mAg^{-1} (~C/6 rate) showed 1^{st} cycle discharge capacity of ~101 $mAhg^{-1}$ and ~100 $mAhg^{-1}$ for de-cuprated Cu_2CP formed at ~1123K and ~1273K, respectively. A steady and expected discharge capacity of ~68 mAg^{-1} and ~70 $mAhg^{-1}$ was achieved from 2^{nd} to 100^{th} cycle due to partial Mg-ion trapping within Mo_6S_8 structure and associated 30% drop in capacity in the 1st cycle. The cyclic voltammogram of the Mo_6S_8 electrode showed expected signature of two anodic peaks during magnesiation and a cathodic peak during de-magnesiation, respectively.

To achieve the fully crystalline phase pure $Cu_2Mo_6S_8$ ternary CP, dwell time at peak temperature of ~1273K was increased to 5 hours. The XRD pattern of 3 hour-mechanically milled powder heat treated at 1273K with the holding time of 5 hours at peak temperature confirmed the complete formation of $Cu_2Mo_6S_8$. De-cuprated Mo_6S_8 was obtained after complete copper removal using a 6 molar HCl solution with constant oxygen bubbling for 7 hours. The lattice parameter(s) calculated using least-square method of $Cu_2Mo_6S_8$ phase formed after 3 hour-mechanically milled powder thermally treated at ~1273K with 5 hours dwell time at peak temperature are shown in Table 4 and are in good agreement with standard unit cell parameter(s).

TABLE 4

Calculated lattice parameter(s) of $Cu_xMo_6S_8$ phase.

Condition	Lattice parameter(s) of $Cu_2Mo_6S_8$	Quantitative Phase formation (%)
1 h mechanically milled powder thermally treated to 1273Kwith 30 min hold at 1273K	a_H: 0.963138 nm, c_H: 1.021042 nm a_R: 0.651957 nm, α_R: 95.233° unit cell volume = 820.2588 × 10^{-3} nm^3	0.3% Mo + 99.7% $Cu_2Mo_6S_8$
30 min mechanically milled powder thermally treated to 1273Kwith 30 min hold at 1273K	a_H: 0.962119 nm, c_H: 1.021095 nm a_R: 0.651464 nm, α_R: 95.1953° unit cell volume = 818.567 × 10^{-3} nm^3	0.3% Mo + 99.7% $Cu_2Mo_6S_8$
30 min mechanically milled powder thermally treated to 1123Kwith 30 min hold at 1123K	a_H: 0.959014 nm, c_H: 1.022991 nm a_R: 0.650268 nm, α_R: 95.0207° unit cell volume = 814.8032 × 10^{-3} nm^3	1.4% MoS_2 + 0.3% Mo + 98.3% $Cu_2Mo_6S_8$
3 h mechanically milled powder thermally treated to 1273Kwith	a_H: 0.961938 nm, c_H: 1.021293 nm a_R: 0.65141 nm, α_R: 95.1822°	100% $Cu_2Mo_6S_8$

TABLE 4-continued

Calculated lattice parameter(s) of $Cu_xMo_6S_8$ phase.

Condition	Lattice parameter(s) of $Cu_2Mo_6S_8$	Quantitative Phase formation (%)
5 h hold at 1273K	unit cell volume = 818.4188 × 10^{-3} nm^3	

Whereas, lattice parameter(s) of de-cuprated Mo_6S_8 calculated using the least-square method (a=0.919233 nm, c=1.087942 nm, unit cell volume=796.1371×10^{-3} nm^3) were found to be in excellent agreement with the standard Mo_6S_8 (ICDD number: 98-005-1708; a=0.92 nm, c=1.088 nm, unit cell volume=797.51×10^{-3} m^3) unit cell parameters showed that complete removal of copper was achieved. The SEM image of $Cu_2Mo_6S_8$ and de-cuprated Mo_6S_8 showed irregular shape submicron size particles that were formed in the case of $Cu_2Mo_6S_8$ phase, which retained their morphology in the de-cuprated Mo_6S_8 phase as well. The HRTEM lattice fringe spacing of $Cu_2Mo_6S_8$ and Mo_6S_8 phase was calculated as ~0.645 nm and ~0.479 nm which corresponded to the interplanar d-spacing of (101) and (102) planes for $Cu_2Mo_6S_8$ and ~0.641 nm for Mo_6S_8 corresponding to the interplanar d-spacing of (101) plane (hexagonal crystal system: space group R-3). The de-cuprated Mo_6S_8 phase was then tested as a magnesium battery cathode in a 2016 coin cell setup using 2(PhMgCl)—$AlCl_3$/tetrahydrofuran electrolyte and polished Mg foil as the anode. The electrochemical performance of Mo_6S_8 composite electrode showed outstanding performance where Mg-ions could be inserted/extracted reversibly from the de-cuprated Mo_6S_8 phase. The cyclic voltammogram acquired at a sweep rate of 0.1 mVs^{-1} between 0.5-1.75V versus Mg/Mg^{2+} showed typical reversible magnesiation/demagnesiation phenomena of Mo_6S_8 electrode where magnesiation and demagnesiation occurred at ~1V and ~1.28V, respectively. The galvanostatic cycling of Mo_6S_8 electrode showed 1^{st} cycle discharge (magnesiation) and charge (demagnesiation) capacity of ~92 $mAhg^{-1}$ (~72% of theoretical capacity 128 $mAhg^{-1}$) and ~57 $mAhg^{-1}$ with Coulombic efficiency ~62% when cycled at a current density of 20 mAg^{-1}. Between the 2^{nd} and 107^{th} cycle a stable discharge and charge capacity of ~62 mAg^{-1} and 67 mAg^{-1} was observed with 95.6% Coulombic efficiency. The expected drop in capacity from 2^{nd} cycle onwards was due to one Mg-ion being trapped which occurred within the Mo_6S_8 framework at the 1^{st} cycle resulting in a capacity loss from the theoretical value (~128 $mAhg^{-1}$). Capacity versus voltage profile of 25^{th}, 50^{th}, and 100^{th} cycle exhibited magnesiation and demagnesiation reaction plateaus at ~1.07V and ~1.2V and was in agreement with a CV curve and those reported in the literature. Rate retention of Mo_6S_8 electrode was also excellent, at C/24, C/12, C/6, C/4, C/3, C/2, 1 C (1 C~120 mAg^{-1}) and 1.5 C current rate a discharge capacity of ~79 $mAhg^{-1}$, ~74 $mAhg^{-1}$, ~70 mAg^{-1}, ~65 $mAhg^{-1}$, ~62 $mAhg^{-1}$, ~59 $mAhg^{-1}$, ~56 $mAhg^{-1}$, ~51 $mAhg^{-1}$ and ~49 $mAhg^{-1}$ was achieved with a Coulombic efficiency ~96.8%, ~94.2%, ~97.1%, ~99.2%, ~99.9%, ~99.9%, ~99.7%, ~99.9%, and ~99.2%, respectively. In addition, long cycle stability of Mo_6S_8 electrode was tested in a 2016 coin cell setup and showed remarkable performance and durability. The 2016 coin cell was cycled continuously for 48 days and was able to deliver a specific capacity ~70 $mAhg^{-1}$ with a Coulombic efficiency ~99% at 330^{th} cycle. These attributes support the

HEMM approach for rapid synthesis of $Cu_2Mo_6S_8$ Chevrel phase, and as an alternative synthesis route for ternary CP.

Synthesis of $Cu_xMo_6Se_8$ Chevrel Phase by HEMM Approach

It was demonstrated that $Cu_2Mo_6S_8$ could be synthesized by HEMM approach and its electrochemical performance in a magnesium battery was deemed competitive with electrochemical data for Chevrel phases made by known synthesis methods. This similar HEMM approach was employed for the synthesis of ternary Chevrel phase —$Cu_2Mo_6Se_8$ using CuSe, Mo, and $MoSe_2$ as starting powders. XRD analyses showed powder XRD patterns collected of 30 minutes, 1 hour, 2 hours, and 3 hours of mechanically milled powder of $2CuSe+3MoSe_2+3Mo$ nominal composition. The XRD patterns from the commercial powders were also acquired and compared. The major XRD peaks of commercial powders were indexed with Mo, $MoSe_2$ (ICDD number: 03-065-7025; hexagonal; space group P63/mmc, number 194), and CuSe (ICDD number: 98-007-1382; hexagonal; space group P63/mmc, number 194) phase along with minor Cu_3Se_2 (ICDD number: 98-000-6312) as impurities. A gradual increase in milling duration from 30 minutes to 3 hours likely induced a homogeneous and intricate mechanical mixture obtained between CuSe, Mo, $MoSe_2$ phases. The XRD patterns showed the Bragg reflections of high intensity peaks from $MoSe_2$, Mo are present but the CuSe peaks completely vanished after 2 hours of milling. Importantly, the absence of oxides of copper and molybdenum during milling operation indicated that mechanical milling between CuSe, $MoSe_2$, and Mo phase was also conducive for the direct synthesis of the Cu_2Mo_6Se phase. SEM images of the CuSe, and $MoSe_2$ commercial powder used during milling showed unique morphologies of the particles before milling. CuSe particles were plate-like, whereas $MoSe_2$ particles were large and flaky. However, upon 30 minutes of milling the morphology of the particles changed completely and correspondingly irregular shaped particles were formed. SEM image of the 30 minutes milled powder showed the formation of agglomerated irregular shape particles. EDX full frame analysis confirmed that the stoichiometry of the batch composition was maintained. Elemental X-ray mapping analysis confirmed that the distribution of Cu, Mo, and Se atoms in the milled powder were homogeneous throughout the microstructure. However, it is to be noted that direct mechanical milling did not form the desired ternary CP and thermal treatment at elevated temperature under inert atmosphere was required. The BET surface area of the 30 minutes, 1 hour, 2 hours, and 3 hours milled powder was ~5.82 m^2/g, ~3.87 m^2/g, ~2.09 m^2/g, and ~2.29 m^2/g, respectively. The BET surface area measurement showed that 30 minutes of milling generated fine particles and further milling had no pronounced effect on the particle size. However, the milling duration was continued up to 3 hours to complete the formation of a homogeneous intricate mixture of the different reaction constituents.

The thermal behavior of the 30 minutes, 1 hour, 2 hours and 3 hours mechanically milled powder was evaluated by thermo gravimetric-differential scanning calorimetry (TG-DSC). The samples were heated under UHP-Ar atmosphere up to ~1273K at a constant heating rate of 10K/min. DSC trace of 30 minutes sample showed a continuous exothermic behavior up to ~624K followed by a plateau up to ~745K. The thermo gravimetric (TG) curve exhibited a ~7% weight loss within the above temperature range. However, there was no further weight loss beyond ~624K and a continuous exothermic behavior was observed up to ~1273K. To assess the exothermic/endothermic behavior evolved with TG-DSC scan of milled powder sample, each constituent used during milling was subjected to TG-DSC under identical conditions. The TG-DSC trace of commercial CuSe, Mo, and $MoSe_2$ powder from room temperature to ~1273K showed no appreciable weight change of $MoSe_2$ commercial powder. However, CuSe showed ~23% weight loss between 646K-860K reflected in the TG curve, that was accompanied by two endothermic reaction peaks at ~658.8K (enthalpy: 68.45 J/g or 9.75 kJ/mol) and at ~798K (enthalpy: 10.83 J/g or 1.54 kJ/mol) in the DSC trace. The endothermic peak observed at ~658.8K was due to incongruent melting of CuSe and formation of Cu_2Se and Se-rich liquid and the second endothermic peak observed at ~798K was due to eutectic melting of Cu_2Se and sulfur-rich phase according to the copper-selenium binary phase diagram. Previous studies showed that enthalpy of formation for peritectic decomposition of CuSe to Cu_2Se and Se-rich liquid was ~11.8±0.03 kJ/mol and was in agreement with experimental data. The formation of Cu_2Se and Se-rich liquid from CuSe at ~658.8K observed in the DSC curve resulted in a 27.7% weight loss according to the following formula: $-2CuSe\ (2\times142.51)=Cu_2Se\ (206.05)+Se\ (78.96)$. Thus, the ~7% weight loss (¼th of ~27.7%) was related to the phase transformation of CuSe to Cu_2Se phase and was in excellent agreement with the following formula: $-2CuSe+3Mo+3MoSe_2=Cu_2Mo_6Se$. It was believed that Se-rich liquid reacted immediately with Mo powder and formed the $MoSe_2$ phase and further, the remaining constituents (Cu_2Se, Mo and $MoSe_2$) reacted with each other and formed the desired $Cu_2Mo_6Se_8$ phase.

$$Cu_2Se+3MoSe_2+xMoSe_2+(3-x)Mo+(1-2x)Se=Cu_2Mo_6Se_8$$

The thermal treatment of milled powder at elevated temperature was important to initiate liquid-phase sintering between the constituents. To assess the phase formation during heat treatment, ~2 g of 1 hour mechanically milled powder sample of nominal composition $2CuSe+3Mo+3MoSe_2$ was heated inside a tube furnace with a heating rate of 10K/min at various temperatures followed by cooling to room temperature at a constant cooling rate of 10K/min (these experiments were done under UHP-Ar atmosphere with gas flow rate ~100 standard cubic centimeter/min). The XRD pattern of the sample heated to ~733K could be indexed to Mo, $MoSe_2$, Cu_2Se and MoO_2 phases. The presence of (11-1) MoO_2 peaks at 26.0° 2θ value was likely as a result of the oxidation of Mo to MoO_2 during thermal treatment due to the unavoidable presence of trace amount of oxygen inside the furnace. In addition, Cu_2Se phase [presence of (111) peak at 26.7° 2θ value] was evident instead of CuSe in the XRD pattern due to incongruent melting of CuSe to Cu_2Se and Se-rich liquid at ~659K according to the TG-DSC analysis. However, there was no Bragg's reflection observed from elemental Se in the XRD pattern which suggested that Se-rich liquid immediately reacted with Mo and formed the $MoSe_2$ phase. This is supported by the TG-DSC analysis of 1 hour milled powder as an exothermic peak is observed at ~735K due to formation of $MoSe_2$ phase. $MoSe_2$ could be formed at temperatures as low as ~650K and is stable over wide temperature range between ~273K to ~1473K according to the Mo—Se binary phase diagram. The XRD patterns of the sample heated to ~925K and ~1000K showed similar XRD peaks with the sample heated to ~733K which corroborated that higher temperature beyond ~1000K is required for $Cu_xMo_6Se_8$ phase to be formed. The powder sample when heated to ~1089K showed the formation of $Cu_2Mo_6Se_8$

phase with the presence of elemental Mo, $MoSe_2$, and MoO_2 as impurities. The absence of high intensity peak from (111) plane of Cu_2Se phase at 26.7° 2θ value in the XRD pattern except for the ~733K sample suggested that Cu_2Se started to disappear above 800K due to eutectic melting of Cu_2Se phase which likely reacted with Mo and $MoSe_2$ phase and nucleated the desired ternary selenium CP phase analogous to the case observed with sulfur CP (shown above). As expected, the sample when heated to ~1151K also showed the formation of $Cu_2Mo_6Se_8$ phase. However, phase-pure $Cu_xMo_6Se_8$ was not detected in the XRD patterns when the sample was heated to ~1089K or ~1151K due to insufficient dwell time at the respective temperature needed to allow for complete transformation to occur. Intrigued by the above observation, ~2 g sample of 30 minutes, 1 hour, 2 hours, and 3 hours of mechanically milled powder was placed on a corundum crucible and thermally treated at ~1151K with 30 minute dwell time at the peak temperature inside a tube furnace under argon atmosphere. The powder XRD analysis of the heat-treated powder confirmed the formation of ternary copper CP—$Cu_2Mo_6Se_8$ with slight presence of unreacted Mo, MoO_2 and $MoSe_2$ phase. Full frame quantitative EDX analyses of the low magnification (1000×) SEM images also proved the presence of Cu, Mo and Se atoms in the ternary $CuMo_6Se_8$ phase formed at 1151K with 30 minute dwell time as well as in the hydrochloric acid treated de-cuprated Mo_6Se_8 phase. The above data was encouraging and in good agreement with TG-DSC, and suggested that synthesis of fully crystalline $Cu_2Mo_6Se_8$ phase was possible by the HEMM approach in a time duration as low as 30 minutes at ~1151K. Lattice parameter(s) of $Cu_2Mo_6Se_8$ phase were calculated using the least-square method of the experimental data and are presented in Table 5. The excellent agreement of lattice parameters with the standard unit cell parameter(s) of $Cu_2Mo_6Se_8$ reported in the literature suggested that the HEMM approach could be applied successfully for the synthesis of selenium CP with minimal thermal treatment required at ~1151K under argon atmosphere.

TABLE 5

Calculated lattice parameter(s) of $Cu_xMo_6Se_8$ phase.

Condition	Lattice parameter(s) of $Cu_2Mo_6Se_8$	Quantitative Phase formation (%)
1 h mechanically milled powder thermally treated to 1089K	a_H: 0.999259 nm, c_H: 1.072559 nm a_R: 0.678719 nm, α_R: 94.8065° unit cell volume = 927.4872 × 10^{-3} nm^3	0.2% Mo + 1.8% MoO_2 + 1.7% MoSe2 + 96.3% $Cu_2Mo_6Se_8$
1 h mechanically milled powder thermally treated to 1151K	a_H: 0.997191 nm, c_H: 1.07323 nm a_R: 0.677823 nm, α_R: 94.7132° unit cell volume = 924.2306 × 10^{-3} nm^3	0.3% Mo + 1.8% MoO_2 + 1.7% $MoSe_2$ + 96.2% $Cu_2Mo_6Se_8$
30 min mechanically milled powder thermally treated to 1151Kwith 30 min hold at 1151K	a_H: 0.972965 nm, c_H: 1.092789 nm a_R: 0.669508 nm, α_R: 93.2087° unit cell volume = 895.9042 × 10^{-3} nm^3	0.2% Mo + 1.9% MoO_2 + 1.7% $MoSe_2$ + 96.2% $Cu_2Mo_6Se_8$
3 h mechanically milled powder thermally treated to 1273Kwith 5h hold at 1273K	a_H: 1.002506 nm, c_H: 1.07251 nm a_R: 0.680305 nm, α_R: 94.9202° unit cell volume = 933.4816 × 10^{-3} nm^3	1.8% MoO_2 + 1.7% $MoSe_2$ + 96.5% $Cu_2Mo_6Se_8$

Phase Formation and Electrochemical Activity of HEMM Derived De-Cuprated Mo_6Se_8

The de-cuprated Mo_6Se_8 phase was obtained by completely leaching out copper from $Cu_2Mo_6Se_8$ phase formed at 1151K with 30 minutes dwell time at the peak temperature. The XRD patterns analysis confirmed the formation of Mo_6Se_8 phase along with minor MoO_2 and unreacted $MoSe_2$ phase. The major Bragg peaks matched with the standard Mo_6Se_8 pattern (ICDD: 01-085-0455) suggested copper was completely removed. SEM image of the Mo_6Se_8 phase showed particles of submicron to micrometer size. Electrochemical performance of the 80 wt. % Mo_6Se_8: 10 wt. % Super-P: 10 wt. % PVDF composite electrode was evaluated in a 2016 coin cell. The electrochemical test showed the 1st cycle discharge (magnesiation) and charge (de-magnesiation) capacity was ~58.5 $mAhg^{-1}$ and ~64 $mAhg^{-1}$ with Coulombic efficiency ~91.5%. In the 2nd cycle the discharge and charge capacity were ~59.4 $mAhg^{-1}$ and ~70.5 $mAhg^{-1}$ and in the 3rd cycle, the discharge and charge capacity were ~63.8 $mAhg^{-1}$ and ~75.5 $mAhg^{-1}$, respectively. It is apparent from the voltage profile that a single voltage plateau was observed during the 1st cycle discharge (~0.85V) and charge (~1.17V) whereas 2-steps magnesiation at ~1.05V and ~0.97V and de-magnesiation reactions at ~1.1V and ~1.17V were evident in the 2nd and 3rd cycle. The detailed subtle differences in the charge-storage mechanisms into Mo_6Se_8 phase from the 1st cycle and the subsequent cycles are discussed later herein. However, the competitive electrochemical data of de-cuprated Mo_6Se_8 phase obtained from $Cu_2Mo_6Se_8$ phase formed at 30 minutes suggested the ease of synthesis of the corresponding selenium CP.

The fully crystalline, $Cu_2Mo_6Se_8$ ternary CP was also obtained upon heating the 3 hours mechanically milled sample at ~1273K with additional 30 minutes dwell time at peak temperature. The XRD pattern of 3 hours mechanically milled powder thermally treated at ~1273K with 5 hours dwell time at peak temperature showed the formation of $Cu_2Mo_6Se_8$ phase along with $MoSe_2$ and MoO_2 as impurities (Table 5). De-cuprated Mo_6Se_8 was obtained by com-

plete leaching of copper using a 6 molar HCl solution under oxygen bubbling for 7 hours. The lattice parameter(s) of $Cu_2Mo_6Se_8$ was calculated using least-square method and are shown in Table 5. The lattice parameter(s) of $Cu_2Mo_6Se_8$ was in good agreement with standard unit cell parameter(s). Whereas, lattice parameter(s) of de-cuprated Mo_6Se_8 (a=0.955858 nm, c=1.116432 nm, unit cell volume=883.3835×10-3 nm3) was found to be in excellent agreement with the standard Mo_6Se_8 (ICDD number: 01-085-0455; a=0.95488 nm, c=1.12095 nm, unit cell volume=884.40×10-3 nm3) unit cell parameters suggesting that copper was completely removed by HCl treatment from the $Cu_2Mo_6Se_8$ phase. The SEM image of $Cu_2Mo_6Se_8$ and de-cuprated Mo_6Se_8 showed irregular shaped submicron size particles that were formed in the case of $Cu_2Mo_6Se_8$ phase which retained its morphology completely in the de-cuprated Mo_6Se phase. The HRTEM lattice fringe spacing was calculated as ~0.668 nm and ~0.35 nm corresponded to the interplanar d-spacing of (101) and (202) planes for $Cu_2Mo_6Se_8$ and ~0.666 nm for Mo_6Se_8 corresponding to the interplanar d-spacing of (101) plane (hexagonal crystal system: space group R-3).

The composite electrode consisted of 80 wt. % Mo_6Se_8 phase (−325 mech) with 10 wt. % Super-P carbon additive and 10 wt. % PVDF binder. It was then tested in a 2016 coin cell setup as a cathode and polished Mg foil as anode separated by a Celgard® separator soaked in 2(PhMgCl)—AlCl3/tetrahydrofuran electrolyte. It showed good electrochemical performance. The cyclic voltammogram, acquired at a sweep rate of 0.1 mVs^{-1} between 0.5-1.5V versus Mg/Mg^{2+} couple, showed a typical two-step reversible magnesiation/demagnesiation phenomena where magnesiation occurred at ~1.04V, and ~0.96V and demagnesiation at ~1.11V, and ~1.18V, respectively. The anodic/cathodic peaks matched well with the theoretical calculation of the magnesiation/demagnesiation voltage. It was noted that magnesium intercalation/de-intercalation phenomena from Mo_6Se_8 phase was completely reversible and no partial Mg-ion trapping occurred as in the $Mg_xMo_6S_8$ phase due to the higher polarizability of the selenium anionic framework. The electrochemical performance of Mo_6Se_8 composite electrode as well as the Mo_6Se_8-graphite (7:3 weight ratio) in situ composite electrode were compared when tested at a current rate of 20 mAg^{-1}. The galvanostatic cycling of Mo_6Se composite electrode showed a 1^{st} cycle discharge (magnesiation) and charge (demagnesiation) capacity of ~83.5 mAhg-1 (~95% of theoretical capacity—88 $mAhg^{-1}$) and ~76.3 $mAhg^{-1}$ with Coulombic efficiency ~91.4%. Between the 2^{nd} and 100 cycle, an average discharge and charge capacity of ~71.2 $mAhg^{-1}$ and 74.2 $mAhg^{-1}$ was observed with ~96% Coulombic efficiency. The gradual fade in capacity from the 2^{nd} to 100^{th} cycle accompanied by ~4% irreversible loss per cycle was due to a change in the crystal structure of magnesiated Mo_6Se_8 from rhombohedral ($R\bar{3}$) to triclinic ($P\bar{1}$) phase and corresponding loss in electronic and ionic conductivity. The $Mg_1Mo_6Se_8$ and $Mg_2Mo_6Se_8$ crystallized into the triclinic form at room temperature by cation displacement or due to cation ordering of crystal structure which caused expansion of the unit cell and resulted in loss of electrical contact of the active mass with current collector. The calculated molar volume of Mo_6Se (R0), $Mg_1Mo_6Se_8$ (T1) and $Mg_2Mo_6Se_8$ (T2) phase were ~88.78 cm^3/mol, ~184.38 cm^3/mol, and ~195.63 cm^3/mol, respectively. The R0 to T1 transformation was associated with ~107% cell volume expansion which may cause loss of electrical contact between the active mass and current collector as well as inherently poor electronic and ionic conductivity of the triclinic Chevrel phase resulting in ~4% capacity fade. In the $Mg_2Mo_6Se_8$ phase, both the Mg-ions were located in the tetrahedral sites of outer ring of cavity 2 and formed a new type of cationic arrangements. The structural rearrangement occurred where four cation sites (2 tetrahedra and two square-pyramids) in cavity 1 for $Mg_1Mo_6Se_8$ degenerated into six tetrahedral sites. Thus, it appeared that the triclinic phase (T1 and T2) is suitable for Mg-ion diffusion and is free from any charge trapping although the loss in capacity gradually is due to poor ionic/electronic conductivity of the magnesiated Mo_6Se_8 phase.

To counteract the loss in electronic/ionic conductivity and associated capacity fade, a bottom-up approach was employed. First, Mo_6Se_8 particles embedded within the graphitic matrix were obtained using synthetic graphite during milling operation. 70 wt % of (2CuSe+3Mo+$3MoSe_2$) powder with 30 wt. % synthetic graphite (Aldrich, 1-2 μm) was mechanically milled for 3 hours and subjected to thermal treatment at ~1273K with 5 hours dwell time at the peak temperature. The XRD patterns of the milled, thermal-treated and copper leached powder showed the presence of elemental Mo, $MoSe_2$, and CuSe phase along with the high intensity peak from (003) plane of graphite at 2θ value of 26.31° of the 3 hours milled powder. The 3 hours milled powder when heated to ~1273K under argon atmosphere showed the formation of fully crystalline $Cu_2Mo_6Se_8$+graphite phase along with unreacted $MoSe_2$. Further, copper was leached out and as a result, the de-cuprated Mo_6Se_8+graphite (7:3) phase was obtained. It can be seen from the three XRD patterns that peak from (003) plane of graphite was present. However, the peak intensity decreased and indicated the collapse of microcrystalline graphite structure and formation of an amorphous disordered carbon due to defect induced melting commonly observed during high energy mechanical milling.

The electrochemical performance of the in situ Mo_6Se+graphite (7:3) when evaluated in a 2016 coin cell showed significantly improved performance compared to Mo_6Se_8 electrode. Although the capacity of in situ Mo_6Se+graphite (7:3) electrode was lower than Mo_6Se_8 electrode due to 70% active mass, it showed an extremely stable capacity up to 100 cycle. The 1^{st} cycle discharge and charge capacity was ~69.3 $mAhg^{-1}$ and ~54.8 $mAhg^{-1}$ with ~79.1% Coulombic efficiency. Between the 2^{nd} and 100^{th} cycle, an average discharge and charge capacity of ~50.43 $mAhg^{-1}$ and 50.4 $mAhg^{-1}$ was observed with ~99.93% Coulombic efficiency. From the above study, it can be inferred that graphite provided the required electronic path for Mg-ion intercalation/de-intercalation to occur reversibly into and from the Mo_6Se_8 phase and improve the Coulombic efficiency from ~96% to ~99.93%. Capacity versus voltage profile of 1^{st}, 2^{nd}, 3^{rd}, 4^{th}, 15^{th}, and 100^{th} cycle of Mo_6Se_8 and Mo_6Se_8+in situ graphite (7:3) showed exactly similar two-steps magnesiation at ~0.96V and ~1.03V and demagnesiation reaction plateaus at ~1.11V and ~1.18V was in agreement with cyclic voltammetry data. However, the 1^{st} cycle magnesiation required a slight overvoltage and a single sloping reaction plateau was observed at ~0.85V and correspondingly, the de-magnesiation reaction occurred at ~1.15V and ~1.20V due to the kinetic barrier that existed in the Chevrel phase host. Rate retention of Mo_6Se_8 electrode was also good, at C/4, 3 C/8, C/2, 3 C/4, 1 C (1 C~80 mAg^{-1}), 3 C/2, and 2 C current rate giving average discharge capacity of ~71.3 $mAhg^{-1}$, ~60.5 $mAhg^{-1}$, ~56.2 $mAhg^{-1}$, ~51.7 $mAhg^{-1}$, ~47.7 $mAhg^{-1}$, ~41.9 $mAhg^{-1}$, and ~31.2 $mAhg^{-1}$ was achieved with Coulombic efficiency ~96.1%, ~97.5%,

~98.7%, ~99.5%, ~99.3%, ~99.8%, and ~99.9%, respectively. From the above study it appears that HEMM approach is also suitable for rapid synthesis of $Cu_2Mo_6Se_8$ Chevrel phase, another potential cathode for rechargeable magnesium battery.

Conclusions

High energy mechanical milling is a suitable approach for preparing ternary Chevrel phase ($Cu_2Mo_6Z_8$; Z=S, Se) using metal and metal sulfide as precursors. $Cu_2Mo_6S_8$ was synthesized from CuS, Mo and MoS_2 composition by using the higher energy mechanical milling (HEMM) approach. Mechanical milling of $2CuS+3Mo+3MoS_2$ in the corresponding stoichiometric composition for 30 minutes to 3 hours formed a homogeneous intricate mixture which upon heating at elevated temperature formed the desired ternary phase. Quantitative X-rays diffraction study showed ~98% $Cu_2Mo_6S_8$ phase could be obtained with 30 minutes of milling followed by thermal treatment at 1123K for 30 minutes under argon. SEM images showed the formation of submicron to micrometer sized agglomerated particles. TG-DSC curves were able to show that elemental Mo reacted with CuS and nucleated the $Cu_{1.83}Mo_3S_4$ phase first which further reacted with MoS_2, and unreacted Mo and formed the desired $Cu_2Mo_6S_8$ phase. Electrochemical performance of de-cuprated Mo_6S_8 phase in a magnesium battery exhibited competitive performance where magnesiation and de-magnesiation was observed at ~1.0V and ~1.28V respectively. Galvanostatic cycling data showed the 1st cycle discharge and charge capacity of ~92 $mAhg^{-1}$ and ~57 $mAhg^{-1}$ with Coulombic efficiency ~62%. The Mo_6S_8 electrode was able to deliver a specific capacity ~70 $mAhg^{-1}$ up to 330 cycles with 99% Coulombic efficiency in a coin cell setup demonstrated the structural integrity of the HEMM-derived Mo_6S_8 phase. The corresponding $Cu_2Mo_6Se_8$ phase was also synthesized by thermal treatment of the milled powder at 1151K for 30 minutes with ~96% yield with unreacted Mo, $MoSe_2$ and MoO_2 as minor impurities. Electrochemical data of Mo_6Se_8 electrode showed a two-step magnesiation (at ~1.04V and ~0.96V) and de-magnesiation (at ~1.11V and ~1.18V) phenomena. Galvanostatic cycling of Mo_6Se_8 electrode showed a 1^{st} cycle discharge and charge capacity of ~83.5 $mAhg^{-1}$ and ~76.3 $mAhg^{-1}$, respectively with ~91.4% Coulombic efficiency. A stable discharge and charge capacity of ~71.2 $mAhg^{-1}$ and ~74.2 $mAhg^{-1}$ was observed with 4% fade per cycle likely due to ~107% stress generated at the electrode due to change in the crystal structure of magnesiated Mo_6Se_8 from rhombohedral ($R\bar{3}$) to triclinic ($P\bar{1}$) phase which resulted in a loss in the electrical path of active mass with current collector. Conductive carbon matrix embedded Mo_6Se_8 particles generated via milling approach were capable of salvaging the fade in capacity and a stable specific capacity of ~50 $mAhg^{-1}$ was observed up to 100 cycles with ~0.07% fade per cycle using graphite and PMAN as the carbon source.

In summary, sulfur and selenium ternary CPs synthesized by the time saving, scalable HEMM approach, and binary CPs obtained by acid leaching copper thereafter were shown as cycle stable Mg-ion battery cathodes suitable for electrical energy storage applications.

Example XIV ($Cu_1Mo_6S_8$)

Experimental

The $Cu_2Mo_6S_8$ (Cu_2CP) Chevrel phase was synthesized by using the high energy mechanical milling (HEMM) route. The approach involved taking stoichiometric amounts of MoS_2, Mo, and CuS batched in a SS vial (powder:ball ratio=1:10). The powders were mechanically milled for 1 h, 2 h, and 3 h intervals. After 3 h milling, the powder was heat-treated at 1000° C. with a heating rate 10° C./min and kept at the peak temperature for 5 h under ultra-high purity (UHP) Ar atmosphere. XRD pattern of the heat-treated powder showed the formation of pure crystalline $Cu_2Mo_6S_8$. Further, $Cu_2Mo_6S_8$ was washed with hydrochloric acid for 2 days to yield a completely crystalline $Cu_1Mo_6S_8$ (Cu_1CP) phase. It was known that Mg^{2+} insertion into the Mo_6S_8 Chevrel phase occurs in two stages, and therefore offers a capacity ~120 $mAhg^{-1}$. Due to partial charge entrapment after the initial magnesiation reaction only ~50-60% magnesium-ion could be extracted resulting ~40-50% irreversible loss in the 1st cycle from the theoretical value (~120 $mAhg^{-1}$). In order to minimize the 1^{st} cycle irreversible loss (FIR), Cu ions were partially leached from the original Cu_2CP structure. Therefore, 1.8 g of Cu_2CP was added to 20 ml 6 M HCl solution in a small glass vial with a magnetic stir bar. The Cu_2CP/HCl solution was continuously stirred for 2 days at room temperature. After 2 days of continuous stirring, the solution was ultrasonically cleaned using distilled water (3 times) and dried at 60° C. for 24 h. The XRD pattern of the partial leached Cu_2CP shows the formation of completely crystalline $Cu_1Mo_6S_8$ (Cu_1CP). Electrodes were fabricated from the synthesized $Cu_1Mo_6S_8$ (Cu_1CP) and tested in 2016 coin cells using 0.4 molar 2(PhMgCl—$AlCl_3$)/tetrahydrofuran electrolyte in the voltage window of 0.5V-1.5V against pure Mg used as the anode following our published work [3]. Results of the electrochemical cycling are provided below.

Results

FIG. **1** shows the XRD pattern of the heat-treated Cu_2CP powder obtained by the precursor route. The Bragg diffraction lines were indexed to a hexagonal-rhombohedral symmetry unit cell of $Cu_2Mo_6S_8$ (space group: R-3; number: 148; JCPDS-ICDD: 00-047-1519). Lattice parameter(s) calculated using the least-square method from the collected experimental data (a=0.96478 nm, c=1.02026 nm, and unit cell volume=822.42×10^{-3} nm^3) were in good agreement with the standard $Cu_2Mo_6S_8$ unit cell parameters (a=0.9584 nm, c=1.025 nm, unit cell volume=815.36×10^{-3} nm^3). Similarly, FIG. **1** exhibits the XRD pattern obtained after removal of one copper from the heat-treated powder using the hydrochloric acid treatment. The Braggs lines were indexed with the hexagonal-rhombohedral symmetry unit cell of $CuMo_6S_8$ phase (space group: R-3; number: 148; JCPDS-ICDD: 00-034-1379), and the calculated lattice parameter(s) (a=0.94412 nm, c=1.04761 nm, and unit cell volume=808.70×10^{-3} nm^3) matched quite well with standard unit cell parameters of $CuMo_6S_8$ obtained from the above ICDD database (a=0.94120 nm, c=1.04070 nm, unit cell volume=798.40×10^{-3} nm^3) The calculated lattice parameters values are also consistent with the standard lattice parameter(s) values of pristine $Cu_2Mo_6S_8$ and acid leached $CuMo_6S_8$ powder obtained from JCPDS-ICDD database suggesting that the 6M HCl treatment for 2 days was successful in leaching out 50% copper from the original Cu_2CP structure and thus yielding $Cu_1Mo_6S_8$ (Cu_1CP) (Table 6)

Material	a (Å)	c (Å)	Unit cell volume (10^6 × pm^3)
HEMM derived $Cu_2Mo_6S_8$	9.6478	10.2026	822.42

-continued

Material	a (Å)	c (Å)	Unit cell volume ($10^6 \times pm^3$)
Standard $Cu_2Mo_6S_8$ (ICDD: 00-047-1519)	9.5840	10.250	815.36
HC1 leached $CuMo_6S_8$	9.4412	10.4761	808.70
Standard $CuMo_6S_8$ (ICDD: 00-034-1379)	9.4120	10.4070	798.40

FIG. **2***a* displays the variation in specific capacity versus cycle number along with Coulombic efficiency of the acid leached $Cu_1Mo_6S_8$ electrode, cycled at a constant current of ~20 mAg^{-1} (~C/6 rate) in the potential window of 0.5-1.5 V using 0.4 molar 2(PhMgCl—$AlCl_3$)/tetrahydrofuran electrolyte. As observed in FIG. **2***a*, the 1^{st} cycle discharge and charge capacity of the $Cu_1Mo_6S_8$ electrode is ~105 $mAhg^{-1}$ and ~78 $mAhg^{-1}$, respectively, with a 1^{st} cycle irreversible loss of ~25.7% (or Coulombic efficiency of ~74.3%). However, from the 10^{th} cycle onward we can see the electrode maintaining a steady charge-discharge capacity of ~55 $mAhg^{-1}$, with a Coulombic efficiency of ~99.9%. It is noted that a first cycle irreversible loss of ~50% is seen for the Mo_6S_8 CP obtained by completely leaching copper out of HEMM derived Cu_2CP structures. The preliminary results obtained for Cu_1CP is therefore encouraging and suggest that partial Mg^{2+} charge entrapment which is common during the 1^{st} cycle magnesiation (discharge) in Mo_6S_8 cathode can be partially overcome with $Cu_1Mo_6S_8$ structure where one Mg^{2+} can cycle without any hindrance. FIG. **2***b* shows the galvanostatic charge-discharge profile (1^{st}, 2^{nd}, 3^{rd}, 10^{th}, 20^{th}, 50^{th} and 90^{th} cycle) of the $Cu_1Mo_6S_8$ electrode conducted at a constant current rate 20 mAg^{-1} (~C/6). During the 1^{st} cycle, a sloping voltage curve is observed for Mg^{2+} insertion/extraction owing to kinetic limitation requiring slight overvoltage of ~200-300 mV from the equilibrium magnesiation potential of ~1.1 V. However, from 10^{th}, 20^{th}, 50^{th}, and 90^{th} cycles onwards single reaction plateaus are observed at ~1.1 V (Mg^{2+} insertion) and at ~1.2 V (Mg^{2+} extraction), respectively. FIG. **2***c* shows the rate capabilities of the $Cu_1Mo_6S_8$ electrode at various current rates of 5 mAg^{-1} (~C/24), 10 mAg^{-1} (~C/12), 20 mAg^{-1} (~C/6), 30 mAg^{-1} (~C/4), 40 mAg^{-1} (~C/3), and 60 mAg^{-1} (~C/2). The $Cu_1Mo_6S_8$ delivers average discharge capacity of ~57 $mAhg^{-1}$, ~56 $mAhg^{-1}$, ~44 $mAhg^{-1}$, ~40 $mAhg^{-1}$, ~32 $mAhg^{-1}$, ~29 $mAhg^{-1}$ at ~C/24, ~C/12, ~C/6, ~C/4, ~C/3, and ~C/2 rates with Coulombic efficiency ~97%, ~100%, ~98.6%, ~98.7%, 99.1%, and ~98.7%, respectively.

In order to understand the reaction mechanism, the Cu_1CP electrode was cycled at a slow current rate of ~5 mAg^{-1} (~C/24 rate) within the potential window of 0.5-1.5 V using 0.4 molar 2(PhMgCl—$AlCl_3$)/tetrahydrofuran electrolyte in a Mg cell. The 1^{st} cycle discharge (magnesiation) and charge (demagnesiation) capacity was observed ~81 and ~80 $mAhg^{-1}$ with 1^{st} cycle irreversible loss ~1.23% implying partial Mg-ion trapping that is common to the Chevrel phase electrodes (Mo_6T_8, T=S, Se) can be avoided (see FIG. **3***a*). In the 2^{nd} and 3^{rd} cycle ~99% Coulombic efficiency was observed. Noticeably, the differential capacity versus voltage curves (dQ/dV versus V) of the 2^{nd} and 3^{rd} cycle illustrates four pairs of redox peaks observed at ~1.22 V, ~1.15V, ~1.1V, and ~0.8V during discharge and ~1.04V, ~1.18V, ~1.23V, and ~1.32V during charge implying that the magnesiation/de-magnesiation reactions in the synthesized Cu_1CP occurs in various stages (see FIG. **3***b*). In order to understand the phase formation, 2016 coin cells were cycled at a slow current rate of ~5 mAg^{-1} between ~0.5V and ~1.5V cut-off voltage. The cells were then disassembled inside an UHP Ar filled glove box and washed with anhydrous tetrahydrofuran (THF) followed by vacuum drying. Ex-situ XRD analysis of the cycled electrodes compared with the bare electrode interestingly indicate partial copper leaching and simultaneous Mg-ion intercalation/de-intercalation with the formation of $Cu_{1-x}Mg_xCP$ and $Cu_{1-y}Mg_yCP$ ($y<x$; $x,y<1$) at the discharge and charge states, respectively (see FIG. **3***c*). In the 2^{nd} cycle, complete copper leaching and exchange with one Mg-ion intercalation occurred during the discharge cycle with the formation of Mg_1CP, whereas complete Mg-ion removal did not occur during the charge cycle leading to the formation of $Cu_{1-y}Mg_y$ CP ($y<1$). In the subsequent cycles however, single Mg-ion intercalation along with partial copper leaching occurred between the two end members of Cu_1CP and Mg_1CP resulting in suppression of Mg-ion trapping akin to CP and thereby resulting in improved Coulombic efficiency. More importantly, it should be noted that the cycling data of Cu_1CP between 2^{nd}-50^{th} cycle at a slow current rate of ~5 mAg^{-1} shows an average discharge-charge capacity of ~55 $mAhg^{-1}$ yielding a Coulombic efficiency ~98% (see FIG. **3***d*). The interesting aspect is the ability of the CuCP to reversibly intercalate one Mg^{2+} ion and also reversibly cycle Cu^{2+} ion.

Example XV ($Mo_6S_{8-x}Se_x$ $1<x<8$)

Experimental: Synthesis of $Cu_2Mo_6S_7Se_1/Mo_6S_7Se_1$ by the High Energy Mechanical Milling (HEMM) Route

Stoichiometric amounts of MoS_2 (0.875 g), $MoSe_2$ (0.1426 g), Mo (0.579 g), CuS (0.35 g) and CuSe (0.0534 g) were batched in a SS vial (powder:ball ratio=1:10). The powders were mechanically milled for 3 h and subjected to XRD analysis. After 3 h milling, the powder was heat-treated at 1000° C. for 5 h under UHP Ar atmosphere. XRD pattern of the heat-treated powder shows the formation of fully crystalline, pure $Cu_2Mo_6S_7Se_1$. The resultant $Cu_2Mo_6S_7Se_1$ was then subsequently washed with HCl/O_2 bubbling for 7 h and the XRD pattern collected on the leached material confirms the formation of $Mo_6S_7Se_1$ (see FIG. **4**). Electrodes were again fabricated as in the case of Example XIV. Accordingly, electrodes were fabricated from the synthesized Mo_6S_7Se (CP) and tested in 2016 coin cells using 0.4 molar 2(PhMgCl—$AlCl_3$)/tetrahydrofuran electrolyte in the voltage window of 0.5V-1.8V against pure Mg used as the anode following our published work. Results of the electrochemical cycling are provided below.

Results

The cyclic voltammogram (CV) in FIG. **5***a* acquired at a sweep rate of ~50 μVs^{-1} between 0.5-1.8 V versus Mg/Mg^{2+} shows the magnesiation reaction (~0.98V) and demagnesiation reaction (~1.3 V, and ~1.56 V) events occurring in the Mo_6S_7Se electrode respectively, in the very 1^{st} cycle. In the 2^{nd} cycle, 2 pairs of magnesiation and demagnesiation peaks were observed at ~1.08 V, ~1.0 V, ~1.3 V, ~1.56 V, respectively. FIG. **5***b* shows the variation of specific capacity versus cycle number along with Coulombic efficiency of the $Mo_6S_7Se_1$ electrode, cycled at a constant current of ~20 mAg^{-1} (~C/6 rate) in the potential window of 0.5-1.8 V using 0.4 molar 2(PhMgCl—$AlCl_3$)/tetrahydrofuran electrolyte. The galvanostatic cycling result shows a 1^{st} cycle discharge (magnesiation) and charge (demagnesiation) capacity of ~68.5 $mAhg^{-1}$ (~58% of the theoretical capacity of ~115.6 $mAhg^{-1}$) and ~66.3 $mAh{\cdot}g^{-1}$, respectively, with a Coulombic efficiency of ~96.8%. Between the 2^{nd} and 200^{th} cycles, an average discharge and charge capacity of ~66 and

64 $mAhg^{-1}$, respectively, were observed with ~97% Coulombic efficiency (see FIG. **5***b*). The capacity versus voltage profiles of the 2^{nd}, 100^{th}, and 200^{th} cycles shown in FIG. **5***c*, exhibiting two pairs of magnesiation (~1.17 V and ~1.13 V) and demagnesiation (~1.17 V and ~1.45 V) reaction plateaus, respectively, in agreement with the differential capacity versus voltage curves (see FIG. **5***d*). The results above show the ability of the sulfo-selenide CP to reversibly cycle Mg^{2+} ions in the voltage window of 0.5V-1.8V with respect to Mg.

Experimental: Synthesis of $Cu_2Mo_6S_{8-x}Se/Mo_6S_{8-x}Se_x$ (x=3, 4, 5) by the HEMM Route

$Cu_2Mo_6S_5Se_3/Mo_6Se_3$: Stoichiometric amounts of MoS_2 (0.625 g), $MoSe_2$ (0.428 g), Mo (0.537 g), CuS (0.25 g) and CuSe (0.16 g) corresponding to the nominal composition of $Cu_2Mo_6S_5Se_3$ were batched in a SS vial (powder:ball ratio=1:10). The powders were mechanically milled for 3 h and subjected to XRD analysis. After 3 h milling, the powder was heat-treated at 1000° C. for 5 h under UHP Ar atmosphere. XRD pattern of the heat-treated powder shows the formation of fully crystalline, pure $Cu_2Mo_6S_5Se_3$. The resultant $Cu_2Mo_6S_5Se_3$ was washed with HCl/O_2 bubbling for 7 h and the XRD pattern collected on the resultant powder confirms the formation of $Mo_6S_5Se_3$ (see FIG. **6***a*).

$Cu_2Mo_6S_4Se_4/Mo_6S_4Se_4$: Stoichiometric amounts of MoS_2 (0.5 g), $MoSe_2$ (0.57 g), Mo (0.516 g), CuS (0.23 g) and CuSe (0.214 g) corresponding to the nominal composition of $Cu_2Mo_6S_4Se_4$ were batched in a stainless steel (SS) vial (powder:ball ratio=1:10). The powders were mechanically milled for 3 h and subjected to XRD analysis. After 3 h milling, the powder was heat-treated at 1000° C. for 5 h under UHP Ar atmosphere. XRD pattern collected on the heat-treated powder shows the formation of pure crystalline $Cu_2Mo_6S_4Se_4$. The resultant $Cu_2Mo_6S_4Se_4$ was washed with HCl/O_2 bubbling for 7 h and the XRD collected on the acid treated powder confirms the formation of $Mo_6S_4Se_4$ (see FIG. **6***b*).

$Cu_2Mo_6S_3Se_8/Mo_6S_3Se_8$: Stoichiometric amounts of MoS_2 (0.375 g), $MoSe_2$ (0.7125 g), Mo (0.495 g), CuS (0.15 g) and CuSe (0.2675 g) corresponding to the nominal composition of $Cu_2Mo_6S_3Se_5$ were batched in a SS vial (powder:ball ratio=1:10). The powders were mechanically milled for 3 h and subjected to XRD analysis. After 3 h milling, the powder was heat-treated at 1000° C. for 5 h under UHP Ar atmosphere. XRD pattern collected on the heat-treated powder shows the formation of pure crystalline $Cu_2Mo_6S_3Se$. The obtained $Cu_2Mo_6S_3Se_5$ was washed with HCl/O_2 bubbling for 7 h and the XRD collected on the acid treated powder confirms the formation of Mo_6S_3Se (see FIG. **6***c*).

As outlined in EXAMPLE XIV and EXAMPLE XV above, electrodes were fabricated from the synthesized $Mo_6S_{8-x}Se_x$ (x=3, 4, 5) materials. Accordingly, electrodes were fabricated from the synthesized $Mo_6S_{8-x}Se_x$ (x=3, 4, 5) materials and tested in 2016 coin cells using 0.4 molar 2(PhMgCl—$AlCl_3$)/tetrahydrofuran electrolyte in the voltage window of 0.5V-1.5V for $Mo_6S_{8-x}Se_x$ (x=3, 4) and 0.5-1.75V for $Mo_6S_{8-x}Se_x$ (x=5) against pure Mg used as the anode following our published work. Results of the electrochemical cycling are provided below.

Results

FIG. **7***a* exhibits the variation of specific capacity versus cycle number along with Coulombic efficiency of the $Mo_6S_5Se_3$ electrode, cycled at a constant current of ~20 mAg^{-1} (~C/6 rate) in the potential window of 0.5-1.5 V using 0.4 molar 2(PhMgCl—$AlCl_3$)/tetrahydrofuran electrolyte. As observed in FIG. **7***a*, the 1^{st} cycle discharge and charge capacity of the $Mo_6S_5Se_3$ electrode is 74.2 $mAhg^{-1}$ and 52.5 $mAhg^{-1}$, respectively, with a 1^{st} cycle irreversible loss of ~29.3% (or coulombic efficiency of ~70.7%). From the 2^{nd} to 90^{th} cycle however, we observed an average stable discharge and charge capacity of ~50.8 $mAhg^{-1}$ and ~51.9 $mAhg^{-1}$ with Columbic efficiency ~97.9%. FIG. **7***b* shows the galvanostatic charge-discharge profile (1^{st}, 2^{nd}, 10^{th}, 20^{th}, and 50^{th} cycle) of the $Mo_6S_5Se_3$ electrode obtained at a constant current rate ~20 mAg^{-1} (~C/6). During the 1^{st} cycle, a single plateau is observed at ~0.92 V for Mg^{2+} insertion owing to the kinetic limitation in $Mo_6S_5Se_3$ electrode. However, for the 2^{nd}, 10^{th}, 20^{th}, and 50^{th} cycle onwards sloping charge and discharge reaction plateaus are observed centered on ~1.1 V/~1.25 V for both Mg^{2+} insertion/extraction reactions, respectively.

FIG. **8***a* illustrates the variation in specific capacity versus cycle number along with Coulombic efficiency obtained for the $Mo_6S_4Se_4$ electrode, cycled at a constant current of ~20 mAg^{-1} (~C/6 rate) in the potential window of 0.5-1.5 V using 0.4 molar 2(PhMgCl—$AlCl_3$)/tetrahydrofuran electrolyte. As observed in FIG. **8***a*, the 1^{st} cycle discharge and charge capacity of the $Mo_6S_4Se_4$ electrode is ~63 $mAhg^{-1}$ and ~43 $mAhg^{-1}$, respectively, with a 1^{st} cycle irreversible loss of ~31.7% (or Coulombic efficiency of ~68.3%). From the 2^{n}d to 100^{th} cycle we observed an average stable discharge and charge capacity of ~40.5 $mAhg^{-1}$ and ~38.7 $mAhg^{-1}$ with Columbic efficiency ~95.6%. FIG. **8***b* shows the galvanostatic charge-discharge profile (1^{st}, 2^{nd}, 10^{th}, and 20^{th} cycle) of $Mo_6S_4Se_4$ electrode obtained at a constant current rate ~20 mAg^{-1} (~C/6). During the 1st cycle, a single plateau is observed at ~0.86 V for the Mg^{2+} insertion owing to the kinetic limitation in the $Mo_6S_4Se_4$ electrode. However, for the 2^{nd}, 10^{th}, and 20^{th} cycle onwards characteristic sloping reaction plateaus are observed as in the case of the $Mo_6S_5Se_3$ electrode.

FIG. **9***a* illustrates the variation of specific capacity versus cycle number along with Coulombic efficiency of the $Mo_6S_3Se_5$ electrode, cycled at a constant current of ~20 mAg^{-1} (~C/6 rate) in the potential window of 0.5-1.75 V using 0.4 molar 2(PhMgCl—$AlCl_3$)/tetrahydrofuran electrolyte. As observed in FIG. **9***a*, the 1^{st} cycle discharge and charge capacity of the $Mo_6S_3Se_5$ electrode is ~78 $mAhg^{-1}$ and ~63 $mAhg^{-1}$, respectively, with a 1^{st} cycle irreversible loss of ~19.2% (or Coulombic efficiency of ~80.8%). From the 2^{nd} to 200^{th} cycle however, we observed an average discharge and charge capacity of 60.6 $mAhg^{-1}$ and ~63.5 $mAhg^{-1}$ with Columbic efficiency ~95.6%. FIG. **9***b* shows the galvanostatic charge-discharge profile (1^{st}, 2^{nd}, 10^{th}, 20^{th}, and 50^{th} cycle) of $Mo_6S_3Se_5$ electrode obtained at a constant current rate ~20 mAg^{-1} (~C/6). During the 1^{st} cycle, a single reaction plateau is observed at ~0.74 V for Mg^{2+} insertion owing to the kinetic limitation in $Mo_6S_3Se_5$ electrode. However, for the 2^{nd}, 10^{th}, 20^{th}, and 50^{th} cycles onwards, characteristic sloping reaction plateaus are observed.

Rate Capability

FIG. **10** shows the rate capabilities of the synthesized $Mo_6S_5Se_3$ and $Mo_6S_4Se_4$ electrodes at various current rates of 5 mAg^{-1} (~C/24), 10 mAg^{-1} (~C/12), 30 mAg^{-1} (~C/4), 40 mAg^{-1} (~C/3), and 60 mAg^{-1} (~C/2). The $Mo_6S_5Se_3$ electrode delivers average discharge capacity of ~50 $mAhg^{-1}$, ~42 $mAhg^{-1}$, ~26 $mAhg^{-1}$, ~23 $mAhg^{-1}$, ~19 $mAhg^{-1}$ at ~C/24, ~C/12, ~C/4, ~C/3, and ~C/2 rates whereas, the $Mo_6S_4Se_4$ electrode delivers an average discharge capacity of ~42 $mAhg^{-1}$, ~34 $mAhg^{-1}$, ~25 $mAhg^{-1}$, ~20 $mAhg^{-1}$, ~7 $mAhg^{-1}$ at ~C/24, ~C/12, ~C/4, ~C/3, and ~C/2 rates, respectively.

In summary, it is important to note that both Cu_2CP and Cu_1CP combined with sulfo-selenide substituted forms of $Mo_6S_7Se_1$; $Mo_6S_5Se_3$; $Mo_6S_4Se_4$; $Mo_6S_3Se_5$ were successfully synthesized using the high energy mechanical milling (HEMM) approach. The resultant materials were then successfully converted to the desired Chevrel phase (CP) following heat treatments in ultra-high purity (UHP) Ar environment at temperature of 1000° C. for 5 h and then with appropriate acid leaching treatments in 6M HCl and a mixture of HCl/O_2 gas bubbling to form the partially-cuprated and de-cuprated substituted sulfo-selenide systems. All of the leached partially-cuprated/de-cuprated Chevrel phases are indeed electrochemically active showing stable capacities in the 51 $mAhg^{-1}$-66 mAg^{-1}. Increasing amounts of Se substitution in the CP phase results in the CP system exhibiting the highest specific capacity of ~66 $mAhg^{-1}$.

Whereas particular embodiments of the invention have been described herein for purposes of illustration, it will be evident to those skilled in the art that numerous variations of the details may be made without departing from the invention as set forth in the appended claims.

What is claimed is:

1. An electrochemical cell, comprising:

an alkali-metal-containing anode;

a cathode, comprising:

a Chevrel-phase material of a formula $Mo_6Z^1_{8-y}Z^2_y$ derived from a precursor material of a formula $M_xMo_6Z^1_{8-y}Z^2_y$, wherein M is a metallic element, 'x' is a number from greater than 0 to 4, 'y' is a number from greater than 0 to less than 8 and each of Z^1 and Z^2 is a different chalcogen with or without the presence of oxygen; and an electrolyte comprising a solution of 3-bis(trimethylsilyl) aminophenyl-magnesium chloride with aluminum chloride in tetrahydrofuran.

2. The electrochemical cell of claim **1**, wherein the alkali-metal-containing anode comprises magnesium.

3. The electrochemical cell of claim **1**, wherein the metallic element is selected from the group consisting of Li, Na, Mg, Ca, Sc, Cr, Mn, Fe Co, Ni, Cu, Zn, Sr, Y, Pd, Ag, Cd, In, Sn, Ba, La, Pb, Ce, Pr, Nd, Sm, Eu, Gd, Tb, Dy, Ho, Er, Tm, Yb, Lu and mixtures thereof.

4. The electrochemical cell of claim **1**, wherein each of the chalcogen Z^1 and Z^2 is selected from chemical elements in Periodic Table Group 16.

5. The electrochemical cell of claim **1**, wherein each of the chalcogen Z^1 and Z^2 is selected from the group consisting of sulfur, selenium, tellurium and mixtures of thereof.

6. The electrochemical cell of claim **1**, wherein M is copper, 'x' is 2, Z^1 is sulfur and Z^2 is selenium.

7. The electrochemical cell of claim **1**, wherein the precursor material is formed from a mixture of MZ^1, MZ^2, $MoZ_2{}^1$, $MoZ_2{}^2$ and molybdenum.

8. The electrochemical cell of claim **1**, wherein the Chevrel-phase material is of a formula Mo_6S_8 which is derived from a precursor material of a formula $Cu_2Mo_6Z^1_{8-y}Z^2_y$, and the said precursor material is derived from a mixture of ammonium tertathiomolybdate and anhydrous copper chloride in the presence of anhydrous N,N-dimethylformamide.

9. The electrochemical cell of claim **1**, wherein the said electrochemical cell is a rechargeable battery.

* * * * *